Western&Graduate&PostdoctoralStudies

Electronic Thesis and Dissertation Repository

2-5-2021 11:00 AM

Cluster Acceleration and Stabilization in Downflow Catalytic Reactors: Experimental and CPFD Simulation Studies

Cesar Alejandro Medina Pedraza, *The University of Western Ontario*

Follow this and additional works at: https://ir.lib.uwo.ca/etd

Part of the Catalysis and Reaction Engineering Commons

Abstract

Particle cluster dynamics in downflow reactors are of great importance for the implementation of large scale, environmentally friendly catalytic processes. Studies should address particle cluster velocities, solids holdups, and individual cluster sizes to establish reliable models for the unit scale up.

In this PhD dissertation, the individual characteristics of particle clusters, such as cluster size, velocity, and particle volume fraction, were measured in the feeding, intermediate, and fully developed flow sections of a cold-flow model unit using CREC-GS-Optiprobes. The downer unit employed in this research had a 0.051 m ID and a 2 m high acrylic column. The feeding section included a cyclone and a ring gas injector with eight nozzles angled at 45°. A fluid catalytic cracking (FCC) catalyst with a mean diameter of 84.4 μm and a density of 1722 kg/m^3 was used. The operating conditions for the experiments were superficial gas velocities of 1.0-1.6 m/s and solids mass fluxes of 30-50 kg/m^2s. The results obtained showed close to normal particle cluster size distributions near the feeding region, and skewed distributions with a higher frequency of short clusters in the fully developed flow section. Additionally, significant changes were noticed when clusters evolved from the feeding section to the fully developed flow section: the average cluster size changed from 7-9 particles to 3-4 particles, and 0.5-0.9 m/s cluster slip velocities in the downer entrance increased to 1.1-1.4 m/s in the stabilized region.

Regarding the obtained findings, it was observed that the cluster slip velocity is a function of the measured axial cluster length. On the basis of the data obtained, it was also established a quasi-spherical shape for the clusters in the entry downer section and a strand shaped cluster for clusters in the stabilized downer region.

Furthermore, by using computational fluid dynamics simulations (Multiphase Particle-in-Cell (MP-PIC) Method) and accounting for the experimentally determined cluster size distribution, a Hybrid Experimental-Numerical Cluster Model was postulated and successfully validated.

Finally, and to establish the relevance of the fluid dynamic model, a fluidized catalytic cracking (FCC) pilot-scale downer unit, was simulated using the developed Hybrid MP-PIC Model and kinetics obtained in a CREC Riser Simulator. Radial and axial temperature distributions show the adequacy of the gas-solid feeder employed. This was the case given the very effective gas-solid mixing leading to quick gas-solid radial thermal stabilization. On this basis, it was proven that flow stabilization can be achieved in a 1-2 m downer unit length, and this for typical FCC operated with 5-7 C/O (catalyst/oil) ratios.

Keywords: Fluidization, Downflow Reactors, Fluid Catalytic Cracking (FCC), Computational Fluid Dynamics (CFD), Computational Particle Fluid Dynamics (CPFD), Multiphase Particle-in-Cell (MP-PIC), Cluster Size Distribution.

Summary for Lay Audience

Chemical Engineering is the discipline that combines chemistry and physics to study the transformation of raw materials into more useful and valuable products. Within this field, reaction engineering is the branch responsible for the design of the vessel where the chemical reaction occurs.

Catalytic processes are responsible for the production of fuels and chemicals, among many other important products that contribute to the world's economic progress. Out of these catalytic processes, one of the most important is fluid catalytic cracking (FCC), which is a process that is at the heart of an oil refinery, taking the product of upstream units and producing gasoline and other precursors for the petrochemical industry.

Even though the FCC process has seen many improvements over the last 40 years, the need to meet stricter environmental regulations poses the challenge to develop better technology to perform this chemical process. The downflow fluidized bed reactor has been proposed as an improvement in the FCC process that will allow for the better utilization of the catalytic resources. Understanding the particle clusters behavior in the entrance region of the downflow reactor is crucial for the successful implementation of this unit.

With this objective in mind, the present PhD dissertation studied the gas-solid fluid dynamic characteristics of the downflow reactor, such as particle cluster velocity, size, and concentration, with a special focus on the entrance zone, using the advanced CREC-GS-Optiprobes fiber optic devices. Additionally, a numerical model was developed based on the experimental results and it was employed in the simulation of a pilot-scale fluid catalytic cracking downflow reactor. As a result, this project aims to contribute to the understanding of particle clusters in downflow fluidized bed reactors and their application in fluid catalytic cracking.

To my wife Karla,

my parents Herminio and Elvia Patricia,

my siblings Carlos and Paty.

Acknowledgments

First of all, I want to thank my supervisor, Professor Hugo de Lasa, an incredible person who I was most fortunate to have as my mentor, his guidance has been invaluable in my academic career and I thank him for the opportunity of doing my PhD studies in his research group.

My team members and friends from the CREC research group. Jose Munoz and Pastor Solano, the lab technicians, who were always helpful in solving problems with the equipment. Francisco Mora and Adriana Paz for their help during the experimental stage of my project. Florencia de Lasa, for reviewing and editing my papers and dissertation. Dr. Salvador Escobedo, Dr. Cristina Lugo, Dr. Sandra Lopez, Dr. Bianca Rusinque, Dr. Maureen Cordoba, and (hopefully one day Dr.) Jeonghoon Kong, who always had a good piece of advice for me. I want to especially thank Dr. Nicolas Torres, whose counsel and friendship helped me in my learning and PhD experience.

My parents, Herminio Medina and Patricia Pedraza, my brother Carlos, my grandma Ofelia. They are a great inspiration in my life, their love is the guide in everything I do. My family in law, Salvador Arredondo, Rosa Maria Ramirez, and Rosa Arredondo, who always have encouraged and supported me. To all my family and friends in Mexico, in particular, Yahir Moreno, thank you for your unconditional support.

Above all, I want to thank my wife, Karla Arredondo Ramirez, I could not ask for a better wife, life companion, and friend. I am deeply grateful for her ever-present love and patience through these years, without her support and advice this would not have been possible.

Contents

List of Tables

List of Figures

Nomenclature

Symbols

a, major axis of spheroid cluster, m.

b, minor axis of spheroid cluster, m.

$A_{c,max}$, cluster cross-sectional area normal to the flow, m^2.

$A_{c,sphere}$, spherical cluster cross-sectional area, m^2.

$A_{c,spheroid}$, prolate spheroid cluster cross-sectional area, m^2.

$A_{c,strand}$, cluster cross-sectional area normal to the flow for strand shape, m^2.

C_D, drag coefficient.

C_i , concentration of component i in five-lump kinetic model, mol/m^3.

C_{xy}, cross-correlation coefficient.

d , distance between probes, m.

D_a, mass diffusion coefficient, m^2/s.

d_p, particle average diameter, m.

$d_{p,max}$, diameter of largest particle in cluster, m.

D_s, drag function, s^{-1}.

F_g, gravity force, $kg\ m/s^2$.

F_D, drag force, $kg\ m/s^2$.

f, particle distribution function.

f_D, collision probability distribution function.

g, gravity acceleration, m/s^2.

G_s, solid mass flux, $kg/m^2\ s$.

h, transversal length of the CREC-GS-Optiprobes sensing region, m.

k_i, kinetic constant for the five-lump kinetic model.

K_1, Stoke's shape factor.

K_2, Newton's shape factor.

L, cluster axial length, m.

m_p, particle mass, *kg.*

n, baseline factor.

n_p, particle feed per average volume.

N, number of particles with average diameter in cluster.

N_{cells}, number of Eulerian cells.

N_p, total number of computational particles

n_{ss}, effectiveness factor.

p, pressure, Pa.

ΔP, pressure drop, *Pa.*

P_a, pressure loss due to acceleration of solids, *Pa.*

Pe, Peclet number.

r/R, dimensionless radial position.

r_p, particle radius, m.

r_{eq}, radius of the equivalent sphere with same volume as cluster, *m.*

Re_p, Reynolds number defined for a spherical particle.

t , time, s.

t_i, cluster time, *s.*

u_c, cluster velocity, *m/s.*

$\dot{u}_p$, particle acceleration, *m/s².*

u_f, fluid velocity, *m/s.*

u_p, particle velocity, *m/s.*

$\bar{u}_p$, average particle velocity, *m/s.*

$\bar{u}_{p,exp}$, radial average experimental particle velocity, *m/s.*

$\bar{u}_{p,sim}$, radial average simulation particle velocity, *m/s.*

U_{sg}, superficial gas velocity, *m/s.*

V, optiprobe signal voltage, *volt.*

V_c, cluster volume, *m³.*

V_{cell}, cell volume, *m³.*

$V_{c,sphere}$, spherical cluster volume, *m³.*

$V_{c,spheroid}$, cluster volume in prolate spheroid shape, *m³.*

$V_{c,strand}$, cluster volume in strand shape, *m³.*

v_i, stoichiometric coefficient of component *i* in five-lump kinetic model.

W_{cr}, catalyst mass in reactor, kg

x, length dimension, *m.*

X_E, mass fraction of coke on catalyst.

X_E', mass of coke produced per mass of vacuum gas oil injected.

$\bar{v}$, average of optiprobe signal, *volt.*

Z, axial position measured from the distributor, *m.*

Greek Letters

ε_f, fluid volume fraction.

ε_s, particle volume fraction.

$\varepsilon_{s,mf}$, particle volume fraction at minimum fluidization.

$\bar{\varepsilon}_{s,exp}$, radial average experimental particle volume fraction.

$\bar{\varepsilon}_{s,sim}$, radial average simulation particle volume fraction.

λ, deactivation parameter.

ρ_f, fluid density, kg/m^3.

ρ_s, particle density, kg/m^3.

σ_v, standard deviation of optiprobe signal, *volt.*

τ, lag between optiprobe signals *x* and *y, s.*

τ_c, particle contact stress, *Pa.*

τ_f, fluid stress tensor, *Pa.*

τ_D, collision damping time, *s.*

φ_{int}, catalyst activity decay.

$\phi_{\perp}$, cross-wise sphericity.

$\phi_{||}$, lengthwise sphericity.

ϕ, standard sphericity.

Acronyms

BNC, Bayonet Neill–Concelman

CFD, Computational Fluid Dynamics.

CPFD, Computational Particle Fluid Dynamics.

CREC, Chemical Reactor Engineering Centre

DEM, Discrete Element Method.

DNS, Direct Numerical Simulation.

EMMS, Energy Minimization and Multiscale

FCC, Fluid Catalytic Cracking.

H-USY, Hierarchical H-style ultra-stable Y

ID, Internal Diameter

LCO, Light Cycle Oil

LOD, length of flow development.

MP-PIC, Multiphase-Particle in Cell.

RNI, Radial Non-Uniformity Index.

RTD, Residence Time Distribution.

TFM, Two-Fluid Model

VGO, Vacuum Gas Oil

1 Introduction

Fluidization is a process where fine solids change into a fluid-like phase through contact with a gas or a liquid. There are several fluidization regimes, ranging from minimum fluidization to fast fluidization, depending on the fluid velocity. These regimes are illustrated in Figure 1.1 (Cocco, Karri, and Knowlton 2014).
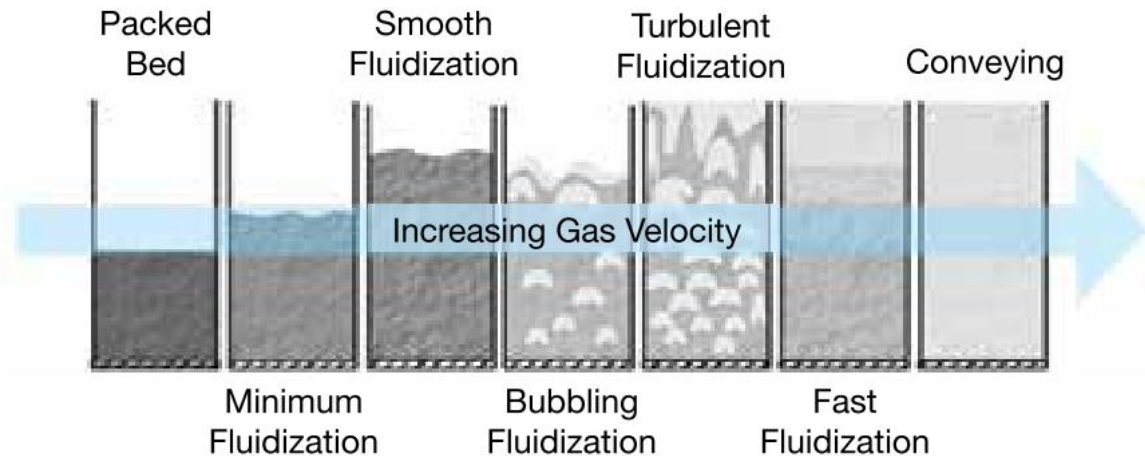
Figure 1.1. Schematic Diagram of Various Fluidization Regimes while Increasing the Superficial Gas Velocity (Cocco, Karri, and Knowlton 2014).

Geldart (Geldart 1973) developed a classification for fluidized systems based on the sizes and densities of particles. Group A particles tend to be aeratable and fluidize well, with particle size ranging from 30 μm to 125 μm, and with densities around 1500 kg/m^3. Group B particles have sizes ranging from 150 μm to 1000 μm. These particles do not undergo smooth fluidization, with bubbles forming as soon as the bed is fluidized. Geldart Group C particles are typically smaller than 30 μm and are difficult to fluidize because of their cohesive nature. They also form channels with fast bubbles that bypass most of the bed. Particles larger than 1000 μm belong in Group D. These powders form enormous bubbles when fluidized and are mostly used in spouting beds (Yang 2003). The Geldart group classification is shown in Figure 1.2.
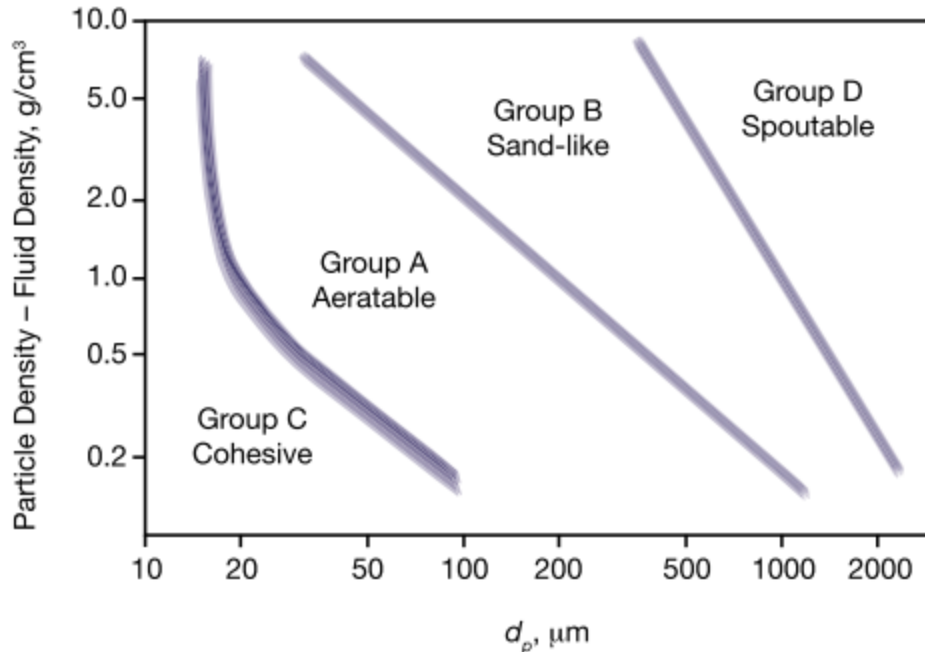
Figure 1.2. Geldart Powder Groups (Cocco, Karri, and Knowlton 2014).

When the gas velocity is sufficiently high, that is, beyond the minimum fluidization point, the particle entrainment rate increases. This means the solids leave the bed and must be fed continuously to maintain the inventory of particles in the system. Under these conditions, the system is a circulating fluidized bed reactor or CFB for short.

The CFBs have significant advantages compared to conventional fluidized beds, such as improved gas-solid contacting, reduced axial dispersion of gas, less tendency towards particle segregation and agglomeration. The riser reactor, where the feed and catalyst move upward, is a typical configuration of the circulating fluidized bed. In this reactor, the catalyst decay is fast, and the catalyst needs to be regenerated constantly.

The most important application of the CFB reactor is in fluid catalytic cracking (FCC) of vacuum gas oil to produce gasoline and other precursors for the petrochemical industry. The FCC unit is present in many refineries and generates approximately 40% of the world's gasoline (Vogt and Weckhuysen 2015). As well, the riser reactor can be found in other industrial and research applications including the roasting and calcination of ores, the combustion of fuels, etc. (J. X. Zhu et al. 1995). A typical FCC unit is depicted in Figure 1.3.
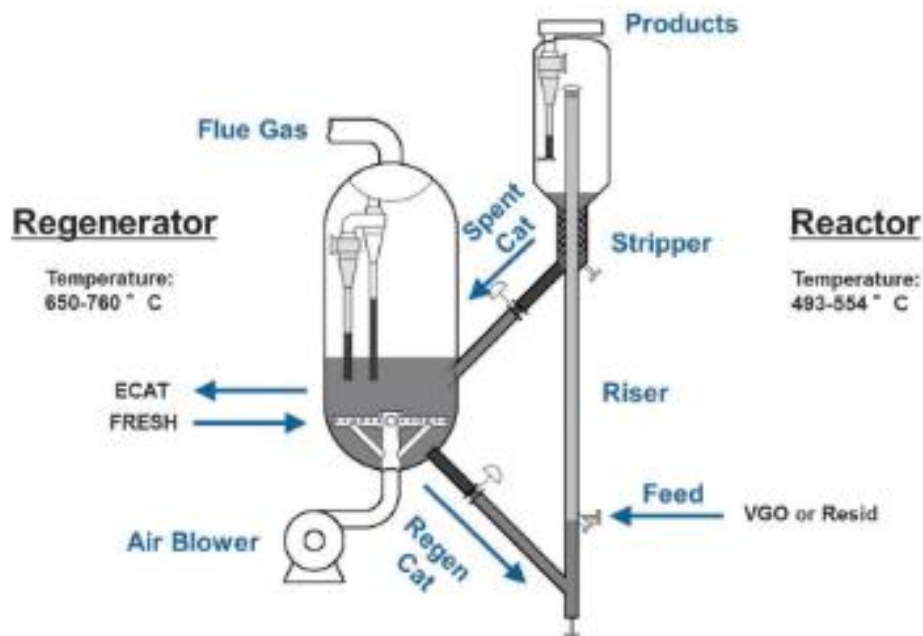
Figure 1.3. A Schematic Description of the FCC Process (Vogt and Weckhuysen 2015).

The catalytic cracking of oil was first developed in the 1940s, using a packed bed reactor with a synthetic silica-alumina catalyst (Armor 2011). The first commercial FCC unit started operating in 1942. It was based on an up-flow reactor and regenerator with a clay-based catalyst (Murphree et al. 1943).

In the early 1960s and 1970s, zeolites, which are synthetic crystalline microporous aluminosilicates, were invented at the laboratories of Union Carbide and Mobil Oil Corporation. The first zeolite relevant for the FCC process was synthetic faujasite or zeolite Y. This zeolite has been the main cracking component in FCC catalysis for more than 50 years (Breck 1964).

The FCC process starts when a hot catalyst is combined with the feedstock at the bottom of the riser reactor. This mixture is rapidly transported up the reactor with a typical contact time of a few seconds. At the top of the riser reactor, the catalyst is separated from the product. At this point in the riser reactor, the catalyst has lost much of its initial activity due to coke deposition. In order to recover the desired activity, the catalyst is transported to the regenerator where most of the coke is burned. Thus, the catalyst is re-used continuously.

The main purpose of the FCC unit in a refinery is to convert heavy gas oil (HGO) and vacuum gas oil (VGO) into useful products, such as liquid-petroleum gas (LPG), olefins, gasoline, light cycle oil, and heavy cycle oil.

Despite the advantages of riser reactors and the developments of the FCC process since its inception, the riser reactor suffers from a non-uniform radial gas and solid flow. This is because of the particle flow against gravity, which induces a backmixing effect, leading to segregation of solids and resulting in a reduced contact between phases, lower conversion, and selectivity towards desired products, i. e. gasoline. (Grace, Avidan, and Knowlton 1997).

Therefore, a new configuration of a reactor called the concurrent downflow fluidized bed reactor was developed. Axial solids dispersion and the nonuniformity of radial gas and solid flow are lower in this reactor since the gas and solids flow in the same direction as the force of gravity. A significant number of papers have been published in the last 25 years, studying the downer hydrodynamics (J. X. Zhu et al. 1995; Z. Wang, Bai, and Jin 1992; Lehner and Wirth 1999; Cao and Weinstein 2000; H. Zhang, Zhu, and Bergougnou 1999; H. Zhang and Zhu 2000; Ball and Zhu 2001; Wu et al. 2007); the gas and solid mixing characteristics of the downer (Wei and Zhu 1996; Wei, Jin, Yu, Chen, et al. 1995; Bang et al. 1999; Yong Jin and Chen 1994); and the potential applications that include pyrolysis and gasification of biomass (Mok et al. 1985; Kim, Lee, and Kim 2001).

Mainly, the downflow fluidized bed, also called downer, reactor has been tested for its applicability in the FCC process (Talman and Reh 2001; Abul-Hamayel 2004). Abul-Hamayel used a pilot plant with a capacity of 0.1 BPD for this purpose (Abul-Hamayel 2004). The results show an increase in the oil conversion, with a higher selectivity towards gasoline and light olefins, under the same operating conditions as a riser reactor. The researchers designated this process as High-Severity-Fluid Catalytic Cracking (HS-FCC), given the flow conditions used for the experiments. For the following tests, the authors increased the capacity of the process to handle 30, 3000, and 30, 000 BPSD (Parthasarathi and Alabduljabbar 2014).

At an industrial scale, a downer unit was built in the Ji'nan refinery for a demonstration, resulting in limited over-cracking and improved selectivity. Two series of experiments

were tested: deep catalytic cracking of vacuum gasoil (VGO) and de-asphalted oil (DAO), and residual oil fluid catalytic cracking (RFCC).

Since the first hydrodynamics studies of the downer, the experimental particle velocity showed a higher value than the theoretical velocity for a single particle (J. X. Zhu et al. 1995). The disparity was attributed to the formation of particle clusters, a phenomenon also observed in the riser reactor. According to Krol et al. (Krol, Pekediz, and de Lasa 2000), the particles agglomerate forming flock and stick structures in the fully developed flow section of the downer.

The mechanisms behind the formation of clusters include turbulence, colloidal interparticle forces, viscous stresses, energy dissipation, and collision between particles (Wylie and Koch 2000). Heat and mass transfer, as well as the residence time, are affected by these clusters. Hence, it is mandatory to investigate the behaviour of clusters in more detail.

Several devices and techniques have been used to study the gas-solid flow in downer reactors, such as: a) capacitive probes (Herbert, P. M.; Gauthier, T. A.; Briens 1998; Sharma 2000), b) laser doppler (Levy and Lockwood 1983; M. Zhang et al. 2003) c) gamma-ray absorption (Yinghui, Zingying, and Jinsen 2012) d) particle image velocimetry (Cate et al. 2002; J. Wang et al. 2005; G. Q. Liu et al. 2008), e) particle tracking velocimetry (Hagemeier et al. 2015), and f) fiber optic probes (Nieuwlan et al. 1996; Xu and Zhu 2010; Werther 1999). Regarding the fiber optic devices, these can be readily implemented. They are able to measure particle volume fraction, cluster velocity, and cluster size simultaneously, presenting an advantage compared to the other techniques.

However, the fiber optic probes are an intrusive device that must be in close contact with the gas-solid flow. To minimize this effect, de Lasa et al. (Young, de Lasa, and Krol 1998) patented a new design called CREC-GS-Optiprobes, incorporating a Graded Refractive Index (GRIN) lens. The lens creates a highly irradiated volume away from the tip of the probe. Only the particles that cross this volume are detected by the sensor. Details of the GRIN lens, the focal region, and the calibration of the device were provided by Islam et al. (Ashraful Islam, Krol, and de Lasa 2011).

Lanza et al (Lanza, Islam, and de Lasa 2012, 2017) performed experiments measuring the gas-solid flow, determining the characteristics of individual clusters in the fully developed flow section of the downer. The authors developed a method to eliminate noise by setting a baseline according to the solid mass flux.

A powerful tool to help in the modelling and optimization of chemical reactors is computational fluid dynamics. It allows one to obtain an approximate solution for the complex system of equations, that describe the behaviour of gas-solid flows. The acceptance of CFD methods in the scientific community to design, scale-up, and optimize multiphase reactors has increased over time. However, there are still challenges to overcome, related to the insufficient computational capacity for simulations to recreate real scale gas-solid flow with a high population of particles (Cocco, Fullmer, and Liu 2017).

In CFD simulations, the particle motion can be averaged and replaced by the motion of a continuum, representing the flow field with an Eulerian frame of reference. The gas-solid flow is described as an interpenetrating continuum in an Eulerian-Eulerian or two-fluid model. The governing equations can be obtained from either an averaging or mixture theory approach (Gidaspow 1992). Although this methodology has been previously used to model the downer reactor (Yi Cheng et al. 1999; Ropelato, Meier, and Cremasco 2005; Chalermsinsuwan et al. 2012), since particles cannot behave entirely as a fluid, this modeling approach cannot lead to completely accurate results. Thus, for an in-depth understanding of the flow phenomena, a more rigorous physical model is required (Cocco, Fullmer, and Liu 2017).

If instead, one would like to track the particles and follow their trajectory, the gas-solid flow should be specified in a Lagrangian frame of reference, allowing for greater detail at the particle level. There are several approaches with varying degrees of modeling and computational effort which could be used, such as:

a) The Direct Numerical Simulation, where all scales of the fluid flow are completely resolved with a no-slip condition applied on the surface of each particle. Additionally, no closure laws are required. This approach is the easiest to model but it consumes the most computational resources (Hao et al. 2009; Tang, Yali; Peters, E.; Kuipers 2016).

b) The Lattice-Boltzmann Method (LBM), which resolves the flow around the particles with the eponymous equations and tracks the particle motion by solving Newton's equations of motion. This approach is less computationally intensive (Beetstra, van der Hoef, and Kuipers 2007).

c) The Discrete Element Method (DEM) which does not resolve the flow around the particles, reducing the computational cost. However, additional models for the gas-solid drag have to be developed (Tsuji, Kawaguchi, and Tanaka 1993; H. P. Zhu et al. 2007, 2008; M. H. Zhang et al. 2008; Cocco, Fullmer, and Liu 2017).

Under the current capacity, it is possible to track tens of millions of particles using the DEM model. However, this remains insufficient, given that an industrial application such as an FCC reactor, contains over a trillion particles (Cocco and Hrenya in Syamlal 2007).

Thus, to reduce the computational time, the particle contact can be reduced by obtaining the collisional stresses from an Eulerian grid. This can be achieved with the Multiphase Particle in Cell Method (MP-PIC). This is a discrete particle numerical method that employs a fixed Eulerian grid, with the fluid phase being treated as a continuum and the particles being treated as Lagrangian groups of particles with similar properties, also called computational clouds or parcels. Snider et al. (Snider 2001) implemented the MP-PIC in a three-dimensional simulation, starting from the single-phase Particle-in-Cell Method (O'Rourke, Brackbill, and Larrouturou 1993; Andrews, M. J., O'Rourke 1996). Particle interactions and properties were interpolated to the grid. The flow field was updated and then interpolated back to the particles. Thus, the gas-solid flow was coupled through mass, momentum, and energy interphase transfer.

Furthermore, the MP-PIC method has been used to model the downer hydrodynamics. Abbasi et al. (Abbasi 2013) executed simulations using the MP-PIC method with the Barracuda VR software. These authors observed periodic solid densification, with zones of high particle volume fraction. They noticed a "wavy" flow, promoting circumferential gas flow, being more apparent at the end of the downer.

To consider the particle clusters formed in the downer, Lanza et al. (Lanza and de Lasa 2016) developed a Hybrid Numerical Cluster model and implemented it in Barracuda VR,

using an experimental cluster size distribution and simulating two downers of different cross-sectional area. The particle clusters were modeled as non-spherical particles and the Ganser drag correlation was selected for their simulations. The results showed an accurate description of the gas-solid flow in the fully developed flow section of the downers, indicating a lower near-wall influence of the downer with a larger diameter.

Despite the extensive research work reported in the literature, focusing on the downer reactor, the acceleration section has been overlooked, with only a few studies focusing on the entrance effect. Furthermore, there is no individual cluster information reported for this region. Since this is where the initial contact occurs, and where the cluster behavior affects the mixing and residence time, it is necessary to study the cluster characteristics to build a reliable model for the successful scale-up.

Chapter 2 summarizes the literature review on downflow reactors, hydrodynamics studies, cluster behaviour, and CFD models. Chapter 3 outlines the main objectives of the project. Chapter 4 describes the experimental equipment used to obtain the data reported in this dissertation and elaborates on the methodology to analyze the data and obtain the individual cluster characteristics.

Chapter 5 reports the experimental results of particle clusters and is based on a first publication, entitled "Cluster Acceleration and Stabilization in a Downflow Circulating Fluidized Bed Unit". This peer-reviewed article was published in *Industrial & Engineering Chemistry Research*, 2020, 59, 12360. Impact Factor: 3.573

Chapter 6 describes the mathematical modeling of cluster dynamics, and the constitutive equations used in the CPFD simulations, to describe the gas-solid flow in the downer reactor.

Chapter 7 reports the results from the CPFD simulations of the cold-flow model unit, and the model validation with the experimental data. This chapter is partially based on a second publication entitled: "Hybrid Particle Cluster CPFD Simulation in the Acceleration and Stabilized Sections of a Downflow Circulating Fluidized Bed", published in *Industrial & Engineering Chemistry Research*, 2020, 59, 20325. Impact Factor: 3.573.

Chapter 8 reports the CPFD simulations of the catalytic cracking of gas oil in a downer reactor using a five-lump kinetic model, with the evaluation of the catalyst-to-oil ratio effect on the outcome of the process.

Chapter 9 outlines the conclusions, research outcomes, and future work recommendations.

2 Literature Review

2.1 Downer Reactor Units

The development of downer reactors for the catalytic cracking of oil started in the 1940s with patents by Standard Oil (Munday 1947).

Later on, a new attempt to develop a downflow reactor was made by Stone and Webster in the early 1970s. This idea was further developed by Gartside and Ellis in the "Quick Contact" Reactor (Gartside 1989). This reactor was composed of a gas-solid mixer with a jet impinger to ensure adequate mixing for reactions, a downflow reactor section, a gas-solid separator, with a residence time of approximately 200 ms. Following a similar design, Berg (Berg, Briens and Bergougnou, 1989) designed the Ultra-Rapid Fluidized Reactor used for biomass pyrolysis and called it "Short Contact Time Fluidized Reactor" (Bassi, Briens, and Bergougnou 1994).

Mobil, Texaco, and Shell patented their versions of downer reactor for FCC (Gross and Ramage 1983; Niccum and Bunn 1985; Dewitz 1989). The contact time for these reactors was lower compared to that of the riser reactor. However, hydrodynamic studies are still being performed to fully implement downer reactors in the refining and the manufacture of chemicals.

The downflow reactor consists mainly of a distributor located at the top; a column where the main reaction is occurring, it usually has a circular cross-section but a square or a rectangular configuration may also be used; the separator to recover the desired products. Each of these components must be carefully designed for an adequate reaction performance.

2.2 Gas and Solid Distributor

The uniform distribution of solids is crucial in a downer. In downers, particles are accelerated by drag force and gravity. The role of the distributor at the entrance of the downer is to ensure good mixing of the gas and solid phases. Several distributor designs have been proposed previously. Zhang et al. (H. Zhang, Zhu, and Bergougnou 1999)

proposed a distributor in a minimum fluidization regime with the particles entering the reactor through several orifices, shown in Figure 2.1.
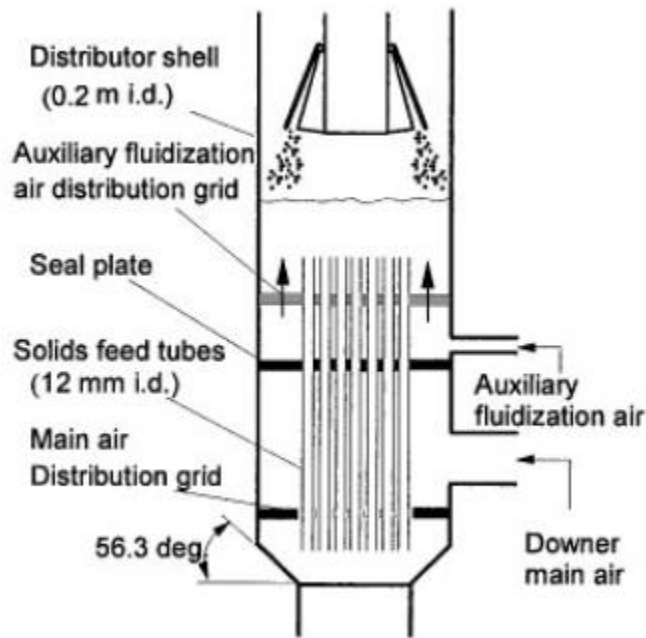
Figure 2.1. Downer Distributor (H. Zhang, Zhu, and Bergougnou 1999)

Berg et al (Berg, Briens, And Bergougnou 1989) proposed a distributor for critical solid-solid mixing, with jets through which flow solid particles. These jets impinge on each other at the center to promote intermixing.

Figure 2.2 a and b (Cao et al. 1995; Lehner and Wirth 1999) share the same principle using a fluidized bed feeder to ensure good gas-solid mixing. Figure 2.2c and d (Muldowney 1995; Y Jin et al. 2000) consider an upflow vaporizer given catalyst/oil mixing is considered more effective in upflow mode.

The gas-solid distributor on top of the downer influences the flow pattern in the reactor, especially in the region near the distributor. However, after a sufficient length, the flow behaviour is stabilized and becomes independent from the entrance structure.

a)

solids inlet

air for
distributor

air inlet   air inlet

downer

b)

primary air

secon-
dary air

$d_i = 60$

$d_i = 75$

solids

fluidized
bed

538

fluidizing air

diffusor

$d_i = 150$

c)

130

150

125

100

120

110

115

CATALYST

OIL

160

d)

catalyst carrier
gas
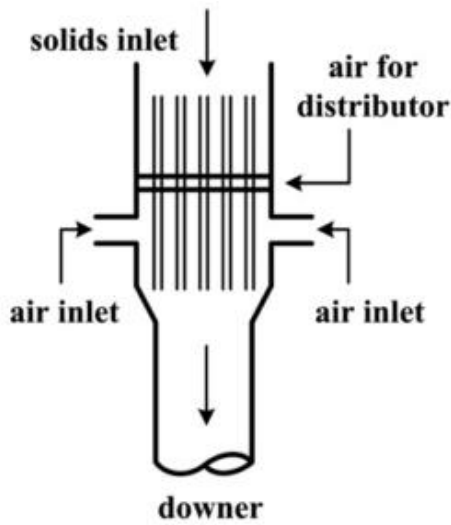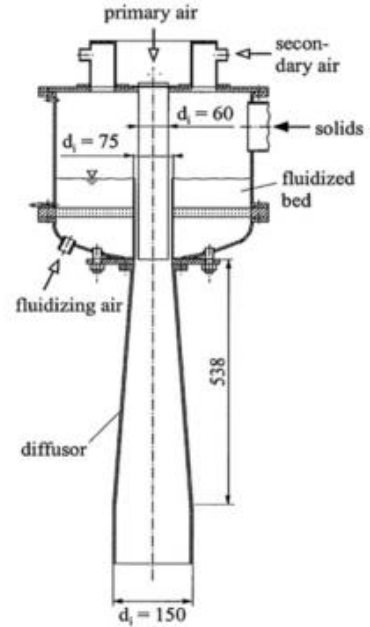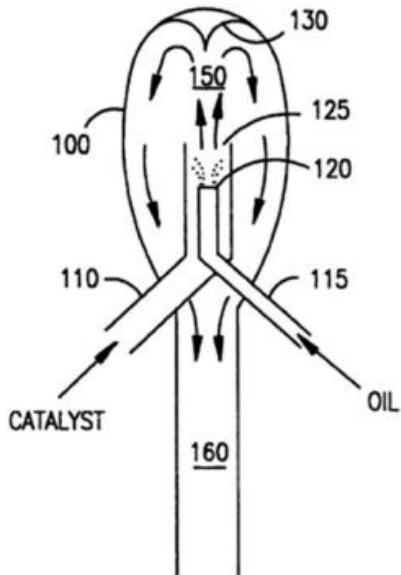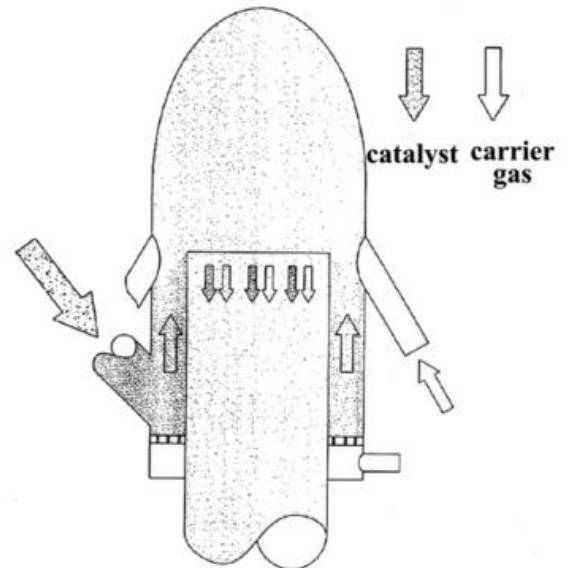
Figure 2.2. Inlet Configurations of Downers in the Literature. a) Cao et al. (Cao et al. 1995), b)Lehner and Wirth (Lehner and Wirth 1999), c) Muldowney (Muldowney 1995), d) Jin et al. (Y Jin et al. 2000)

The effect of the nozzle angle on the flow was studied at Tsinghua University (Qian 2006), using two angles for the injection, 30° and 45°. An optic density sensor captured the radial solids distribution, as reported in Figure 2.3.
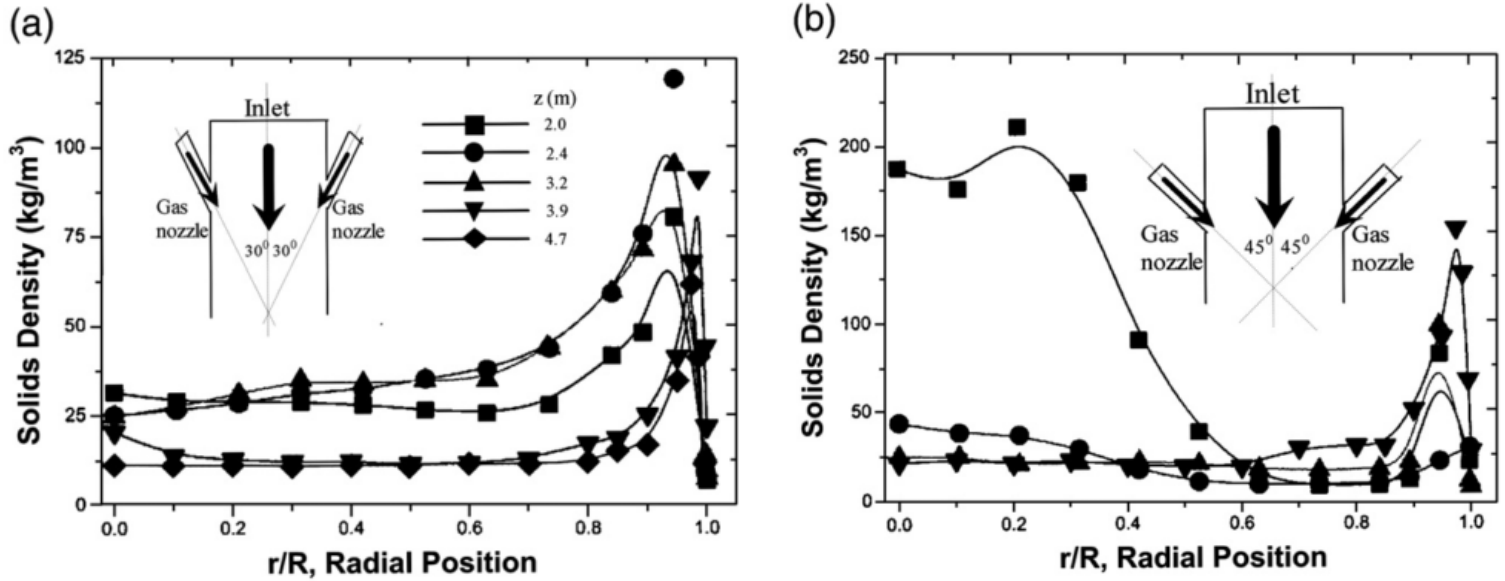
Figure 2.3. Influence of Gas Nozzles at the Downer Inlet on the Solids Fraction Distribution. a) 30° gas nozzle; b) 45° gas nozzle. (Qian 2006)

Upon injection, the solids flow was redistributed and stabilized after a relatively short distance. However, when using the 45° nozzle, a much denser flow of solids in the central region of the downer was formed. This region was strongly turbulent and fast-moving. Thus, the 45° angled nozzle needed a shorter distance from the feeding level to redistribute the solids uniformly compared to the 30° nozzle.

2.3   Gas-Solid Separator

Depending on the reaction, the contact time between the gas and the particles in the downer can range from fractions of a second (Bassi, Briens, and Bergougnou 1994) to several seconds (Rostom and de Lasa 2019; Ahmed and de Lasa 2020). In the case of faster reactions, rapid separation is crucial.

For this purpose, Gartside (Gartside 1989) developed a quarter turn cyclone separator as described in Figure 2.4a. They achieved a separation time of 30 milliseconds with a 98% efficiency.
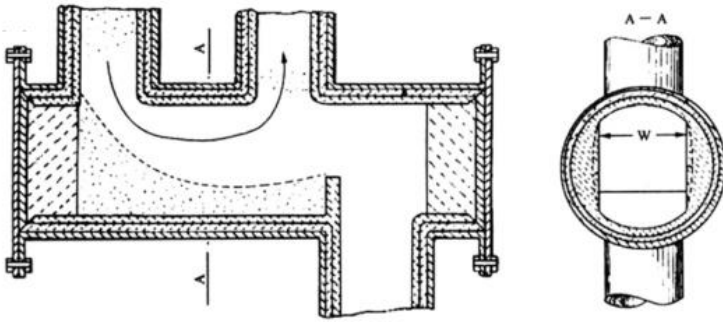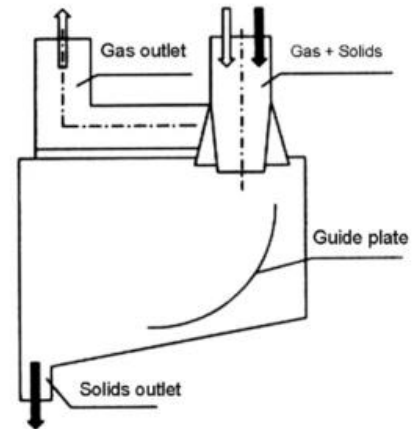
Figure 2.4. Gas-Solids Fast Separators. a) Gartside (Gartside 1989), b) Qi et al. (Qi et al. 1990)

Tsinghua University (Qi et al. 1990) developed an inertial separator where the two phases flow through a nozzle and impinge on a curved guiding plate, with separation times ranging from 0.05 to 0.3 s. This separator is shown in Figure 2.4b.

In the case of reactions taking place over several seconds, such as in FCC, a conventional cyclone separator can be used.

2.4 Measurement Techniques

The gas-solid flow in circulating fluidized beds has been studied using a number of techniques and devices, each with its advantages and drawbacks. They can be classified into two main groups: intrusive and non-intrusive.

2.4.1 Non-intrusive techniques

2.4.1.1 Laser-Doppler Velocimetry

A non-intrusive technique was introduced by Levy (Levy and Lockwood 1983), called laser Doppler velocimetry. This technique is based on the scattering of coherent light by particles passing through two crossed laser beams. When a particle traverses the measurement volume, it creates a Doppler signal, where the fluctuations of the light intensity are proportional to the particle velocity. This method does not indicate the particle trajectory and is limited to systems with transparent walls and very diluted particle concentrations.

Zhang (M. Zhang et al. 2003) studied the flow structure in a riser/downer coupled circulating fluidized bed, with a dual-optical fiber density probe and a laser Doppler Velocimeter (LDV) system. From the analysis of the probability density distribution of transient velocity signals obtained by LDV, it was shown that the dispersed particle phase, conformed by small, short-lived clusters, prevails in the downer.

2.4.1.2 Gamma-Ray Computed Tomography

Gamma-ray computed tomography is a non-intrusive technique that determines the density distributions of solids in the reactor cross-section by using a set of radiation attenuation measurements. The measurements are taken along beam paths through the reactor from several directions around it, forming a projection. This method, however, only determines the volume fractions of the gas-solid mixture. It has to rely on other techniques for the measurements of particle velocities (Bhusarapu, Al-Dahhan, and Duduković 2006). Bartholomew and Casagrande (Bartholomew and Casagrande 1957) were the first to apply this technique in a riser reactor using a Cobalt-60 source. Given that the measurements were non-invasive, it was determined that they could be performed in existing industrial units. However, it was noted that the operation of the equipment had to remain steady for the duration of the measurements, which could take as long as 18 hours (Werther 1999).

2.4.1.3 Particle Image and Tracking Velocimetries

Particle image velocimetry (PIV) is a non-intrusive, image-based technique used to obtain the velocity of particles in a gas-particle flow using tracers. A camera records two images and the particle shift is determined by using a cross-correlation function. The time gap is obtained from the recorded frequency of the camera. The PIV is based on the intensity distribution. It does not track the particles directly. Microscale quantities like collision rates of particles are not provided by PIV.

Particle tracking velocimetry (PTV) is another image-based measurement technique to determine particle velocities in a Lagrangian reference frame. Using this technique, several algorithms have been developed for the search of corresponding particles. However, only a few PTV studies have been performed using particulate multiphase flows (Capart, Young, and Zech 2002). The PTV and PIV techniques are limited to pseudo-2D

configurations because the particle systems must be accessible to the high-speed camera and the illumination source. The PTV is almost identical to the PIV but at smaller fields of view and shorter observation times. This generates information on particle-particle interactions.

2.4.2 Intrusive techniques

2.4.2.1 Capacitance probes

Capacitance probes are a device that measures the local, time-dependent concentrations of particles in a suspension through the dielectric constant of the mixture. A commercial amplifier supplies a fluctuation charge of constant amplitude to the sensing surface through a conductor that is surrounded by a guard conductor (Louge and Opie 1990; Herbert, P. M.; Gauthier, T. A.; Briens 1998; Tuzla, K. Sharma 1998). Tuzla et al. used capacitance probes to measure the transient dynamics in the downer reactor, detecting the concentration of solids at 4.8 m from the downer entry. The measurements allowed the detection of clusters, at a duration time of approximately 0.2 seconds. The results also indicated that at any local position, clusters exist during 3 to 4% of the time.

2.4.2.2 Fiber Optic probes

The fiber optic probes are a device designed to register the light reflections from the particles that pass in front of the sensor. The downside of the conventional design is the close contact with the solid phase, given that the measuring region is immediately adjacent to the probe. To address this issue, de Lasa et al. developed a new design for a fiber optic prob designated as CREC Optiprobes, with a Graded Refractive Index (GRIN) lens (Sobocinski, D. A.; Young, B. J.; de Lasa 1995), that redirects the light, creating a measuring volume, with high irradiated energy density, away from the tip of the probe. Furthermore, the size of the focal region is in the same order of magnitude as the particles. This results in the ability to measure the characteristics of particles, such as cluster size. The optic probe also allows the measurement of the particle volume fraction and particle velocity, simultaneously.

Lanza (Lanza, Islam, and Lasa 2016b) developed, for the CREC Optiprobes, a baseline setting methodology to study individual particle clusters size and velocity, in the fully developed flow section of two downers with different cross-sectional areas.

2.4.3 Hydrodynamic behavior

The particle phase both in riser and downer units is affected by the same forces, drag, and gravity. However, these forces act in dissimilar ways in riser and downer units, and their effects depend on their radial positions. In the case of the riser, the drag force dominates in the centre because of a higher particle velocity. At the near-wall position, the gas velocity is lower, and the gravity force is more dominant. The effect of gravity in risers causes aggregation. This results in the solids slipping downward and the characteristic non-uniform radial profile.

In the downer reactor, particle aggregation still occurs near the unit wall, increasing, as a result, the particle downward velocity, which in turn restricts further aggregation. Thus, overall, there is a more uniform radial flow structure in the downer reactor.

2.5   Axial gas and solid flow structure

Wang et al. (Z. Wang, Bai, and Jin 1992), performed one of the first studies on downers. These authors collected pressure, gas, and particle velocity data in a 5.8 m high unit. More recently, Zhang (H. Zhang, Zhu, and Bergougnou 1999; H. Zhang and Zhu 2000) measured solid concentration, pressure, particle, and gas velocity. The experimental data were obtained along the radius, for 11 operating conditions and at 8 different axial levels.

2.5.1 Particle velocity profile

From the results of the study, Wang et al. established that the downer reactor has three clear sections:

a) At the entrance of the unit, particles are accelerated by gravity and drag, and gas attains a high velocity. When particle velocity becomes equal to the gas velocity, the gas drag acting on the particles becomes zero. This section, which extends from the inlet to this axial position, is called first acceleration section.

b) Following the acceleration section and, due to gravity, solids are further accelerated and the particle velocity exceeds the gas velocity. Given this effect, the drag force now acts in the opposite direction as gravity. In this second acceleration section, particles keep accelerating as long as the gas drag is less than gravity.

c) When the drag becomes equal to gravity, the particle velocity levels off, namely, solids reach the terminal velocity. The section in which this takes place is designated as the constant velocity or developed flow section.

2.5.2   Gas velocity

In the first acceleration section, the gas velocity decreases due to the gravitational and drag forces acting on the particles. In the second acceleration region, the gas velocity decreases slightly due to the comparatively reduced acceleration of the particles. In the constant velocity section, the gas velocity becomes constant given that the particle acceleration is negligible. Figure 2.5 reports the changes in particle velocity, gas, and particle voidage along the downer, as well as the effect of different experimental conditions.
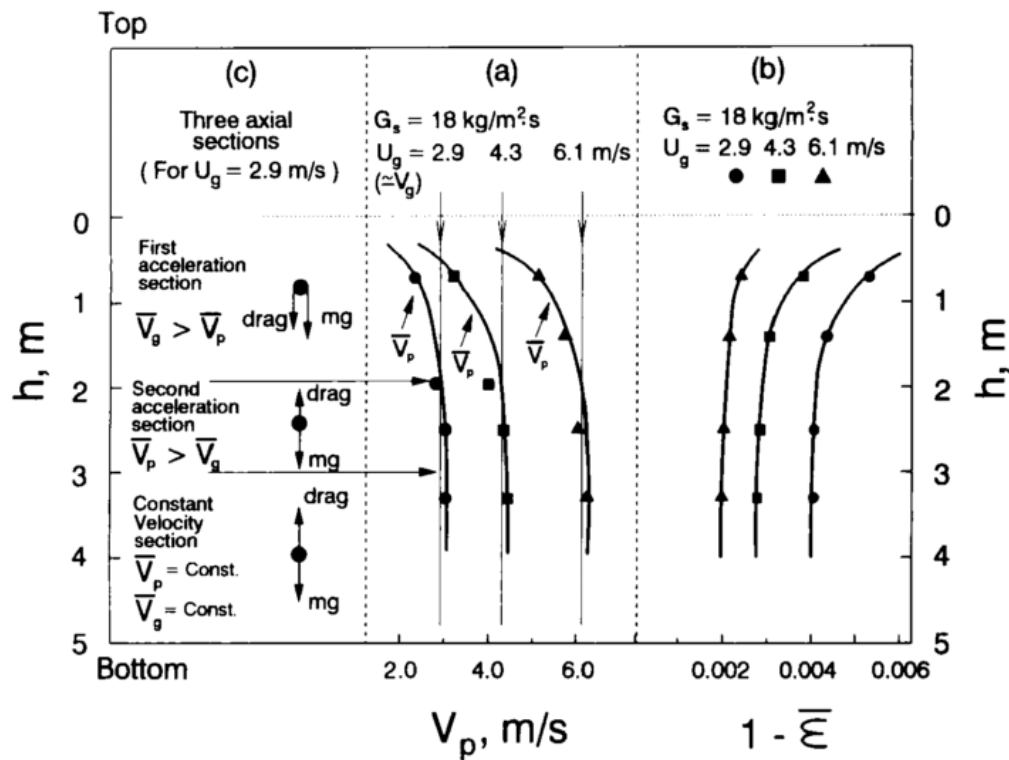
Figure 2.5. Axial Gas-Solid Flow Structure (J. X. Zhu et al. 1995)

2.5.3   Solids Concentration

The particle concentration or particle volume fraction is a key parameter for downer unit operation and modeling. This particle volume fraction has a higher value in the near

entrance region of the downer. However, after some time, it reaches a constant value. It must be noted that the concentration of solids in downers is lower compared to the values obtained in risers. In downers, the solids holdup reaches a constant value in a shorter axial downer section. Given particle velocity and solid hold up are inversely proportional, this leads in downers to a higher particle velocity and lower particle volume fraction.

2.5.4 Axial pressure profiles

The pressure drop in the downer reactor is a function of the concentration of solids and can be represented by the following equation:

$$\Delta P = P_2 - P_1 = \Delta L g \rho_{susp} - \Delta P_a \qquad (2-1)$$

where P_1 and P_2 are points along the downer, $\Delta L g \rho_{susp}$ is the static head due to suspension holdup and P_a is the pressure loss due to the acceleration of solids.

At the entrance of the downer, where the drag force is zero, the pressure drop caused by the particle acceleration is equal to the static head. Hence, in this case, the total pressure drop is zero.

In the first acceleration section, the P_a exceeds the static head. Therefore, the pressure drop is negative, and the absolute pressure decreases in this section. In the second acceleration region, the P_a is lower than the static head, making the pressure drop positive with the absolute pressure increasing. Furthermore, in the constant velocity section, the acceleration is zero, and the pressure drop is constant. Finally, and from this point, the absolute pressure increases linearly along the downer. Figure 2.6 shows the axial profiles of pressure and pressure gradient.

a)
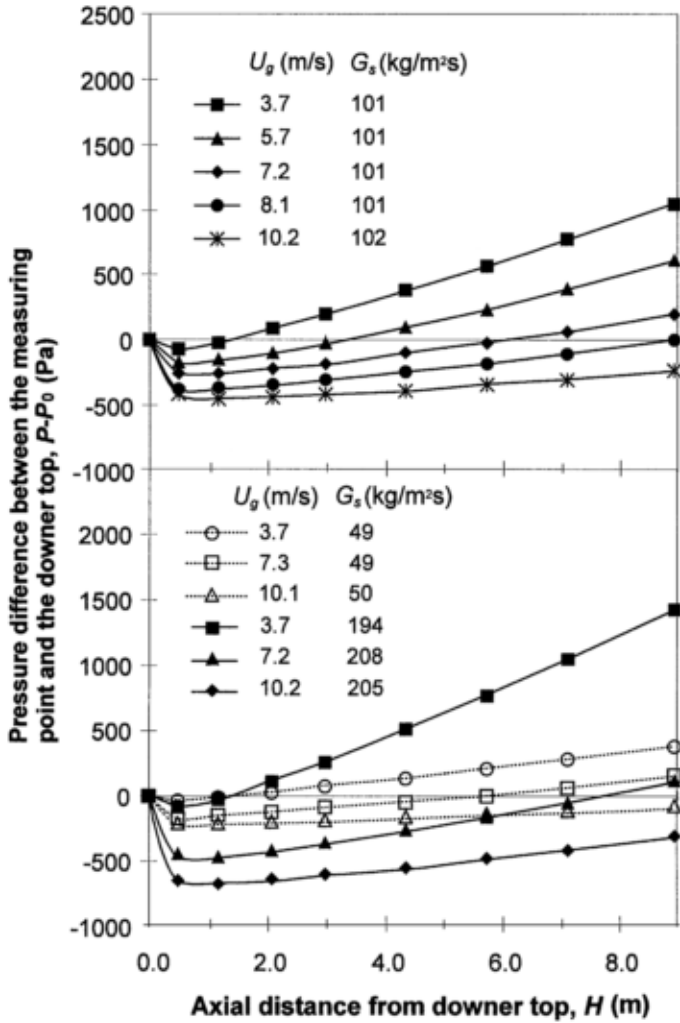
b)
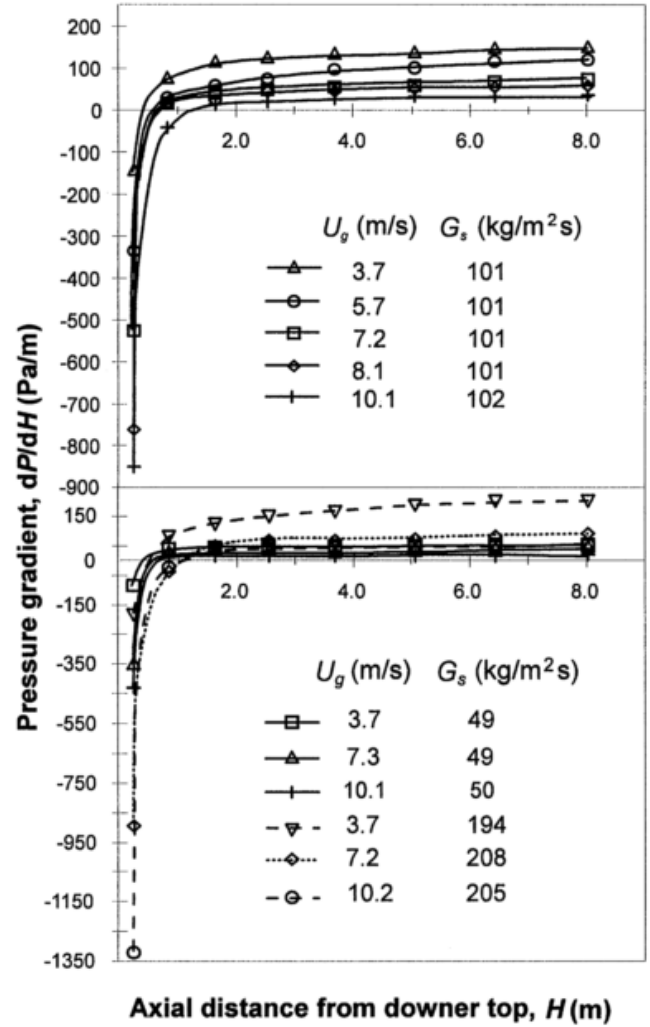
Figure 2.6. a) Axial Pressure, b) Axial Pressure Gradient along Downer. (H. Zhang, Zhu, and Bergougnou 1999)

2.6 Radial Gas and Solid Flow Structure

2.6.1 Solids Concentration Distribution

The solid phase concentration, also called particle volume fraction, is a key characteristic of the gas-solid flow and a necessary parameter for calculating solids flow and kinetic modeling. Previous studies, e. g. Wang et al. (Z. Wang, Bai, and Jin 1992), reported the radial profiles of particle volume fraction at different axial positions. The results showed a more uniform radial profile along the whole downer column compared to that of the riser reactor. However, a peak was still observed near the wall, located between 85%-96% of

20

the total radius. Zhang (H. Zhang, Zhu, and Bergougnou 1999) measured the radial solids concentrations. Their results are shown in Figure 2.7.
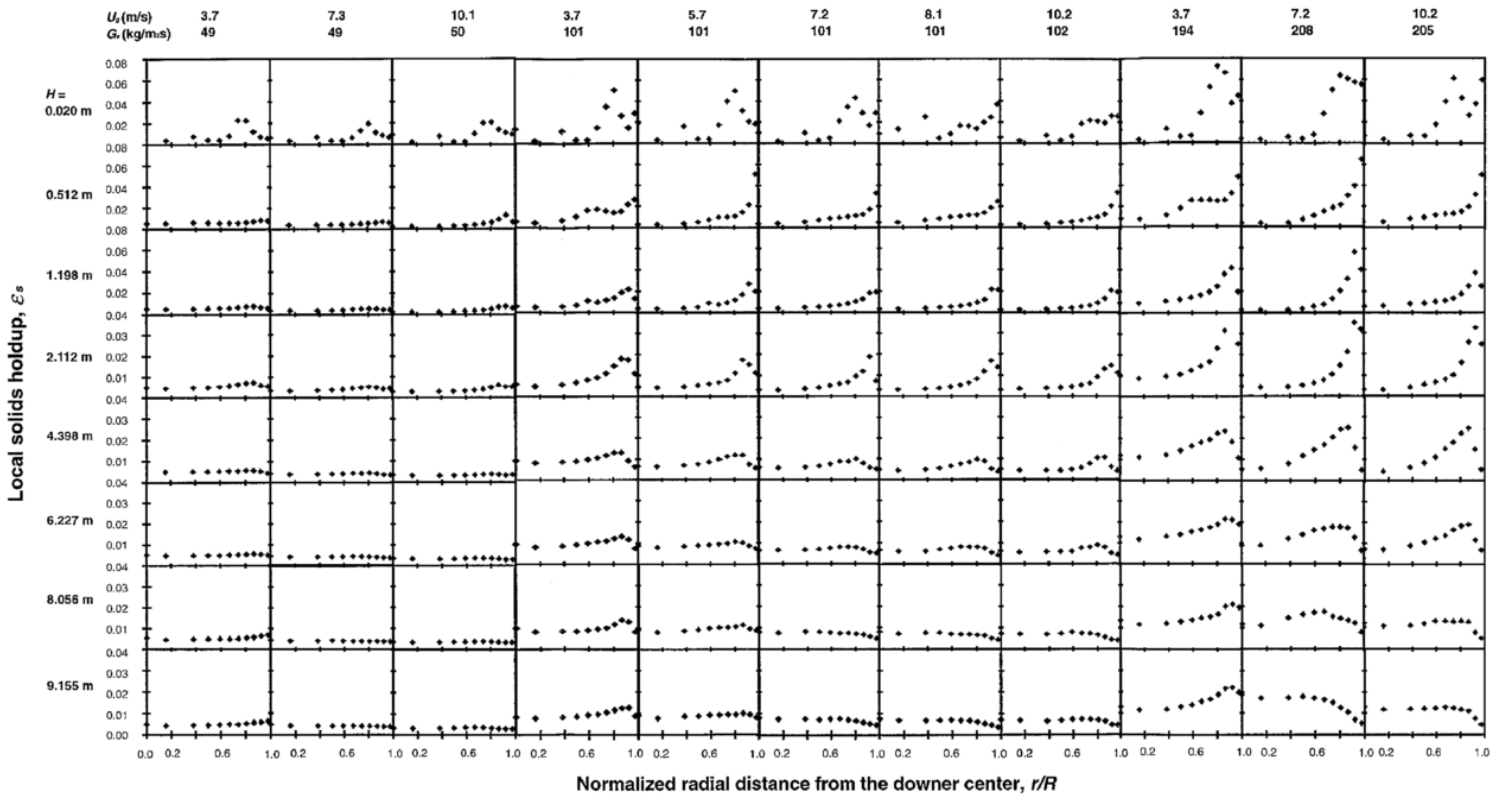
Figure 2.7. Radial Solids Holdup Profiles along the Downer under Different Operating Conditions (H. Zhang, Zhu, and Bergougnou 1999).

In the same study, Zhang et al. reported a dilute core/dense annulus radial structure at superficial gas velocities below 4 m/s. Meanwhile, the opposite structure, a dense core/dilute annulus was observed at a gas velocity above 5 m/s.

2.6.2 Gas velocity radial distribution

A study by Zhu et al. (J. X. Zhu et al. 1995) showed that the radial gas velocity profiles as shown in Figure 2.8. One can notice a relatively flat radial gas velocity profile, with the maximum gas velocity corresponding to the high solid concentration near the wall.
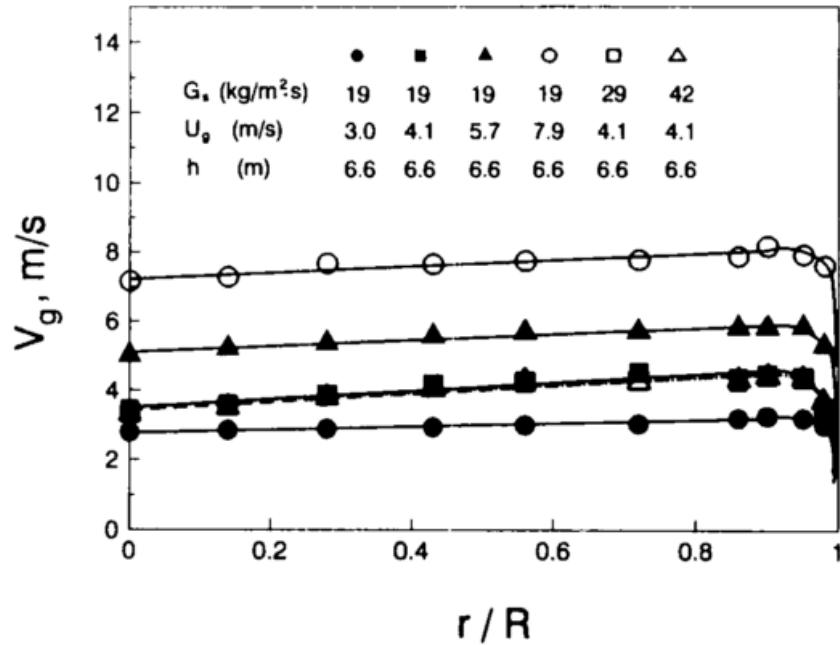
Figure 2.8. Radial Gas Velocity Distribution. (J. X. Zhu et al. 1995)

The gas velocity is rather unaffected by the solid mass flux and axial position (Cao et al. 1995).

2.6.3 Particle velocity

Zhang et al. (H. Zhang and Zhu 2000) conducted studies on particle velocity, which are shown in Figure 2.9. Near the entrance of the downer, a "distributor effect" can be seen, with fluctuations occurring along the radius. However, at a longer length in the downer, the radial profile develops further and reaches the constant velocity section. The typical developed profiles in this section are characterized by a relatively flat core, where the particle velocity slightly increases with the radial position, and an annulus where the particle velocity drops near the wall.
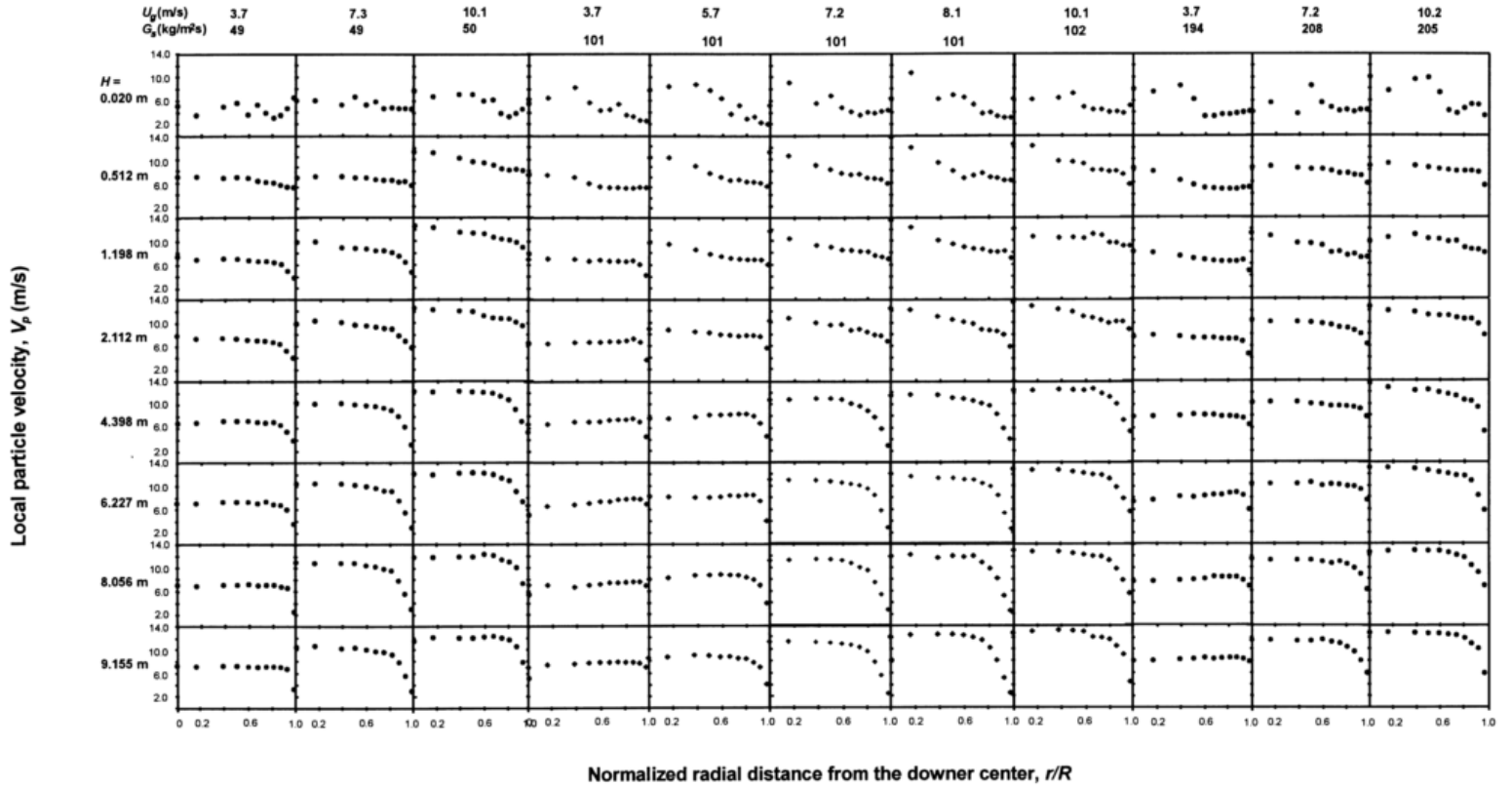
Figure 2.9. Radial Profiles of Particle Velocity along a Downer under Different Operating Conditions. (H. Zhang and Zhu 2000)

2.7 Radial Non-Uniformity Indices

Zhu and Manyele (Zhu, Jesse; Manyele 2001) proposed a Radial Non-uniformity Index (RNI) to characterize the radial flow structures in various fluidized systems, including gas-solids two-phase flow systems. An RNI was applied to the solids holdup as shown in the equation below.

$$RNI(\epsilon_s) = \frac{\sigma(\epsilon_s)}{\sigma(\epsilon_s)_{max}} = \frac{\sigma}{\sqrt{\bar{\epsilon}_s(1 - \epsilon_{mf} - \bar{\epsilon}_s}} \tag{2-2}$$

Where $\sigma(\epsilon_s)$ is the standard deviation of the radial solids holdup profile, $\sigma(\epsilon_s)_{max}$ is the normalizing parameter, $\bar{\epsilon}_s$ is the cross-sectional average solids holdup, and ϵ_{mf} is the solids holdup at minimum fluidization. The normalizing parameter, $\sigma(\epsilon_s)_{max}$, is the maximum possible standard deviation which is obtained from a set of solids holdup data having values of either 0 or ϵ_{smf} (extreme values) and with the same average solids

23

holdup as the one from the experiment data to be compared to. Figure 2.10 provides a comparison of $RNI(\epsilon_s)$ as a function of axial position at 11 operating conditions.
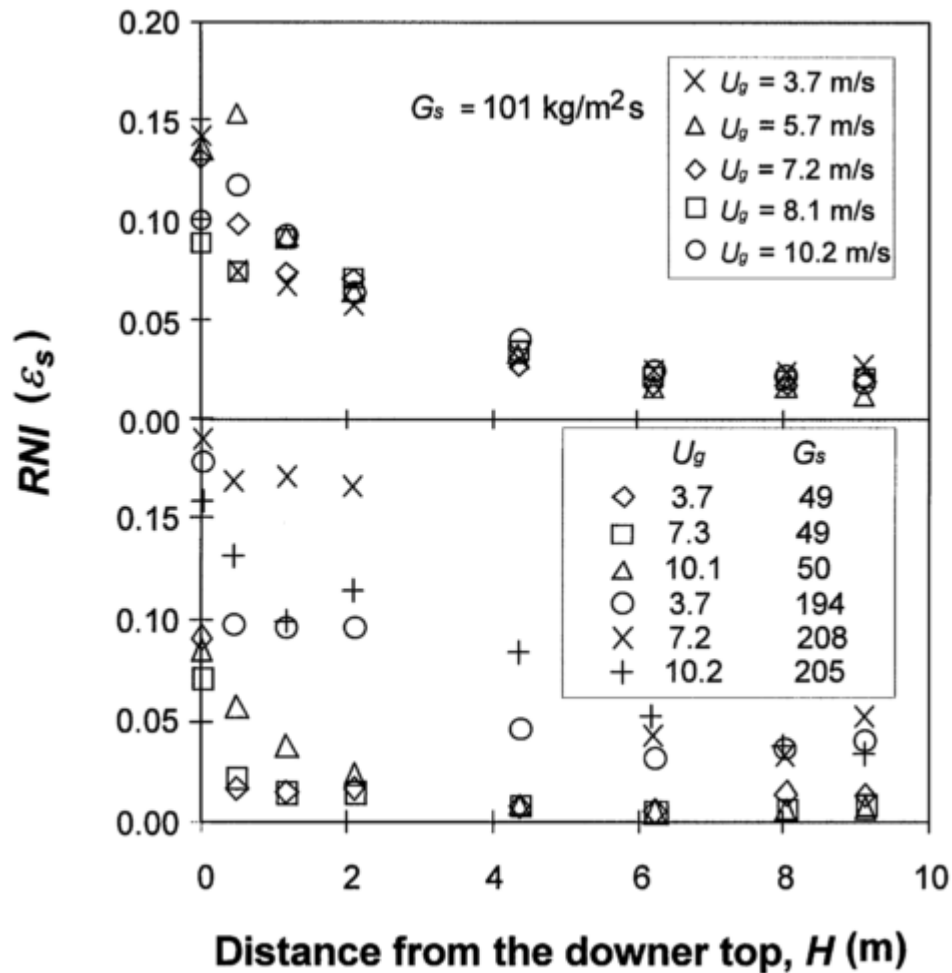
Figure 2.10. A Comparison of Axial Profiles of RNI under Different Operating Conditions (H. Zhang, Zhu, and Bergougnou 1999)

The trend for all conditions studied is that the Non-Uniformity Index is high at the downer entrance and gradually decreases along the column. Figure 2.10 shows that with an increase in G_s at a fixed U_g, the radial solid fraction non-uniformity of solids holdup largely intensifies. An increase in U_g has no noteworthy influence on the RNI, in the lower section of the downer.

The RNI calculated for downers and risers further shows a higher degree of uniformity of flow in the downer unit as shown with the RNI index profiles. Figure 2.11 shows the RNI profiles for each reactor.
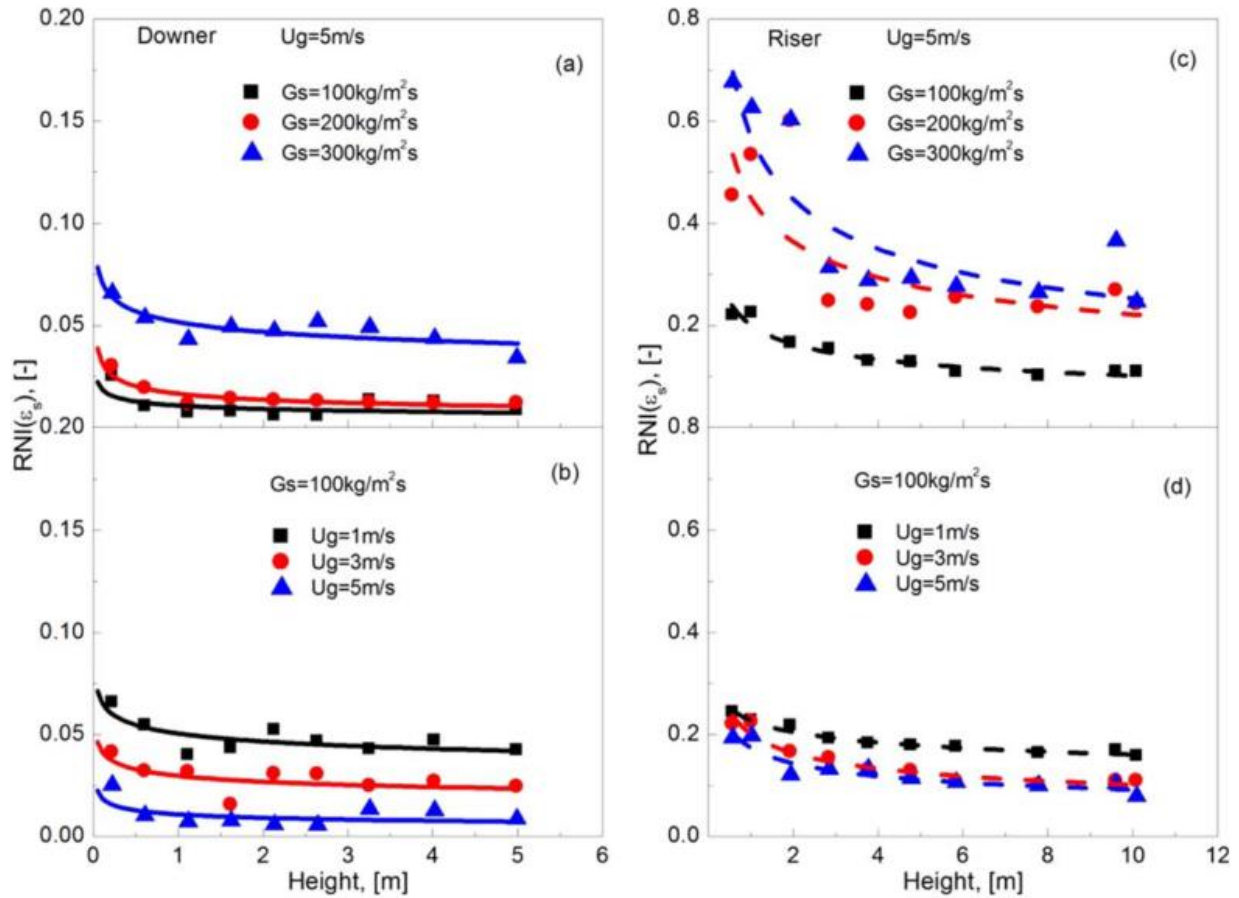
Figure 2.11. RNI of Solids Holdup Along the Riser and Downer (Wang, Chengxiu; Li, Chunyi; Barghi, Shahzad; Zhu 2015)

2.8   Intermittency Indices

Another tool previously used to evaluate the gas-solid flow in circulating fluidized beds is the intermittency index, which compares the time variations of solids holdup between risers and downers. A high intermittency index is a sign of a more segregated flow. Zhang et al. (H. Zhang, Huang, and Zhu 2001) reported Intermittency Index values for both risers and downers. Their results indicate a variation of the values between the center and near-wall regions, at the entrance of the downer. This is reduced in the fully developed flow region and is shown in Figure 2.12.
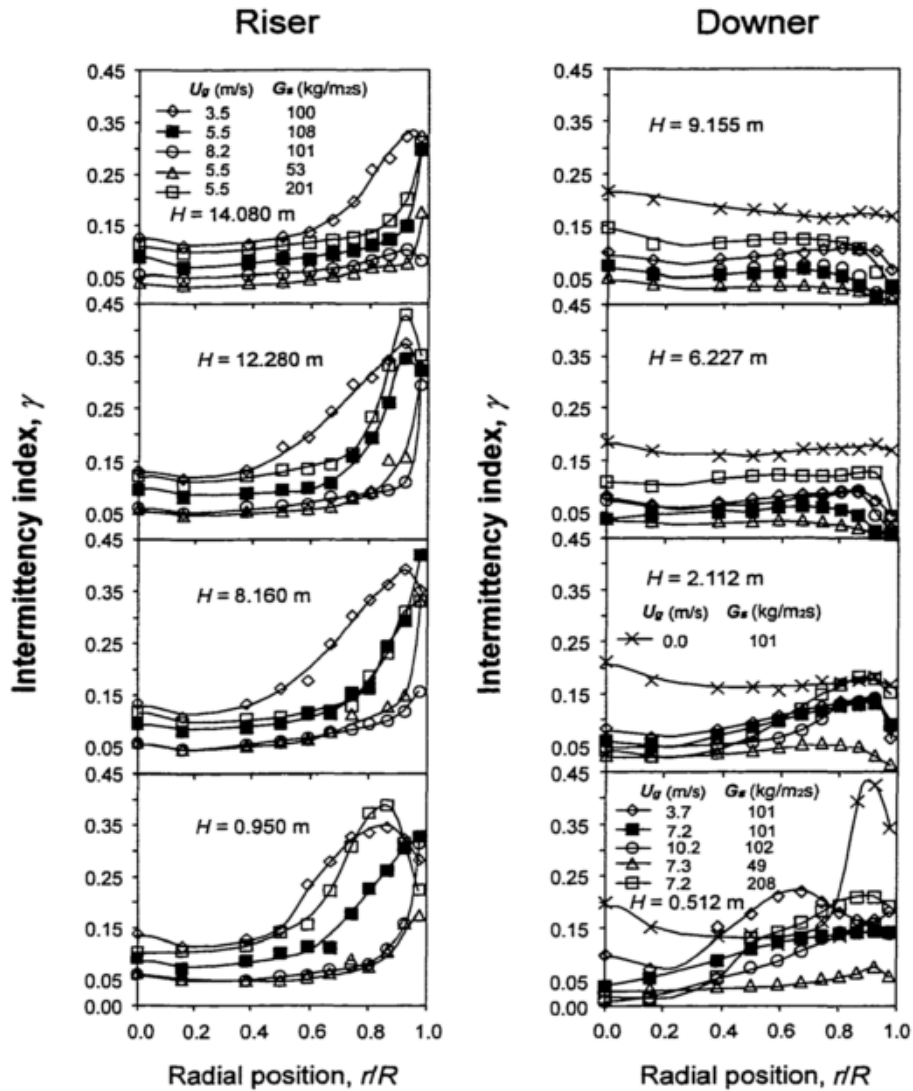
Figure 2.12. Radial Profile of Intermittency Indices Along the Riser and Downer. (H. Zhang, Huang, and Zhu 2001)

It can be concluded that the microflow structure is more uniform in the downer than in the riser.

2.9 Development of Gas-Solid Flow Structure

The length of flow development (LOD) is the length that is needed for both the radial solids holdup profile and radial particle velocity to become fully developed (Zhang, Huang and Zhu, 2001; Wang, 2013). This is referred to as LOD_v for particle velocity, and LOD_f for solids flux.

Figure 2.13a shows the effects of G_s and U_g on the LOD, in terms of particle velocity in the core and wall regions; Figure 2.13b reports the effects of the operating conditions on LOD to determine the solid mass flux.

a)

b)
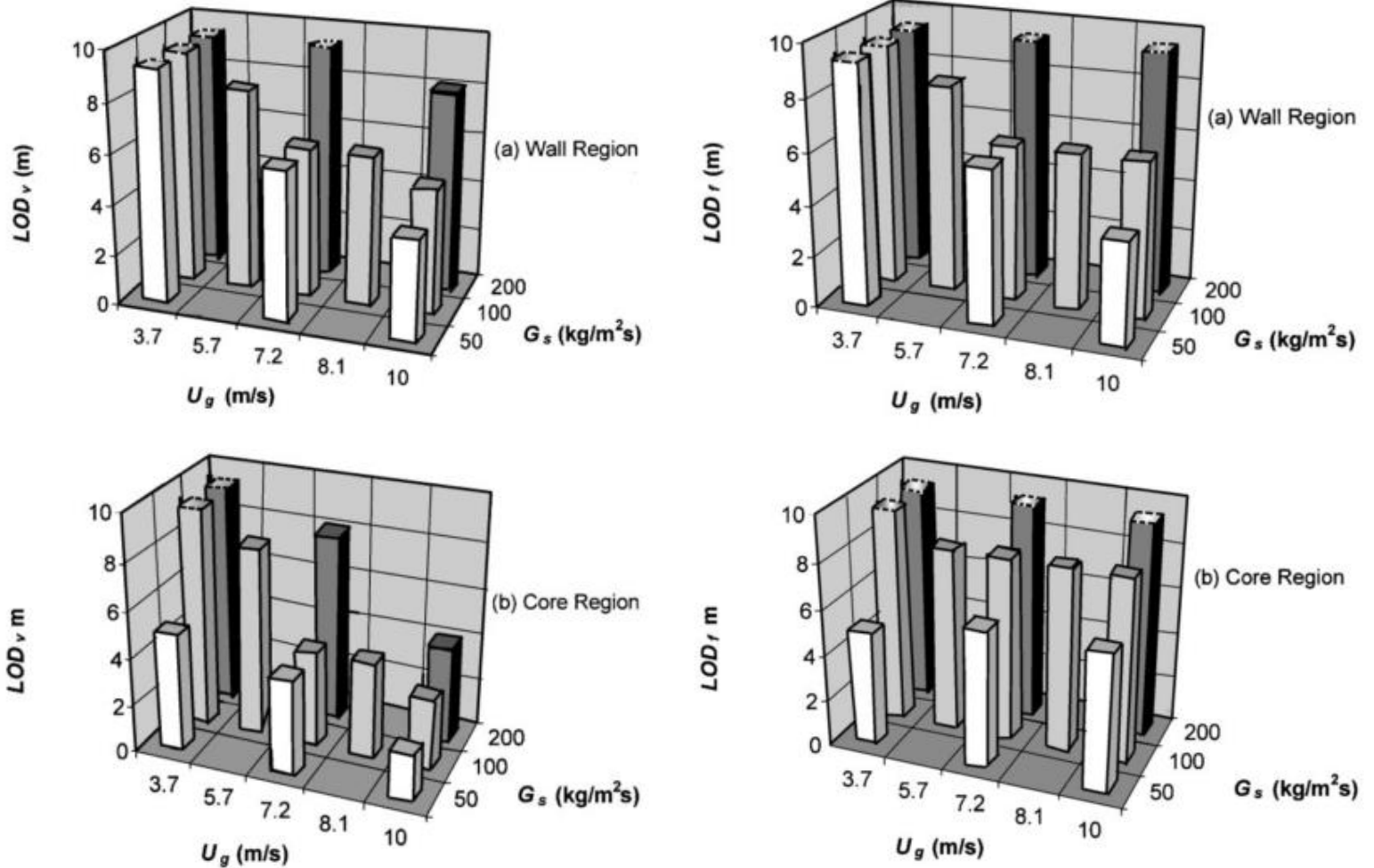
Figure 2.13. Effects of Solids Circulation Rate and Gas Velocity on the Length of Flow Development to Determine a) particle velocity, and b) solids flux. (H. Zhang and Zhu 2000)

One can observe that increasing the G_s at a constant U_g always extends the LOD_v for both the core and wall regions while increasing the U_g with a fixed G_s always shortens LOD_v for both regions. The influence of the operating conditions on the LOD_f is, however, quite different. In the core, increasing the G_s and/or the U_g slows down the radial flow development. In the near-wall region, increasing the G_s extends the flow development, while increasing the U_g shortens it.

27

For catalytic or non-catalytic reactions, smaller LODs are favourable, since the axial solid dispersion is less uniform in the development zone and may be detrimental for the overall reactor performance. In fact, larger LODs may lead to over-conversion and the formation of undesired products in reactors. Therefore, a downer is preferred due to the smaller length of development, and this to better control both the overall conversion and desired product selectivity.

2.10 High Density Gas-Solids Flow Studies

The studies reported above focused on low to medium flow density in downers, where the average solids holdup is below 5 %. In a special effort to achieve high solids holdup, Liu et al. (W. Liu et al. 2001) designed a downer feeder consisting of a 0.66 m tall funnel with a 250 mm diameter, in order to pre-accelerate the particles and feed them at terminal velocity. Using this apparatus, an average solids holdup of 0.07 – 0.09 was achieved with a solids circulation rate over 400 kg/m^2 s.

Wang and Zhu (C. Wang, Li, and Zhu 2015) employed a riser-downer system where solids fluxes of 700 kg/m^2 s were registered and average solids holdup higher than 0.06 were achieved. One could notice in this respect that, the development of solids holdup can be enhanced by increasing U_g and/or decreasing G_s, as shown in Figure 2.14. It can also be seen that particle acceleration (and therefore flow development) begins from the center and then extends to the near-wall region.
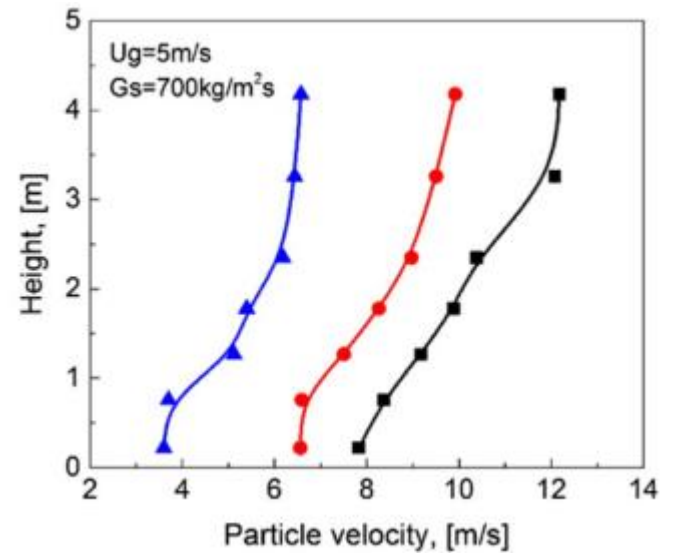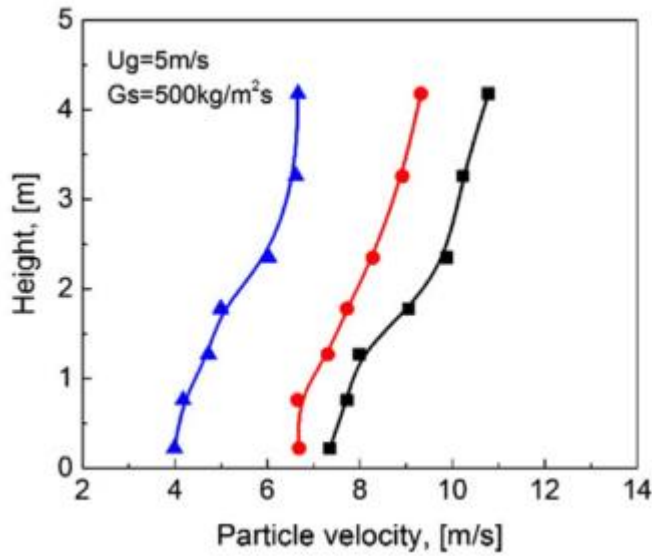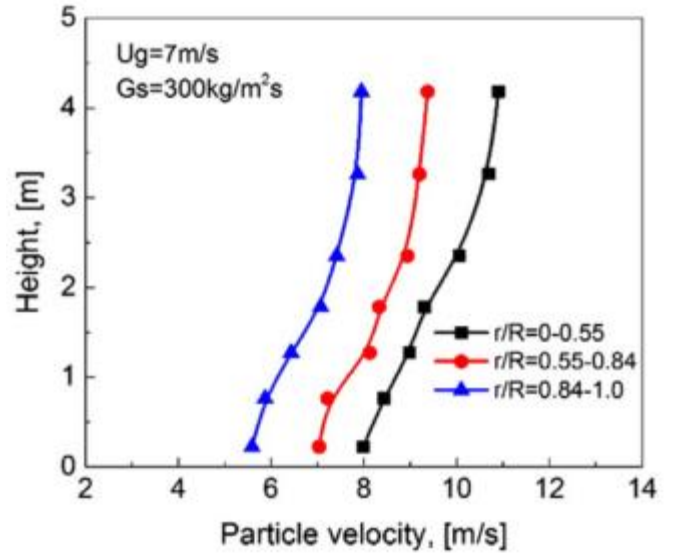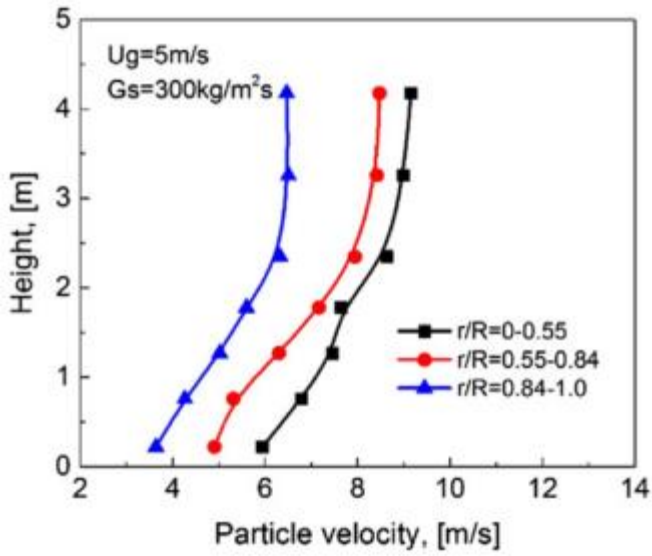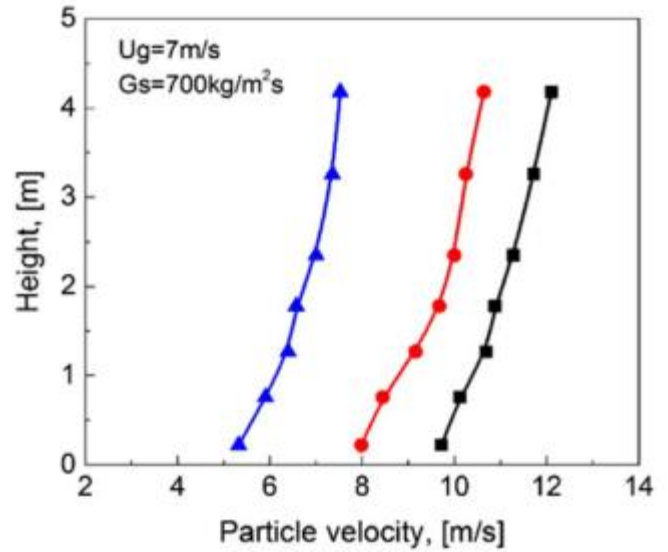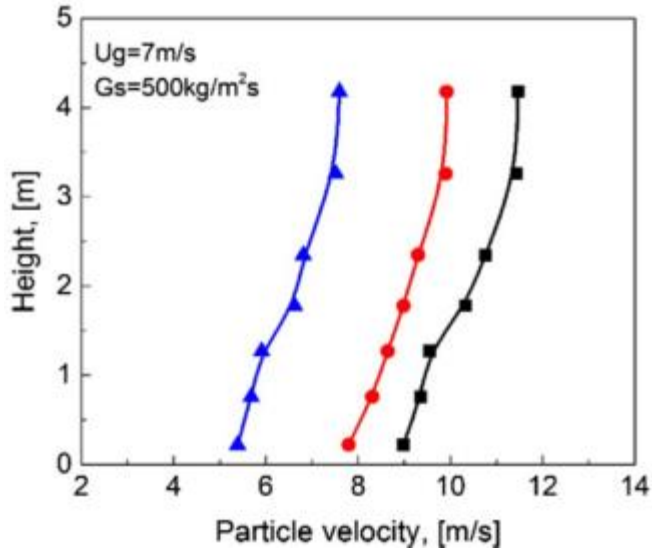
Figure 2.14. Flow Development of Local Particle Velocity Along the Downer (C. Wang, Li, and Zhu 2015).

The solids circulation rate plays a key role in the distribution of solids holdup. Solids holdup increases with the increase of G_s. The effects of G_s are more significant at low superficial gas velocities than that at high U_g. The flow development of solids holdups along the downer is reported in Figure 2.15.
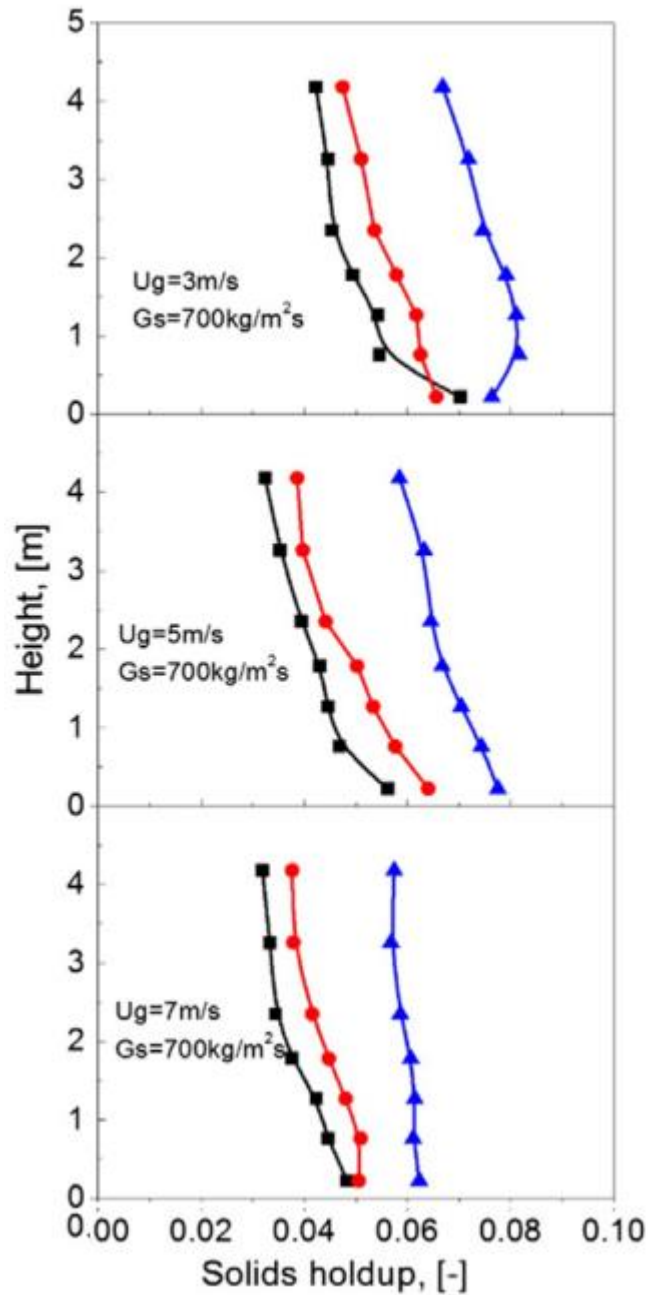
Figure 2.15. Flow Development of Local Solids Holdup along the Downer. (C. Wang, Li, and Zhu 2015)

One can also notice in Figure 2.15 that the highest solids holdup conditions are achieved at low superficial gas velocities and high solids circulation rates. The solids holdups are higher at the near-wall and the entrance of the downer regions.

2.11 Slip Phenomenon and Solid Aggregation

The slip velocity is defined as the difference between particle and gas velocities, and it determines the gas-solid heat and mass transfer.

Krol et al. (Krol, Pekediz, and de Lasa 2000) proposed a model where particles agglomerate, on the basis of a number of leading particles being followed by a number of trailing particles. In this model, a trailing particle experiences a wake attraction created by the motion of a leading particle and thus becomes a string of two particles. This process may repeat itself and form larger strings.

The clusters behave differently in riser and downer reactors. In the riser, as the cluster gets bigger (and heavier), its velocity decreases because of the gravity. It becomes more difficult to collapse, contributing to the solids backmixing, which is characteristic in the riser. The clusters in the downer move along with gravity. As they get bigger, their velocity increases, making them easier to break.

The continuous formation and collapse of clusters means that there is a more stable flow in the downer compared to the riser (Wang, Chengxiu; Li, Chunyi; Barghi, Shahzad; Zhu 2015). According to the study performed by Tuzla et al. (Tuzla, K. Sharma 1998) the life of particle clusters may be in the order of 0.1 to 10 ms, meaning that this process may occur several times inside the downer.

Lu et al. (Lu et al. 2005) used high-speed photography to study downers. The presence of clusters with a flock and stick shape is clear, as depicted in Figure 2.16.
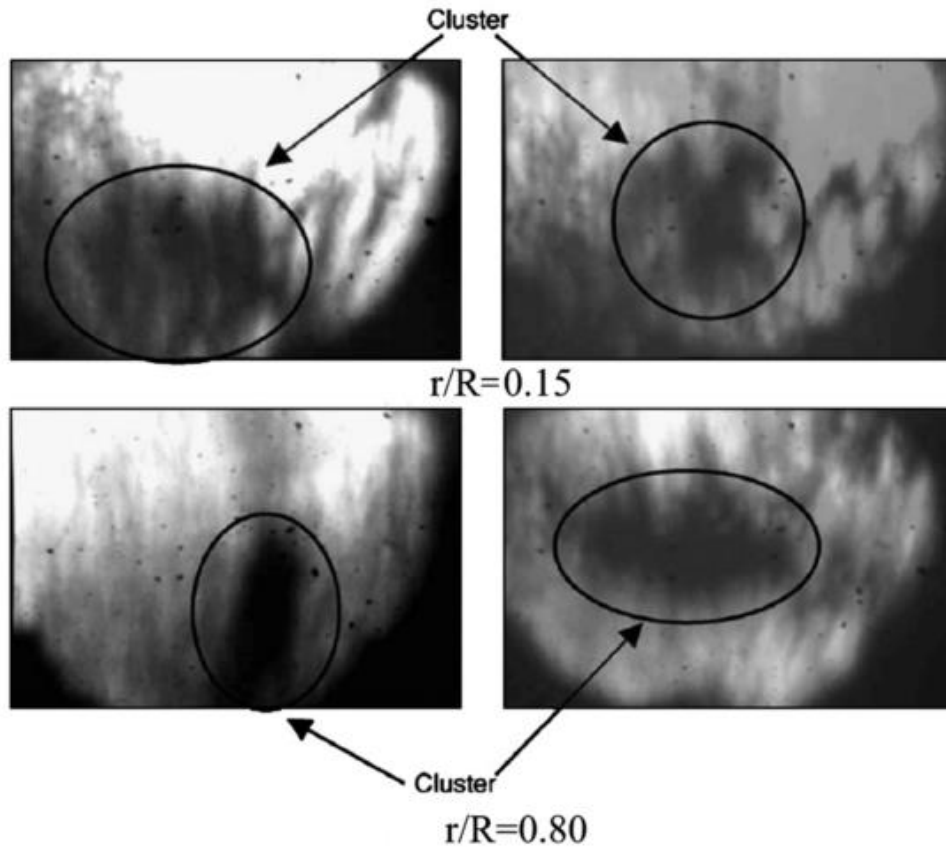
Figure 2.16. Solids Clusters in a Downer. (Lu et al. 2005)

The effect of operating conditions on the slip velocity is reported in Figure 2.17. In the study, the authors used FCC particles with a particle diameter of 59 μm and particle density of 1550 kg/m^3.
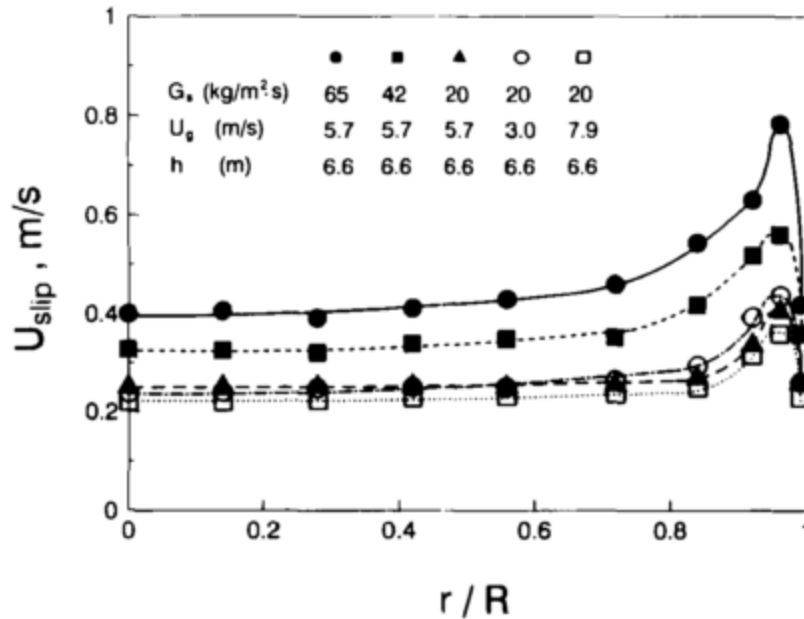
Figure 2.17. Radial Slip Velocity Distribution - Effect of Solids Circulation Rate and Gas Velocity (J. X. Zhu et al. 1995)

2.12 Residence Time Distribution (RTD) and Two-Phase Mixing

The solids holdup and particle velocity studies help one to understand the hydrodynamics inside downflow reactors. Axial and radial profiles in the downer have shown more uniformity compared to those in the riser, as reported above. However, more information regarding the residence time and the mixing of solids is necessary to improve our understanding of these units.

Jin and Chen (Yong Jin and Chen 1994) used a phosphor tracer technique to measure the solids RTD in the downer axis. Figure 2.18 shows typical RTD curves for different radial positions.
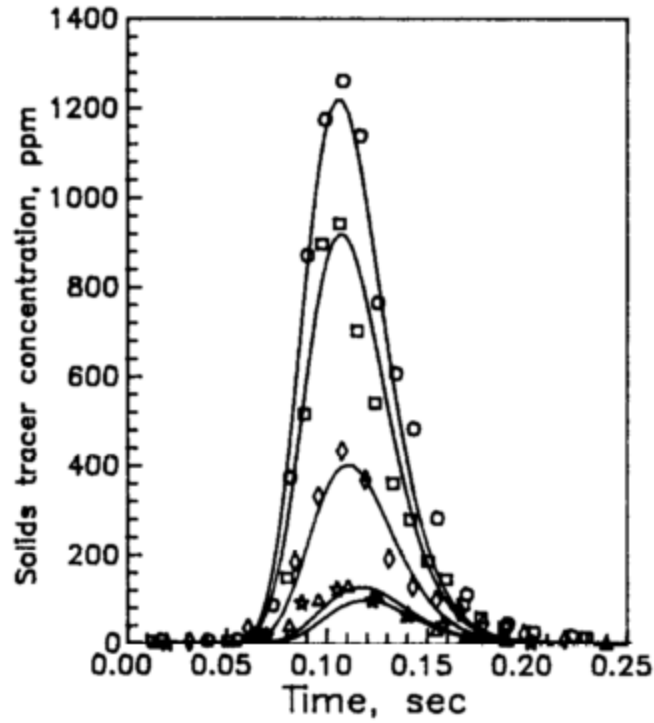
Figure 2.18. RTD Curves (x=0.4 m, Ug = 3.5 m/s, Gs = 33 kg/m2 s): (○) r/R = 0.0; (□) r/R = 2/7; (◊) r/R=4/7; (Δ) r/R=6/7; (*) r/R=1 (Yong Jin and Chen 1994)

Gas and solids flow patterns differ greatly in risers and downers, as shown by hydrodynamics studies and as discussed in Section 2.4.3. These differences also affect the mixing behavior in the units. Using the phosphorus tracer techniques, Wei and Zhu (Wei and Zhu 1996) report the RTD curves for risers and downers, depicted in Figure 2.19.
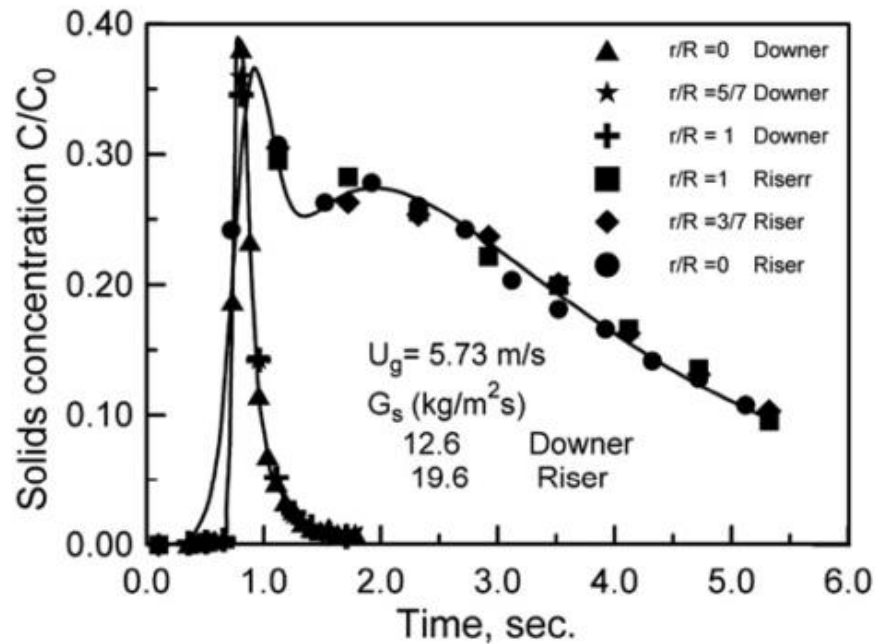
Figure 2.19. Solids RTD in the Downer and Riser (Wei and Zhu 1996).

When comparing the RTD curves for the two reactor types, one can note that the narrower solids concentration distribution of the downer means that there is close to plug-flow behaviour in this type of unit. On the other hand, one can observe that the long tail of particles in the riser is due to the backmixing of particles, resulting from the flow against gravity.

A complete understanding of the two-phase flow mixing also requires knowledge of the gas phase. Wei et al. (Wei, Jin, Yu, and Liu 1995) applied a steady-state tracer technique to measure hydrogen. The results show limited backmixing in the axial direction. However, there is lateral mixing which is comparable to that in the riser. Radial profiles of tracer concentrations measured at different heights are depicted in Figure 2.20.
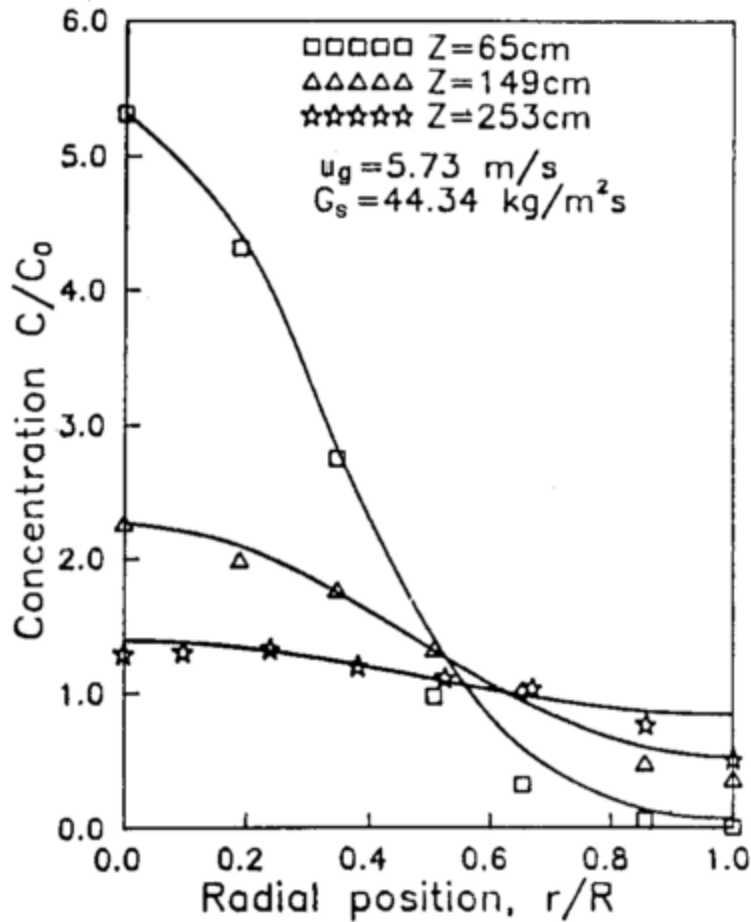
Figure 2.20. Tracer Concentration as Function of Radial Position (Wei, Jin, Yu, and Liu 1995)

The Peclet number is defined according to the following equation:

$$Pe_a = \frac{U_g L}{D_a} \qquad (2-3)$$

Where U_g is the superficial gas velocity, L is the length between the injection and measuring points, and D_a is the mass diffusion coefficient in the axial direction.

Wei and Zhu (Wei and Zhu 1996) also reported the axial and radial values of the Peclet number (Pe). Their results are depicted in Figure 2.21, with similar Pe values reported for the radial direction compared with those of the riser. However, the axial Pe number in the downer is two orders of magnitude greater than that in the riser. This is attributed to the fact that the large radial gas dispersion allows the gas to mix well in this direction. Furthermore, the small observed axial dispersion is characteristic of the downer´s close

to plug-flow behaviour. All this contributes to determining that the downflow CFB are good reactors. Furthermore, it highlights the advantages of using a downer versus utilizing a riser.
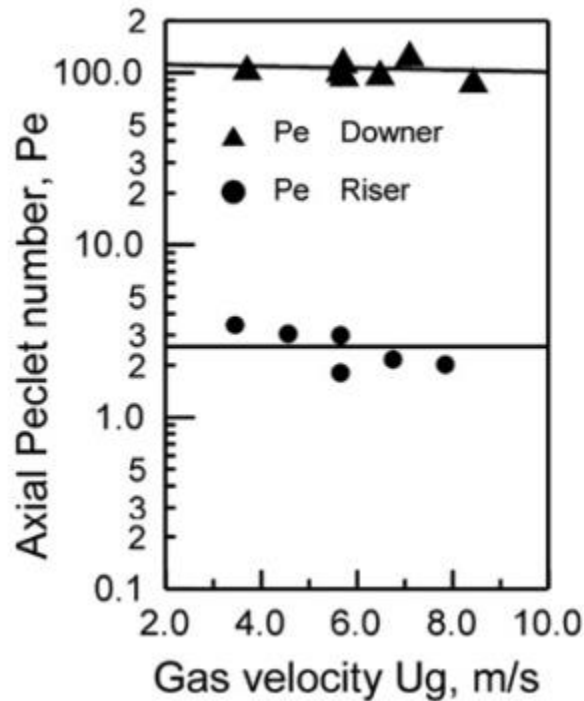
Figure 2.21. Calculated Peclet Number in Riser and Downer. (Wei and Zhu 1996)

2.13 Heat Transfer

Heat transfer between a gas-solid flow and heat transfer surfaces in a CFB is comprised mainly of three components: particle convection, gas convection, and radiation (Ma and Zhu 1999). Normally, particle convection is the primary heat transfer mechanism. Gas convection may become important at high velocities and low solids holdups. Ma and Zhu (Ma and Zhu 1999) determined local heat transfer coefficients in a downflow reactor by using a miniature cylindrical copper probe.

The experimental data indicates that the average heat transfer coefficient decreases along the downer. This agrees with the decrease in solids holdups. Figure 2.22 shows the axial distribution of the heat transfer coefficient and the suspension density.

a)

b)
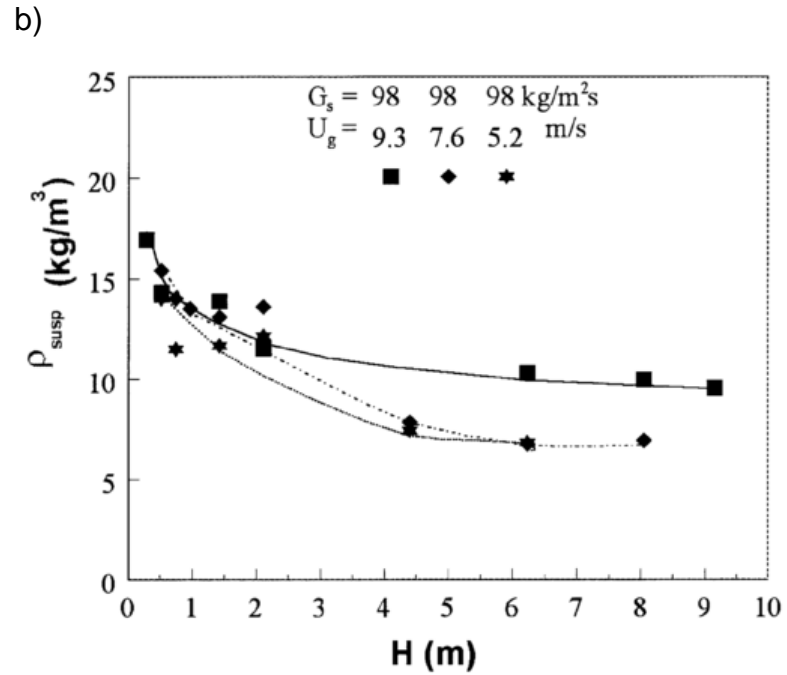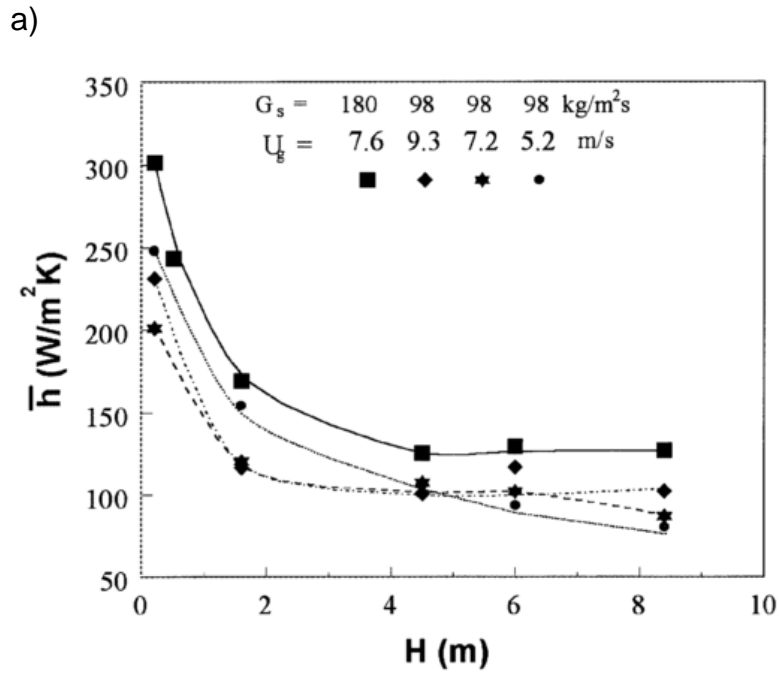
Figure 2.22. Axial Distribution of: a) Average heat transfer coefficient; b) Average suspension density (Ma and Zhu 1999)

One can observe in Figure 2.8 that the radial profiles of solids holdup show a high concentration of solids at the near-wall region. This corresponds with the observed radial variation of the heat transfer coefficient, as depicted in Figure 2.23.
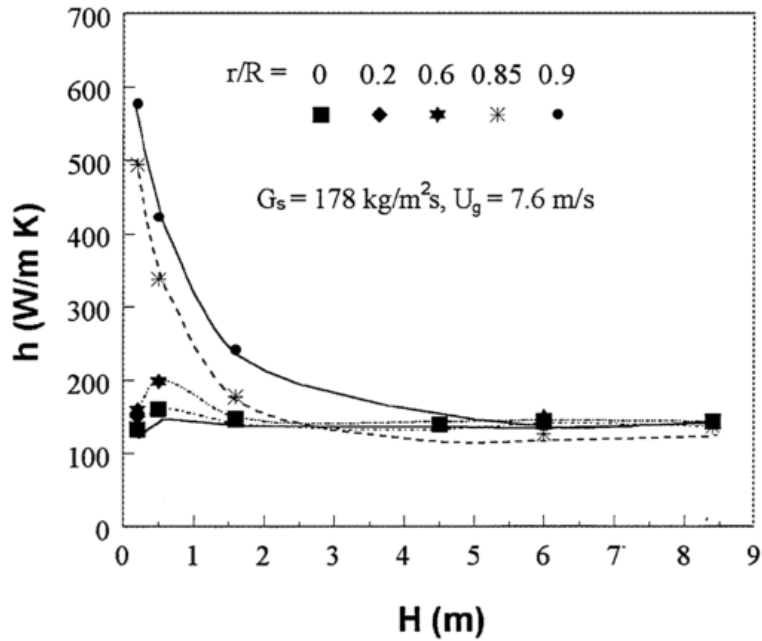
Figure 2.23. Axial Distribution of Heat Transfer Coefficient at Different Radial Positions (Ma and Zhu 1999)

Thus, it can be concluded from Figure 2.22 and 2.23 that heat transfer in downers is closely related to the local solid concentration (apparent particle density).

2.14 CFD Studies of Downflow Reactors

The gas-solid flow in downers has been modelled and described through several methods and at different scales. As mentioned above, there are two main types of multiphase models: Eulerian-Eulerian, where both phases are described as a continuum; and Eulerian-Lagrangian, where the fluid phase is a continuum and the solids are modeled as a discrete phase, following their trajectory.

Regarding the Eulerian-Eulerian, or Two-Fluid model, several studies have been performed to describe the downer behaviour. Cheng (Yi Cheng et al. 1999) implemented a particulate turbulence term into the conventional kinetic theory framework. By comparing the conventional kinetic theory and their modified model, the authors found that the conventional kinetic theory overpredicts the particle densification while the turbulent model for both phases has a better agreement with experimental data. These authors also performed a scale-up analysis and observed very uniform radial profiles for

the small downer diameter, without the typical densification near the wall reported by the FLOTU group.

In addition to this, Jian and Ocone (Jian and Ocone 2003) developed a two-fluid model of a downer reactor with a modified solid stress tensor, introducing a counter-diffusive term accounting for all inter-particle cohesive forces and this to predict particle movement.

Furthermore, Li and Lin (S. Li, Lin, and Yao 2004) used the energy-minimization and multi-scale (EMMS) drag model, which describes the interactions between gas and particles at three scales: micro-scale of individual particles; meso-scale of clusters; and macro-scale. These authors found that in this case, the cluster size was small, only a few times greater than the particle size, compared to several hundred times the particle size in riser reactors.

Additionally, Ropelato (Ropelato, Meier, and Cremasco 2005) used an Eulerian-Eulerian approach in downers, considering two interpolation schemes: a first-order Upwind, and a second-order Higher Upwind. The results showed a small difference in the particle volume fraction between the two schemes, in the order of 10^{-3}, which was considered negligible.

Chalermsinsuwan (Chalermsinsuwan et al. 2012) performed a parametric study within the Eulerian-Eulerian framework, evaluating the impact of a) the specularity coefficient, b) the restitution coefficient between particle and wall, c) the restitution coefficient between particles, d) the interphase exchange function, e) the inlet granular temperature, and f) inlet configuration. The authors concluded that the interphase exchange model, the inlet granular temperature, and the inlet configuration have the most significant effect on the downer system.

Regarding the Eulerian-Lagrangian modelling, Zhang (M. H. Zhang et al. 2008) proposed a model with the solid phase being treated as a discrete phase, as described by a conventional DEM. This model was developed to compare the cluster behavior in a riser and a downer. The results showed that clusters at the near to wall region behave very differently. While in the riser the clusters have a downward velocity opposite to the main flow, the clusters in the downer are all downward, in the same direction as the main flow.

As well, the simulations show a shorter duration lifespan for the clusters in the downer unit (0.05 s).

As mentioned previously, Lanza (Lanza and de Lasa 2016, 2017) implemented a hybrid numerical cluster model in MP-PIC simulations using the CPFD Barracuda VR commercial software. In this work, the researchers used an experimentally determined cluster size distribution as the particle size distribution in the simulations. Clusters were considered to be non-spherical using the Ganser and Haider-Levenspiel drag correlations for the interphase momentum exchange. The results were in good agreement with the experimental data collected in the fully developed flow sections of two downers of different cross-sectional areas.

Furthermore, the MP-PIC model has been implemented in downer reactors with catalytic reactions. Rostom and de Lasa (Rostom and de Lasa 2019) designed a downer reactor for the catalytic dehydrogenation of propane to obtain propylene. Additionally, Ahmed and de Lasa (Ahmed and de Lasa 2020) proposed one such reactor for the chemical looping combustion process.

2.15 Potential Applications

The downer reactor features make it especially suitable for a fast reaction where the intermediates are the desired products. As such, its application has been explored in fields such as high temperature catalytic cracking, pyrolysis of coal and biomass, plasma reactors for acetylene production, among others.

2.15.1 *Fluid Catalytic Cracking (FCC)*

Fluid Catalytic Cracking (FCC) was the first application of fine powder fluidization. Nowadays, it is still the major application of fluidization at a large scale. FCC is a profitable and useful process in refineries. It takes the heavy petroleum fractions and yields more useful products such as gasoline, diesel, and light cycle oil, which account for 75-80% of the total refinery products (Babich and Moulijn 2003). FCC gasoline represents 30-40% of the gasoline pool (W.-C. Cheng et al. 1998). Out of the more than 600 refineries around the world, around 300 of them use this technology. Almost all the FCC units in the world are risers, but due to their shortcomings, many researchers and oil refining companies

began researching downflow configurations, obtaining patents for downers during the 1980s and 1990s.

Talman et al. (Talman, Geier, and Reh 1999) developed a downer reactor for this process. Although they reached oil conversions of up to 70% with residence times of 60-400 ms, the reported high conversions were only achieved when the solids could be transformed into a questionably homogeneous dispersed two-phase flow.

Abul-Hamayel (Abul-Hamayel 2004) developed the High Severity Fluid Catalytic Cracking (HS-FCC) process based on the downer reactor at a pilot-plant scale. Features of the HS-FCC process include 550°C reaction temperature, short contact times, and 13-35 high catalyst/oil ratios. The pilot plant study was performed with both risers and downers and the results are shown in Figure 2.24.

a)

b)
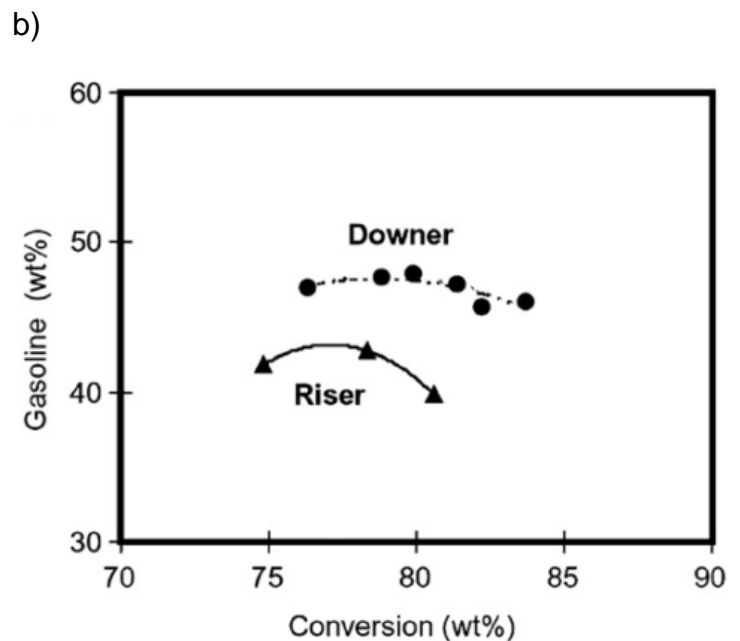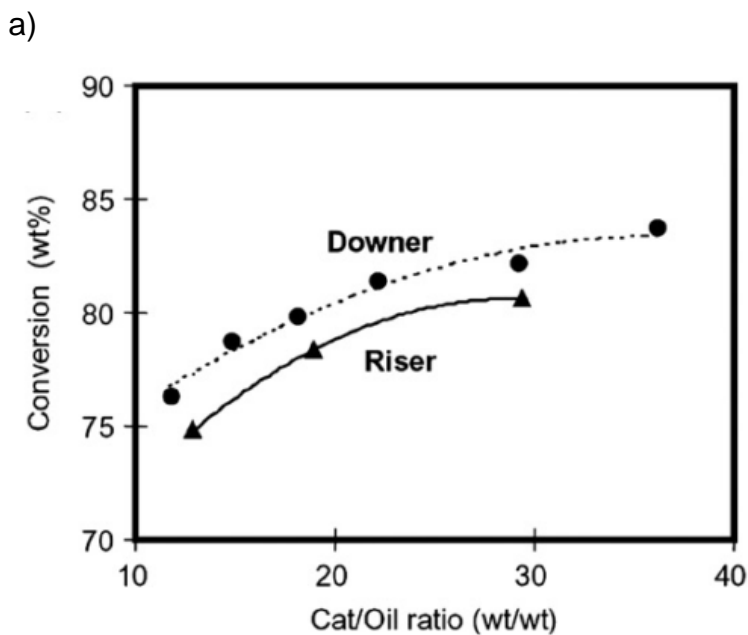
c)

d)
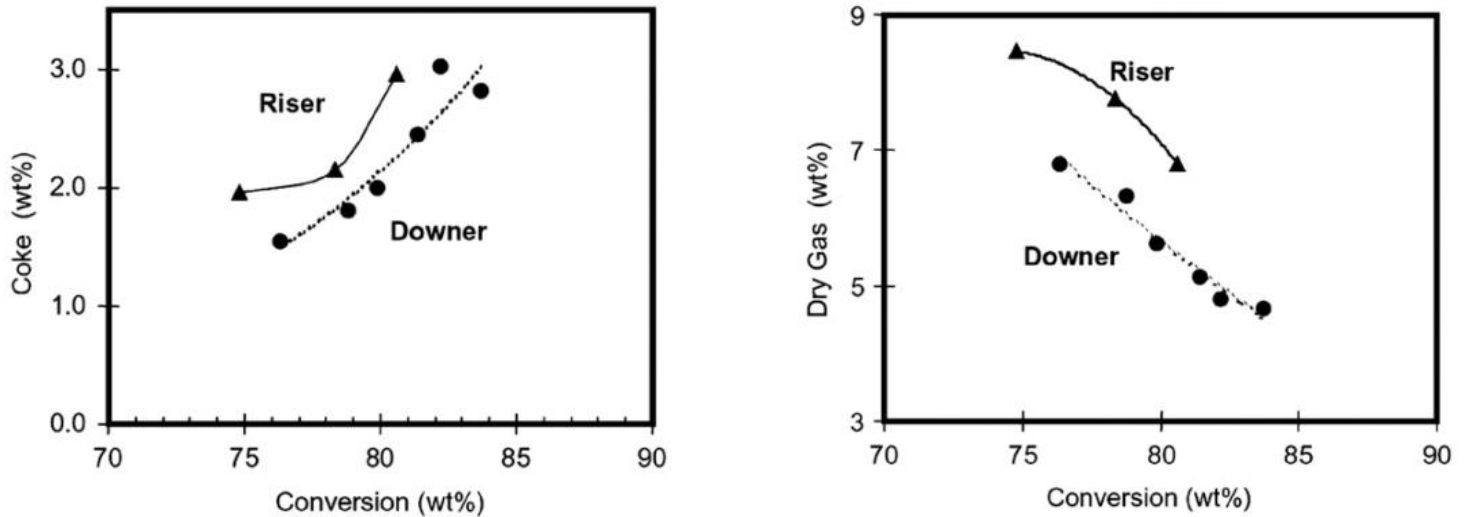
Figure 2.24. Comparison of Riser and Downer Reactors used for FCC. a) Oil conversion versus cat/oil ratio, b) Gasoline yield, c) Coke yield, d) Dry gas yield (Abul-Hamayel 2004)

A circulating fluidized bed was built in the Ji´nan refinery (SINOPEC). It was the first industrial demonstration of a downer reactor in a refinery (Yi Cheng et al. 2008). This unit consisted of a riser coupled to a downer (RtoD) reactor and was tested for deep catalytic cracking (DCC), and residue FCC feedstock (RFCC). The results for DCC included a 1.06 wt% increase in gasoline yield, an 8.38 wt% increase in diesel oil, and a 0.75 wt% increase in propylene yield. Regarding the RFCC, the yields of LPG and propylene increased by 11.45 and 5.06 wt%, respectively.

While these results are encouraging for downer unit applications to FCC, they are questionable and require additional checking and verifications needed given the following:

o Diffusional processes in FCC catalyst establish intrinsic limits for the transport of VGO species having a 330-350 kg/kgmole molecular weight. Chemical species have to diffuse in the microchannels of the Y zeolite crystallites (0.4-1 micron size), dispersed in 60-micron fluidizable particles, to reach active sites. Thus, suggested reaction times, below 1 second, are questionable for an FCC process dominated by catalytic reactions and taking full benefit from the high selectivity of Y-zeolites for gasoline formation.

o High C/Os surpassing the values of 7, may lead to a catalytic reaction strongly dominated by the stronger Y zeolite acid sites, either internal or external, which

44

invariably leads given stoichiometric constraints to excessive amounts of light gases and coke.

2.15.2 *Pyrolysis and Gasification*

Biomass is considered a viable alternative to fossil fuels, for the production of energy and useful chemicals. Biomass is widely available and represents a source of liquid, solid, and gaseous fuels (Bridgwater and Peacocke 2000). Biomass can be treated by biological and thermal methods. The latter are summarized in Figure 2.25.
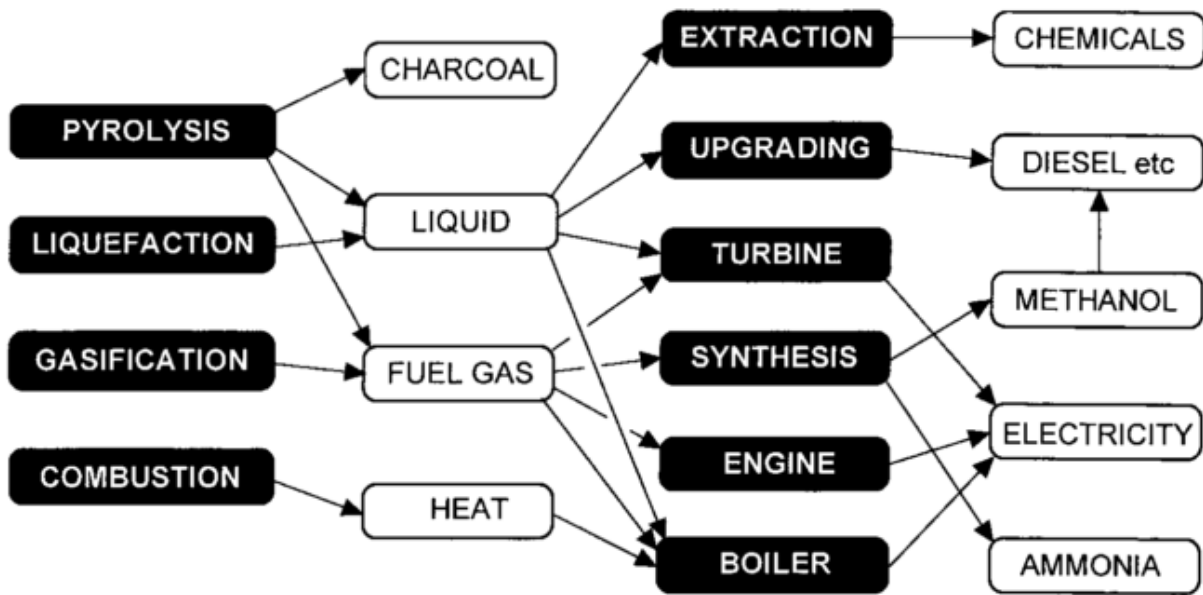
Figure 2.25. Thermochemical Biomass Processes and Products. (Bridgwater and Peacocke 2000)

Berg et al. (Berg, Briens, and Bergougnou 1989) developed the Ultra-Rapid Fluidized Reactor for biomass pyrolysis, which consisted of a mixer, a downer, and a separator.

Another possible application for the downer is coal gasification. Kim et al. (Kim, Lee, and Kim 2001) developed a gasifier, where the heat is supplied from combustion in a riser and the gasification reaction is done in the downer section.

The downer, operated at its highest severity operation (1500 K – 3000 K), can be used in the pyrolysis of coal for acetylene production (Y. Cheng et al. 2008).

2.15.3 Coal Topping

The implementation of a downer combustor for coal topping has been proposed (J. Wang et al. 2005). This is an integrated multiproduct process, with the objective being to obtain a high yield of light liquid fractions and gaseous products by flash pyrolysis.

2.15.4 Carbon Nanotube Synthesis

A coupled downer-turbulent fluidized bed was used in the synthesis of single-walled carbon nanotubes, showing a higher selectivity and yield, given that there was a more controlled residence time distribution in the reactor (Yun et al. 2013).

2.16 Conclusions

- o Fluidization processes play a major role in the world's economy, providing useful materials and necessary fuels to drive progress. Fluid catalytic cracking of vacuum gas oil is an important part of today's refinery.

- o However, with increasing regulations and the general concern about greenhouse gas emissions and the generation of cleaner fuels, it is vital to pursue enhancements to the process.

- o The downer reactor, which functions oppositely to the riser, with gas and solids flowing in the same direction as gravity, can lead to better utilization of catalytic resources and more flexible operating conditions.

- o Downer reactors applications to FCC are still very limited. Units operating with high 15-35 C/O ratios were claimed to provide high VGO conversions. However, these units may potentially lead to an excessive amount of coke, and as a result, fundamentally based hydrodynamic models and kinetics are still required. This is needed before further downer application to FCC processes is engaged.

- o Hydrodynamics downer studies have shown that the downer has three major sections based on particle velocity: first and second acceleration sections, and a fully developed flow section. In this regard, most reported research work focuses on the fully developed flow section where the particles reach terminal velocity.

- o Downer studies have established important features in downer reactors, such as limited cluster formation, distinctive hydrodynamic regions, and uniform flow

profiles. These characteristics allow potentially for higher conversion of reactants, an operation without hotspots, and increased selectivity towards desired products.

- o Downer mixing studies have shown a small axial solids dispersion, with the overall two-phase flow pattern approximating the plug-flow behaviour. Thus, the downer offers much more uniform radial profiles, as well as a narrower residence time distribution, reducing the yield of unwanted products.

3   Research objectives

The main objective of the present PhD Dissertation is to develop knowledge regarding the downer reactor operation and simulation, with particular emphasis in the downer entry section. With this goal in mind, the specific objectives of the present study were as follows:

a) To measure the individual particle cluster sizes, velocities, and particle volume fractions in a cold-flow model unit, using the advanced non-intrusive CREC-GS-Optiprobes fiber optic devices. This should be done at various axial positions, including the downer feeding section and the downer stabilization section.

b) To study the mixing efficiency in the selected gas-solid downer feeder, comprised of a cyclone and a ring gas injector, as well as to assess the impact of the entry region on the flow development and stabilization in the downer.

c) To develop a numerical hybrid fluid dynamic model based on the MP-PIC method, accounting for the cluster size and geometry obtained experimentally.

d) To validate the numerical model with the experimental data and to determine the appropriate drag correlation closure equations.

e) To numerically simulate the vacuum gas oil fluid catalytic cracking demonstration reactor unit, by implementing a 5-lump kinetic model originally developed in a CREC Riser Simulator (Al-Sabawi, Atias, and de Lasa 2006).

f) To assess the mixing effectiveness of the selected feeder type in a scaled-up downer reactor using as a basis, the numerically calculated axial and radial temperature at various C/Os, feeding temperatures, and contact times, of industrial interest.

It is expected that in all these respects, the present study which combines experimental and numerical methods will provide insights on both particle cluster acceleration and stabilization downer sections. It is anticipated that this PhD Dissertation, with its original findings in the entry downer section, will be of significant value for the design and operation of large-scale fluidized catalytic cracking downer units.

4 Experimental Setup and Methodology

4.1 Catalyst particles

The catalyst particles used in the 0.051m ID Plexiglas unit experiments were those of an FCC catalyst with a mean diameter of 84.4 μm, and a standard deviation of 33.6 μm. The particle apparent density was 1722 kg/m^3. The cumulative particle size distribution is reported in Figure 4.1.
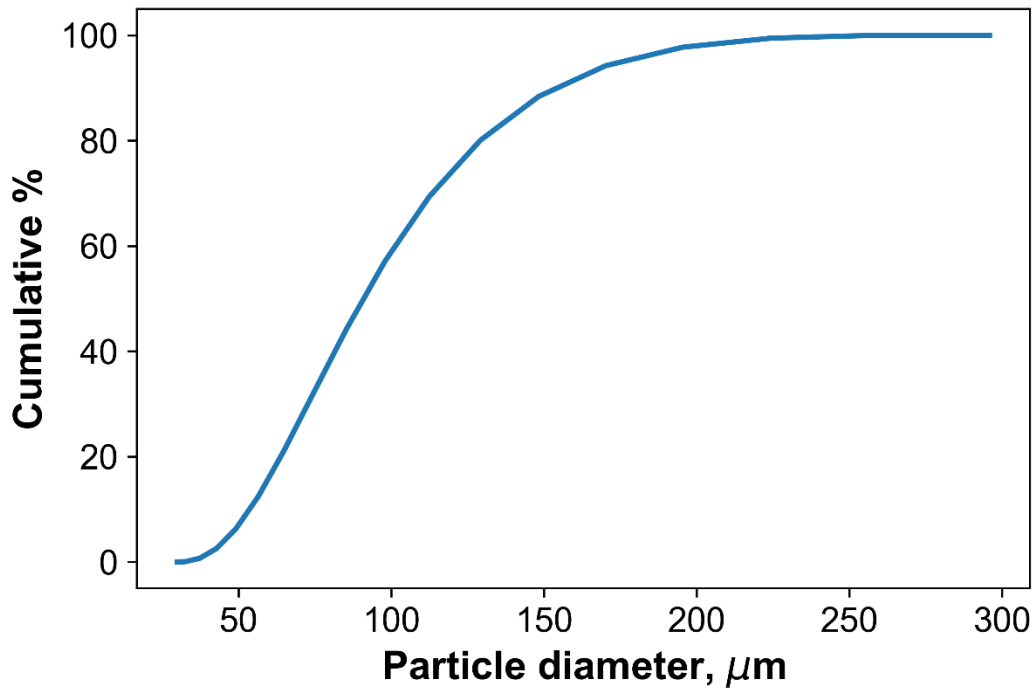
Figure 4.1. Experimental Particle Size Distribution.

The electrostatic charges produced from the gas-solid flow can affect the agglomeration of particles and lead to inaccurate results. To avoid this, a set volume of 0.01 m^3 of ammonium hydroxide (28-30% ammonia concentration) is added per every cubic meter of FCC catalyst in the system.

4.2 Downer experimental setup

All the experiments reported here were carried out in a cold-flow model system, depicted in Figure 4.2.
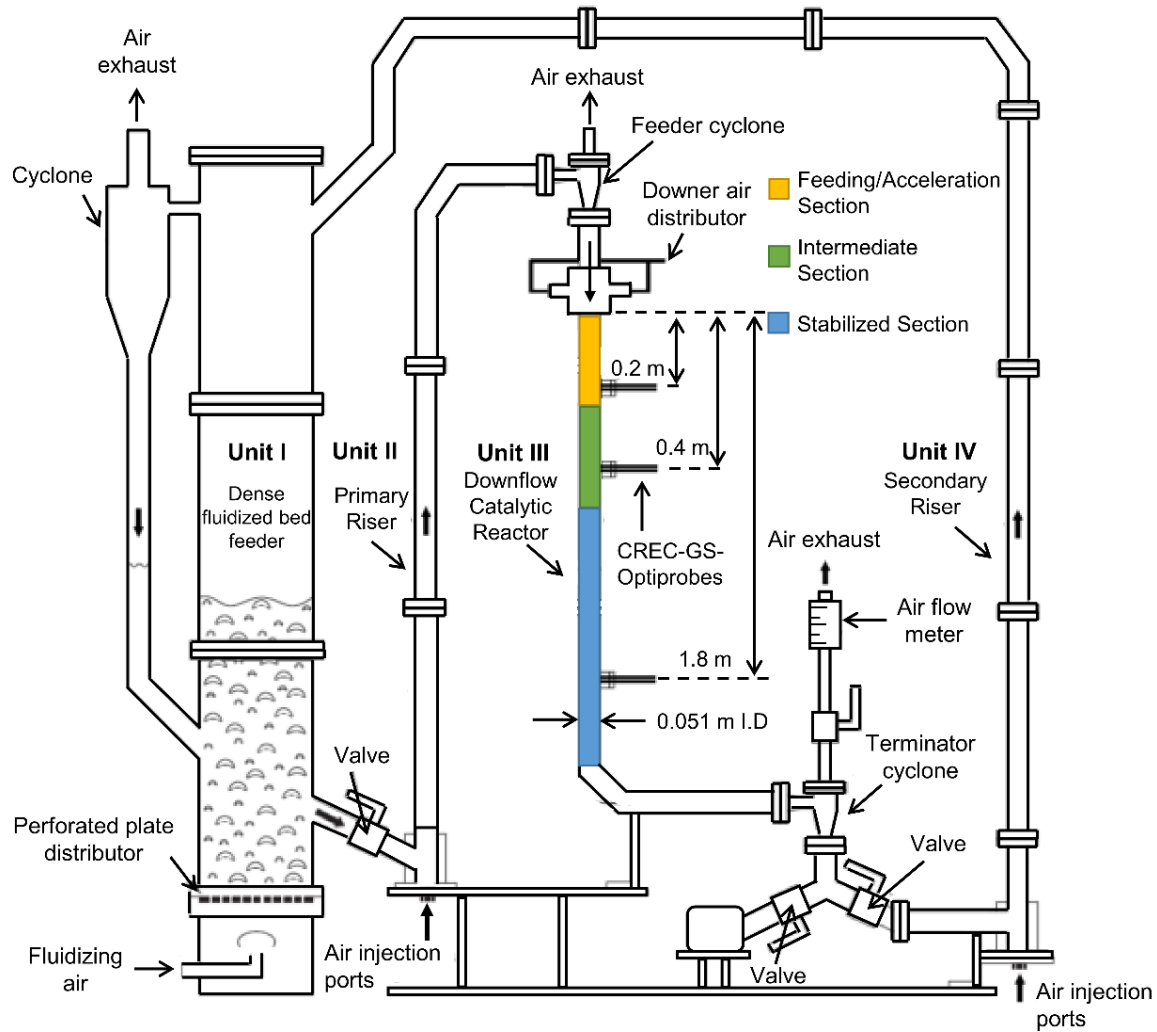
Figure 4.2. Schematic Description of the Experimental System Employed for the Experimental Studies. Note: Unit I: Dense Phase Fluidized Bed Feeder. Unit II: Primary Riser Unit, Unit III: Downflow Reactor Unit, Unit IV: Secondary Riser Unit. (Medina-Pedraza and de Lasa 2020)

Figure 4.2 describes the experimental system which is comprised of the following: a) Unit I: a *Dense Phase Fluidized Bed Feeder*, b) Unit II: a *Primary Riser*, c) Unit III: a *Downer Unit* and d) Unit IV: a *Secondary Riser*. First, the catalyst is fluidized in Unit I, then it is fed through a ball valve to the Primary Riser of Unit II. The Primary Riser unit ends in a cyclone, where gas and catalyst particles are separated. Next, the particles enter the downer unit or Unit III. At the downer feeding section, descending particles encounter eight air jets. These eight air jets are fed via nozzles equally spaced around the column perimeter. Each nozzle has a diameter of 2 mm and is angled at 45º downwards. Below the downer feeding section, the 0.051 m ID downer column extends 2 m downwards. At

the exit of the downer, the catalyst particles are directed to an output cyclone that redirects the particles to the solid mass flux measuring device or to a Secondary Riser Unit, designated as Unit IV. Unit IV allows the catalyst particles to be returned to the Dense Fluidized Bed Feeder (Unit I), providing continuous circulation of solids in the experimental setup.

Figure 4.3 shows additional details of the downer unit, specifically of the feeding section and the eight air jets distributed circumferentially, pointing down the downer's longitudinal axis with an inclination of 45⁰.
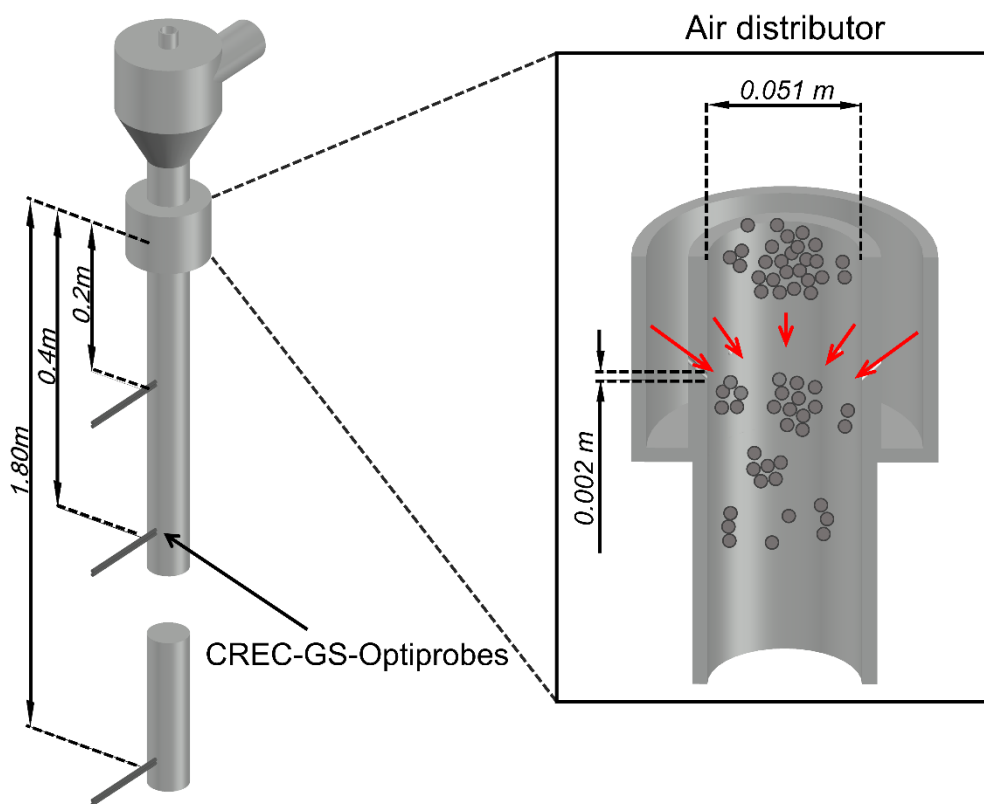
Figure 4.3. Diagram of the Cold-Flow Model Unit Providing Details of the Downer Feeding Section.

To study the evolution of the clusters in the downer unit, three axial positions were selected for the experimental study: 0.20, 0.40, and 1.80 m, measured from the bottom of the air distributor. This allowed for the detection of accelerating clusters at Z = 0.20 m. Z = 0.40 m represented an intermediate position and Z = 1.80 m was located in the fully developed flow section, where the clusters have stabilized.

The superficial gas velocity used in the experiments was 1.0 and 1.6 m/s, and this in order to evaluate the changes at these conditions. In the same manner, the solids mass flux was set at values close to 30 and 50 kg/m^{2}s. Finally, pressure measurements were effected at the same axial positions as the cluster data acquisition was performed.

4.3   Data Acquisition (DAQ) System

The CREC-GS-Optiprobes are modified fiber optic sensors that allow for the detection of individual clusters, thanks to its small high irradiation intensity focal region located away from the tip of the probe. The calibration of the device and focal region characteristics were obtained with a rotating disk, that uses the same FCC particles as in the experiments, as documented in Nova (Nova, Krol, and de Lasa 2004). Additionally, a camera laser beam profiler was used. More details about the apparatus are reported in Islam (Ashraful Islam, Krol, and de Lasa 2011). These results showed that the focal region has a transversal length of 118 µm, with a standard deviation of 33.6 µm. Furthermore, it is located 5 mm away from the tip of the probe. Details of the CREC-GS-Optiprobe and its focal region are shown in Figure 4.4.
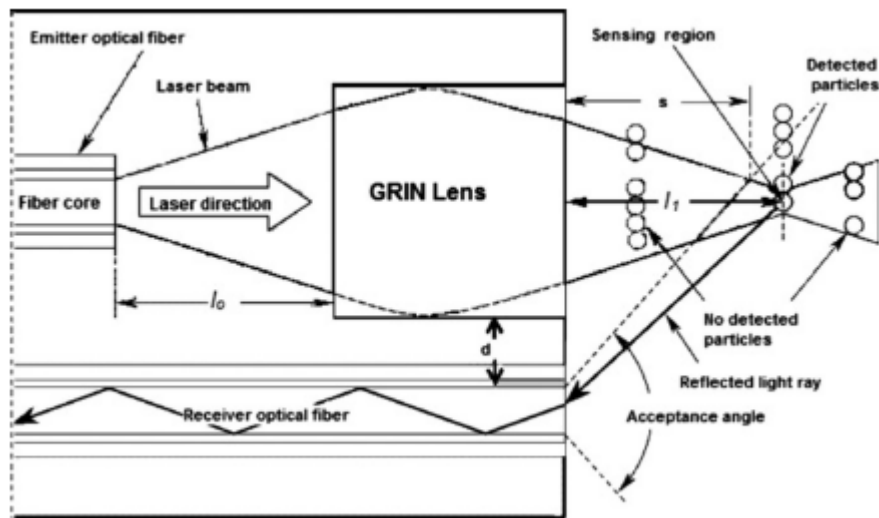
Figure 4.4. Features of CREC-GS-Optiprobes: l_o, object distance; l_1 image distance; d spacing between the GRIN lens and the receiver fiber core; s distance defining the visible domain boundary of the receiver fiber. (Ashraful Islam, Krol, and de Lasa 2011)

The DAQ setup is comprised of the following: a) An 820 nm laser diode light source focused on the emitting fiber; b) an emitting fiber with a GRIN lens which redirects the

light rays creating the highly irradiated focal region; c) a receiver fiber which collects the rays reflected by the particles; d) a photomultiplier converting photons from the receiver fiber into a voltage signal; e) a BNC block transferring the output voltage signal to the DAQ card placed in a computer running LabVIEW software. The DAQ card is a National Instruments PCI-6143. The LabVIEW software records the voltage signals and provides various data acquisition analyses. Figure 4.5 describes the complete DAQ system employed in the experiments.
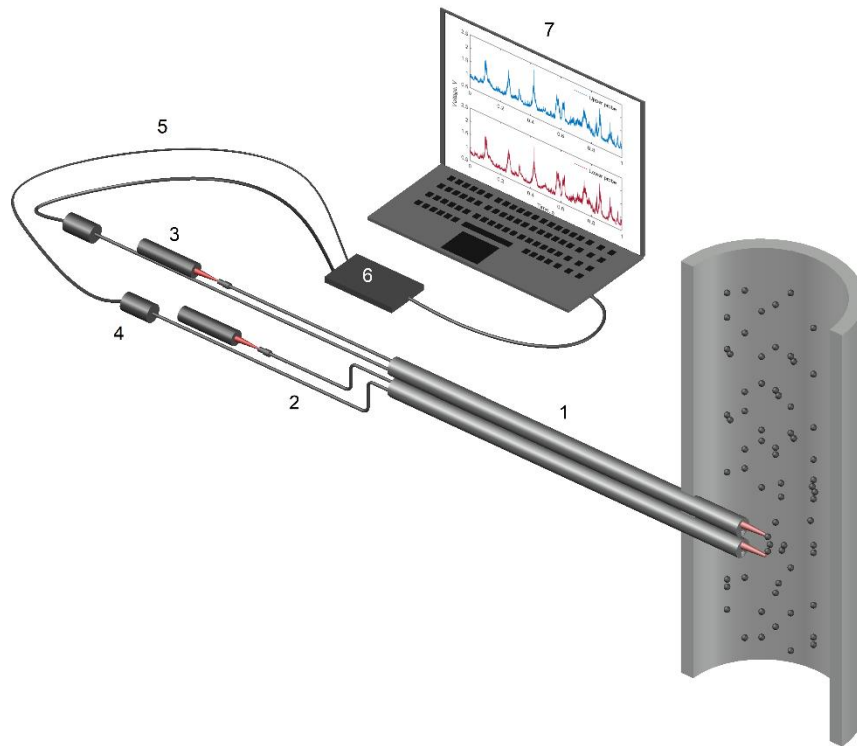
Figure 4.5. Fiber-Optic Measurement System: (1) CREC-GS-Optiprobes with an Emitting Fiber and a GRIN Lens, (2) Fiber Optic Cable, (3) Laser Diode, (4) Photodetector, (5) BNC Cable, (6) BNC Connector Block, (7) Computer with LabVIEW Software Pack (Medina-Pedraza and de Lasa 2020)

4.4   Methodology

4.4.1   Cluster Properties Calculation

The CREC-GS-Optiprobes allow one to obtain the particle volume fraction, the particle cluster size, and the particle cluster velocity, simultaneously. The sensor is comprised of two axially aligned fiber optic probes. When a particle cluster passes through the focal region of the CREC-GS-Optiprobe, a voltage signal is generated and recorded by the DAQ system. Additionally, a second signal is generated when the particle is detected by

the bottom probe. Thus, the particle velocity can be established by the time lag between the two signals, which is determined by a cross-correlation function. Since this is a discrete function, an error is produced when few sampling points are obtained. To minimize this error, the sensor records 100,000 data points per second, to fully capture the particle movement in the downer unit, while reducing the error related to the cross-correlation function. (Herbert et al. 1994)

Measurements were taken at 21 positions across the downer diameter as follows: two measurements at 0.005 m from the wall on each side; 19 measurements every 0.002 m of the remaining distance. These measurements were repeated five times at each position, with a sampling time of 1 second each. Typical signals obtained are portrayed in Figure 4.6.
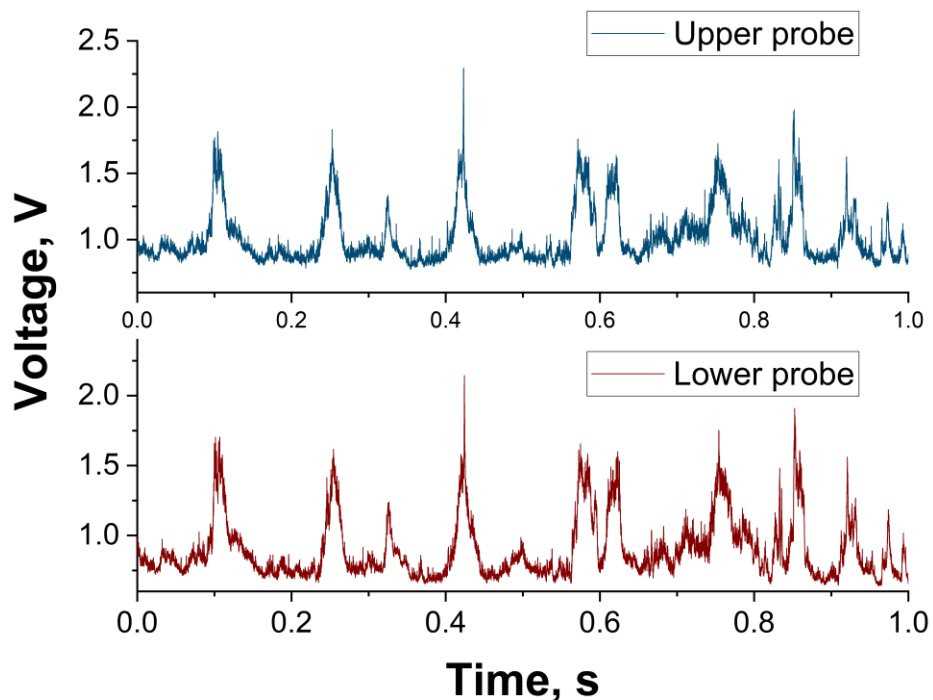
Figure 4.6. Typical CREC-GS-Optiprobe Voltage Signals as Detected by the Upper and Lower Probes. (Medina-Pedraza and de Lasa 2020)

Electrical signal noise and secondary reflection noise were eliminated by using a baseline signal. The baseline signal position is calculated with Equation 4-1 as follows:

$$V = \bar{v} + n\sigma_v \qquad\qquad (4-1)$$

where V represents the baseline signal in volts, $\bar{v}$ is the average of the recorded voltage signals, n is a baseline factor calculated for every solid circulation condition studied, and σ_v is the voltage signal standard deviation.

Furthermore, when a cluster passes in front of the optical fiber, a peak is registered, with a time width of t_i. The particle holdup is calculated using Equation 4-2, as shown below, by adding the width of all peaks detected by the CREC-GS-Optiprobes and dividing this result by the sampling time.

$$\varepsilon_s = \frac{\sum t_i}{t} \tag{4-2}$$

The cluster velocity is calculated with the distance between the probes, which is 5 mm, and the time lag between signals, which is designated as τ. It is then calculated with the cross-correlation function shown in Equation 4-3.

$$C_{xy}(\tau) = \lim_{t \to \infty} \frac{1}{t} \int_0^t x(t) \cdot y(t + \tau) dt \tag{4-3}$$

$$u_c = \frac{d}{\tau} \tag{4-4}$$

It should be noted that only peaks with a cross-correlation coefficient greater than 0.4 were considered as valid for cluster detection, as recommended by Lanza (Lanza, Islam, and de Lasa 2017).

Furthermore, the cluster size, N, reported as the number of particles with an average diameter forming the cluster, is calculated using Equation 4-5:

$$N = \frac{t_i u_c - h + d_p}{d_p} \tag{4-5}$$

with h being the sensing region transversal length of the CREC-GS-Optiprobes as reported by Islam et al. (Ashraful Islam, Krol, and de Lasa 2011).

4.4.2 Cluster Velocity and Drag Coefficient Calculation

In the fully developed flow section of the downer, clusters have a 'strand' type shape, i. e. a series of particles arranged in a vertical row, as shown in Figure 4.7. This is believed

to be the more stable fluid dynamic form of the particle cluster (Krol, Pekediz, and de Lasa 2000).
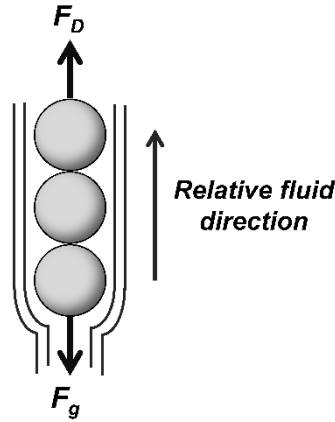
Figure 4.7. Forces Acting on a Particle Cluster.

Regarding particle clusters arranged in a strand or train of particles, their volume can be calculated according to Equation 4-6:

$$V_c = \frac{1}{6}\pi d_p^3 N \qquad (4-6)$$

As well, the cluster cross-sectional area normal to the flow can be defined with Equation 4-7 as follows:

$$A_{c,max} = \frac{\pi}{4} d_{p,max}^2 \qquad (4-7)$$

Furthermore, the particle cluster Reynolds number, which is the ratio of the inertial and viscous forces, can be calculated with Equation 4-8 as follows:

$$Re_p = \frac{2r_{eq}\rho_f u_{slip}}{\mu_f} \qquad (4-8)$$

where u_{slip} is the cluster slip velocity, and r_{eq} is the radius of the equivalent sphere having the same volume as the cluster, as given by Equation 4-9:

$$r_{eq} = \sqrt[3]{\frac{3V_c}{4\pi}} \qquad (4-9)$$

Cluster velocity and its change with time-on-stream can be described via a balance of forces as described in Equation 4-10:

$$m_p \frac{du_p}{dt} = F_g - F_D \qquad (4-10)$$

With F_g being the gravity force, calculated as a buoyancy effect, as follows:

$$F_g = V_c(\rho_s - \rho_f)g \qquad (4-11)$$

Furthermore, the drag force, F_D can be calculated according to Equation 4-12a as follows:

$$F_D = \frac{1}{2}\rho_f A_{c,max} C_D u_{slip}^2 \qquad (4-12a)$$

With C_D representing the drag coefficient.

At steady-state, which is the equivalent of particle clusters having a zero acceleration, or du_p/dt equaling zero, the gravity and drag forces are equal, and can be replaced by Equations 4-11 and 4-12a as follows:

$$\frac{1}{2}\rho_f A_{c,max} C_D u_{slip}^2 = V_c(\rho_s - \rho_f)g \qquad (4-12b)$$

Thus, Equation 4-12b can be rearranged to obtain an expression for the slip velocity in terms of the fluid density, particle density, cluster volume, cluster cross-sectional area as follows:

$$u_{slip} = \sqrt{\frac{2V_c(\rho_s - \rho_f)g}{\rho_f A_{c,max} C_D}} \qquad (4-13)$$

A similar expression for particles with an average diameter can be obtained by replacing the cluster volume and particle cross-sectional area in Equation 4-13, which results in Equation 4-14. In this manner, the particle cluster velocity can be expressed as a function of the axial cluster length, which is the parameter detected by the CREC-GS-Optiprobes. Thus, assuming a cluster "train of particles" the following is obtained:

$$u_{slip} = \sqrt{\frac{4Nd_p(\rho_s - \rho_f)g}{3\rho_f C_D}} \qquad (4-14)$$

Equation 4-14 is strictly applicable to the stabilized flow downer section, for particles with an average diameter. It includes a drag coefficient for particle clusters, modeled as non-spherical particles, as described in Figure 4.7.

The clusters considered in this study are modelled as non-spherical particles. The drag coefficient can be estimated through several available literature correlations (Loth 2008). Haider and Levenspiel (Haider and Levenspiel 1989) proposed a correlation for non-spherical particle motion with the sphericity being a key parameter. The standard sphericity is the ratio of the surface area of the volume equivalent sphere to the surface area of the non-spherical particle studied. Later, Ganser (Ganser 1993) similarly proposed a drag function but implementing two shape factors: the Stoke's factor based on low Reynolds regimes; and Newton's factor, accounting for behavior at higher Reynolds. In this respect, Lanza et al. (Lanza, Islam, and de Lasa 2012; Lanza and de Lasa 2016) concluded that the Ganser correlation, based on Chhabra (Chhabra, Agarwal, and Sinha 1999) provides the best C_D correlation for a "train of particles" as shown in Figure 4.7 in the fully developed flow section. The Ganser drag function is defined by Equation 4-15.

$$C_D = \frac{24}{Re_p K_1 K_2}\left(1 + 0.1118\left(Re_p K_1 K_2\right)^{0.6567}\right) + \frac{0.4305}{1 + \dfrac{3305}{Re_p K_1 K_2}} \qquad (4-15)$$

$$K_1 = \frac{3}{1 + 2\phi^{-0.5}} \;\; ; \;\; K_2 = 10^{1.8148(-log\phi)^{0.5743}} \qquad (4-16)$$

More recently, it was reported by Bagheri (Bagheri and Bonadonna 2016) that for the motion of non-spherical particles, the Hölzer-Sommerfeld drag model (Hölzer and Sommerfeld 2008) yields a lower error than the Ganser correlation. Thus, in the present study, further consideration is given to a Hölzer-Sommerfeld drag correlation, which considers three shape parameters based on a cluster equivalent sphere of equal volume: a) Standard sphericity: the ratio of the surface area of the equivalent sphere to that of the cluster; b) Cross-wise sphericity: the ratio between the cross-sectional area of the equivalent sphere and the cluster projected area, normal to the flow; and c) Lengthwise sphericity: the ratio of the cross-sectional area of the equivalent sphere over the

difference between half of the cluster surface area and the cluster projected area parallel to the flow. Thus, the drag coefficient is calculated according to Equation 17 as follows:

$$C_D = \frac{8}{Re_p\sqrt{\phi_\parallel}} + \frac{16}{Re_p\sqrt{\phi}} + \frac{3}{\sqrt{Re_p}\phi^{0.75}} + 0.42 * 10^{0.4(-log\phi)^{0.2}} \left(\frac{1}{\phi_\perp}\right) \qquad (4-17)$$

One should note that the Hölzer-Sommerfeld correlation can offer a more accurate description of the particle clusters, using the three shape parameters described in the previous paragraph and represented in Equations 4-18, 4-19, and 4-20:

$$\phi_\parallel = \frac{4r_{eq}^2}{Nd_p^2} \qquad (4-18)$$

$$\phi = \frac{4r_{eq}^2}{Nd_p^2} \qquad (4-19)$$

$$\phi_\perp = \frac{4r_{eq}^2}{d_p^2} \qquad (4-20)$$

4.4.3 Random Cluster Selection

Since the particles in the system have a size distribution ranging from a diameter of 30 µm to 220 µm, particles in clusters can be arranged differently. In order to study this, a MATLAB script was developed to randomly select a set of particles that match the average measured axial cluster length, within a 2% error. This methodology was previously used to some extent by Lanza et al.(Lanza and de Lasa 2016) This cluster configuration is depicted in Figure 4.8.
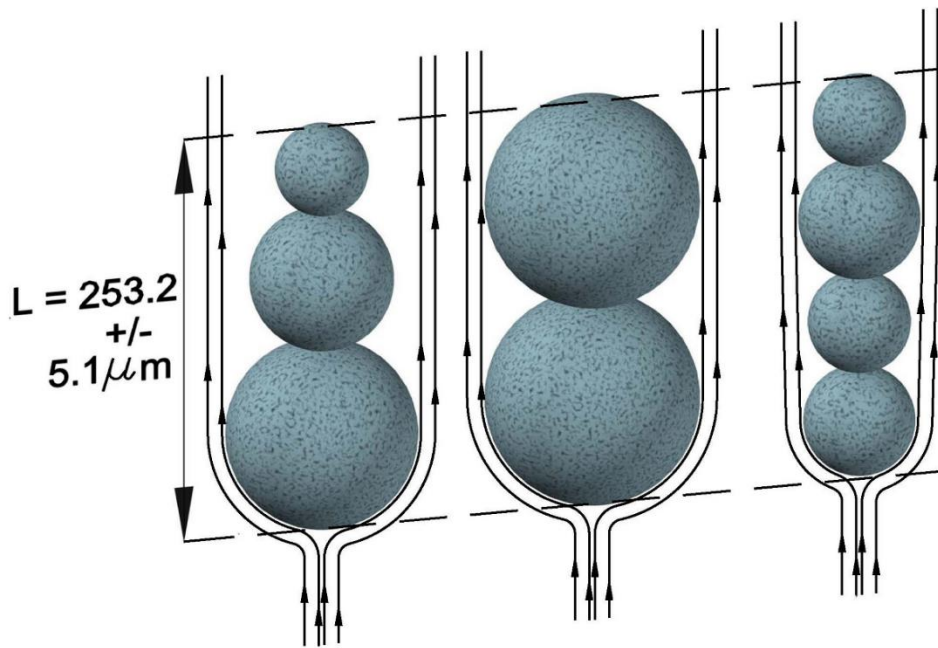
Figure 4.8. Cluster Shape with Random Particle Selection.

In this manner, one can form different particle clusters having the same length, with, however, different configurations, with this being critical for slip velocity calculations. One can notice as well that clusters are formed with a different number of particles. Figure 4.9 shows histograms for the number of particles, cluster volume, cluster cross-sectional area, and sphericity, in 1000 clusters with a length of 253.2 µm.

a)

b)

c)

d)
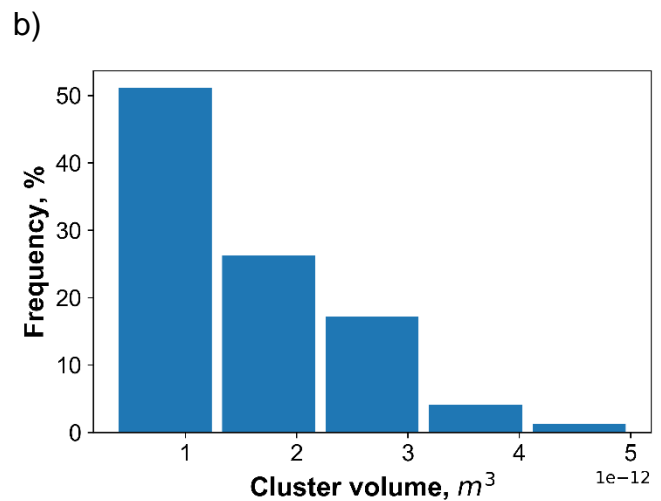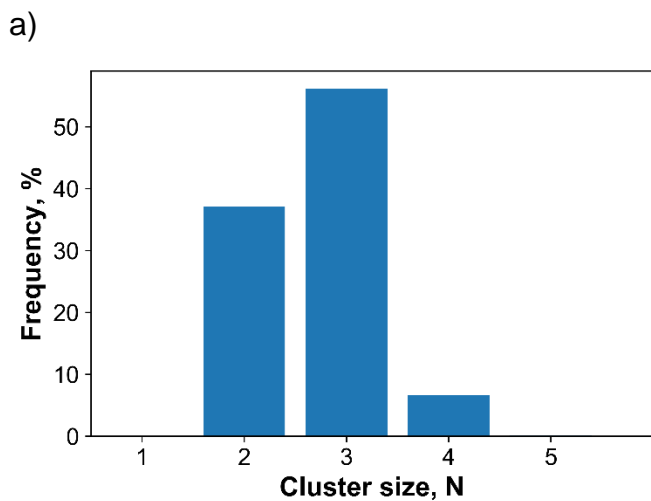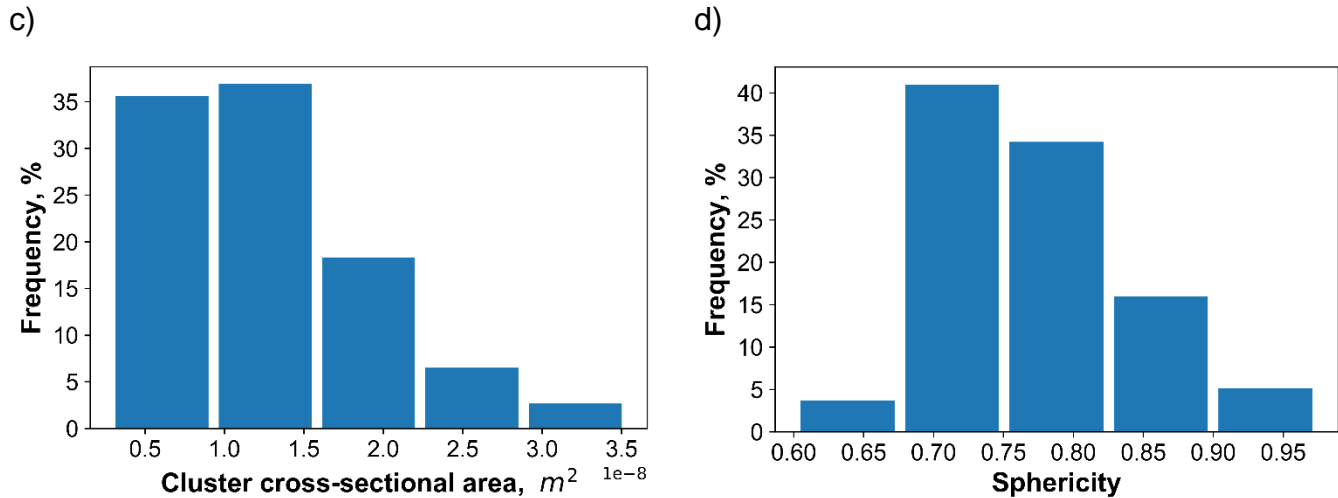
Figure 4.9. Frequency distribution of a) number of particles in a cluster; b) cluster volume; c) cluster cross-sectional area normal to the flow; d) sphericity.

As illustrated in Figure 4.9, the clusters, even if they have the same length can be constituted by a different number of particles, and more importantly, have different volumes, cross-sectional areas, and sphericities, which are key parameters that determine their velocity.

4.5   Conclusions

a) The CREC-GS-Optiprobes were successfully used to characterize and monitor the particle cluster dynamics and individual cluster characteristics in the feeding section of a downer unit.

b) Clusters with the same axial length were randomly generated from the original particle size distribution. These clusters have a distribution of the number of particles, volume, cross-sectional area, and sphericity, these are key parameters for the calculation of cluster velocity.

5   Cluster acceleration and stabilization results and discussion

5.1   Cluster Size Distribution in the Downer

Cluster size distributions were studied in the downer of the present study, at the flow conditions reported in Table 5.1. For the four flow conditions studied, experiments at three different axial positions were effected. Each combination of superficial gas velocity, solids flux, and axial position was repeated at least five times. Every one of the performed runs included a minimum of 50,000 detected peaks over a recording time of 5 seconds. Following data processing for every run, at least 1000 of them were selected as acceptable peaks using baseline analysis and cross-correlation, with calculations being developed as reported in Section 4.4. Calculations provided particle cluster size, particle volume fraction, and particle cluster velocity.

Table 5.1. Operating Conditions

Condition	U_{sg} (m/s)	G_s (kg/m^2 s)
Z = 0.2 m from air distributor		
1	1.0	31.4
2	1.0	50.3
3	1.6	31.2
4	1.6	53.3
Z = 0.4 m from air distributor		
5	1.0	30.2
6	1.0	50.8
7	1.6	30.5
8	1.6	50.5
Z = 1.8 m from air distributor		
9	1.0	31.1
10	1.0	49.6
11	1.6	31.0
12	1.6	52.0

In particular, and to study the flow development in the downer, systematic comparisons between radial averaged cluster sizes and radial averaged cluster velocities in the feeding section, in the intermediate section height, and the fully developed section were effected. Analyzing these data, using average values was considered adequate, given the radial cluster size standard deviations at various downer levels were limited to 6%.

Figure 5.1 reports the particle cluster size distribution at Z = 0.20 m, Z = 0.40 m, and Z = 1.80 m, with a 1.0 m/s superficial gas velocity and a 31.0 kg/m^2 s solid flux.
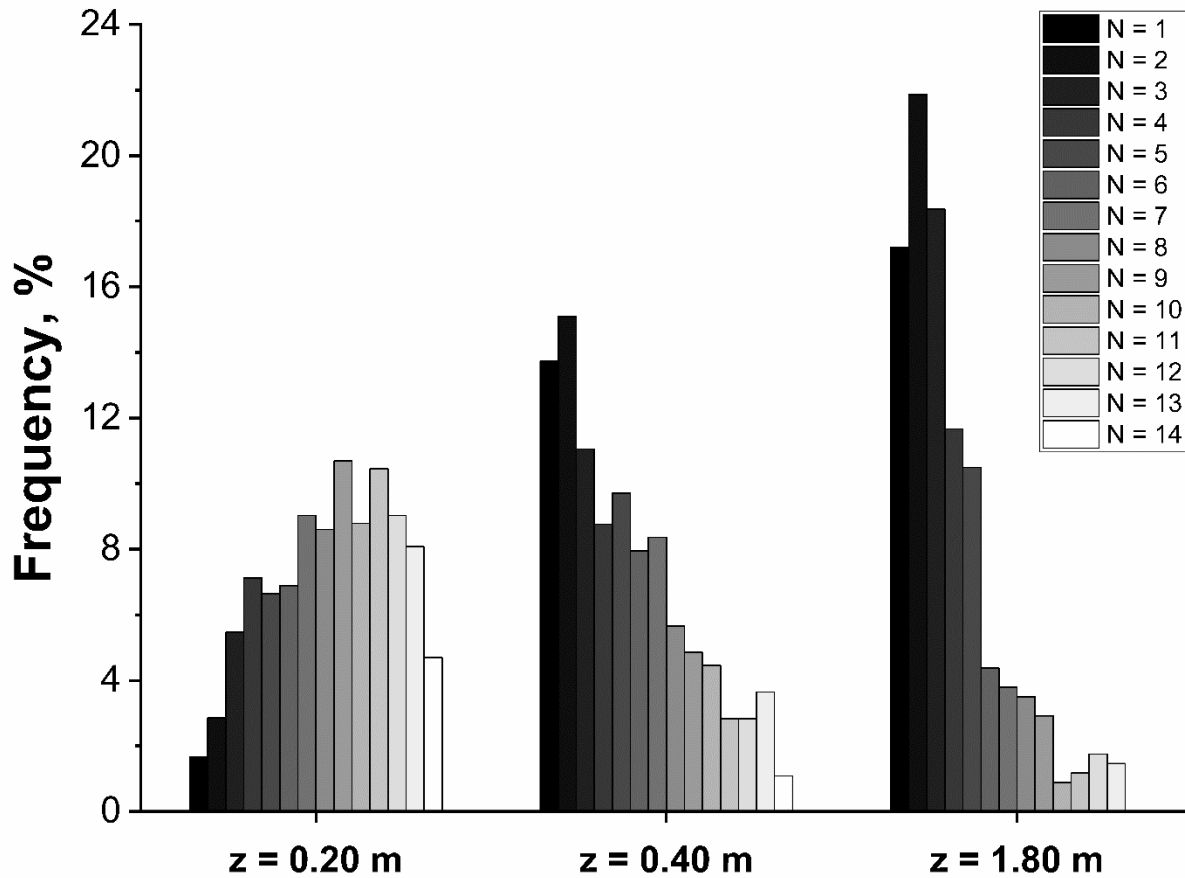
Figure 5.1. Radial Average Particle Cluster Size Distribution at Z = 0.20 m, Z = 0.40 m and Z = 1.80 m with U_{sg} = 1 m/s and G_s = 31.0 kg/m^{2}s. Note: Reported frequencies display a typical 2-5% standard deviation.

One can see in Figure 5.1 that the presence of particle clusters from 1 to 14 average equivalent particles was recorded at the different axial downer levels studied. Furthermore, one can also observe that particle cluster distribution changed from wide and close to symmetrical in the acceleration zone, to a more asymmetrical or skewed distribution, in the fully developed flow section.

In this respect, it can also be observed that at Z = 0.40 m, the particle cluster distribution already resembles the asymmetric shape characteristic of the downer end section. Thus, particle clusters while moving in the downer reactor, evolve from an average of 8

equivalent particles to an average of 4 equivalent particles. This reduction in average cluster size is the result of particle deagglomeration, which is the consequence of cluster-cluster interactions, cluster-wall interactions, and fluid-cluster drag. As well, the mentioned flow stresses on particle clusters led to asymmetric distributions. Thus, in the fully developed stabilized downer flow section, there is a dominant influence of short clusters. This is given the low probability of large clusters surviving.

Furthermore, and in order to predict the cluster size distribution based on the initial operating conditions, the experimentally obtained results were evaluated using three probability distribution functions: Normal, Lognormal, and Gamma(Hahn and Shapiro 1967). Table 5.2 reports the different distribution function parameters with the corresponding standard errors.

Table 5.2 Probability Distribution Function Parameters.

	Z = 0.20 m		Z = 0.40 m		Z = 1.80 m	
	Parameters	**Standard Error**	**Parameters**	**Standard Error**	**Parameters**	**Standard Error**
Normal	μ = 8.423	0.171	5.288	0.129	3.931	0.154
	σ = 3.504	0.121	3.519	0.091	2.867	0.109
Lognormal	μ = 2.006	0.0277	1.400	0.028	1.105	0.039
	σ = 0.569	0.0196	0.783	0.020	0.727	0.028
Gamma	A = 4.164	0.276	2.034	0.098	2.139	0.152
	B = 2.023	0.142	2.598	0.142	1.815	0.145

One can thus see that according to the standard error, the best data fitting for the experimental cluster size results is given by the Lognormal distribution function, with this being adequate at all axial positions studied.

Figure 5.2 reports the fitted Lognormal distribution function for the three axial positions studied. One can notice that the Lognormal distribution function captures the progressive change of the particle cluster distribution from close to symmetrical in the feeding section to strongly asymmetrical in the fully developed flow section.
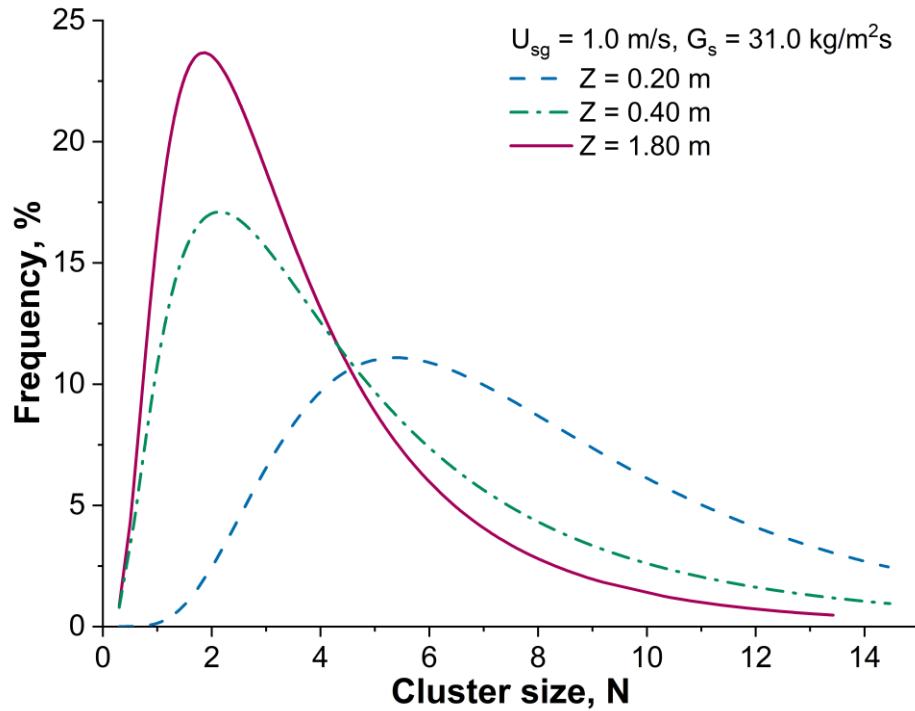
Figure 5.2. Lognormal Distribution Curves with U_{sg} = 1.0 m/s, G_s = 31.0 kg/m²s for Z = 0.20, 0.40, and 1.80 m.

These types of lognormal distributions, as reported in Figure 5.2, reflect the conditions at particle cluster formation, as well as the later randomness of cluster-cluster interactions and fluid dynamic forces exerted on particle agglomerates while moving in the downer.

5.2   Effect of Superficial Gas Velocity and Solid Mass Flux

For every axial position, experiments with four different operating conditions were performed. This was done to study the parametric effect of superficial gas velocity and solids mass flux on the cluster size distribution. For the Z = 0.20 m feeding section position, the cluster size distributions are reported in Figure 5.3.
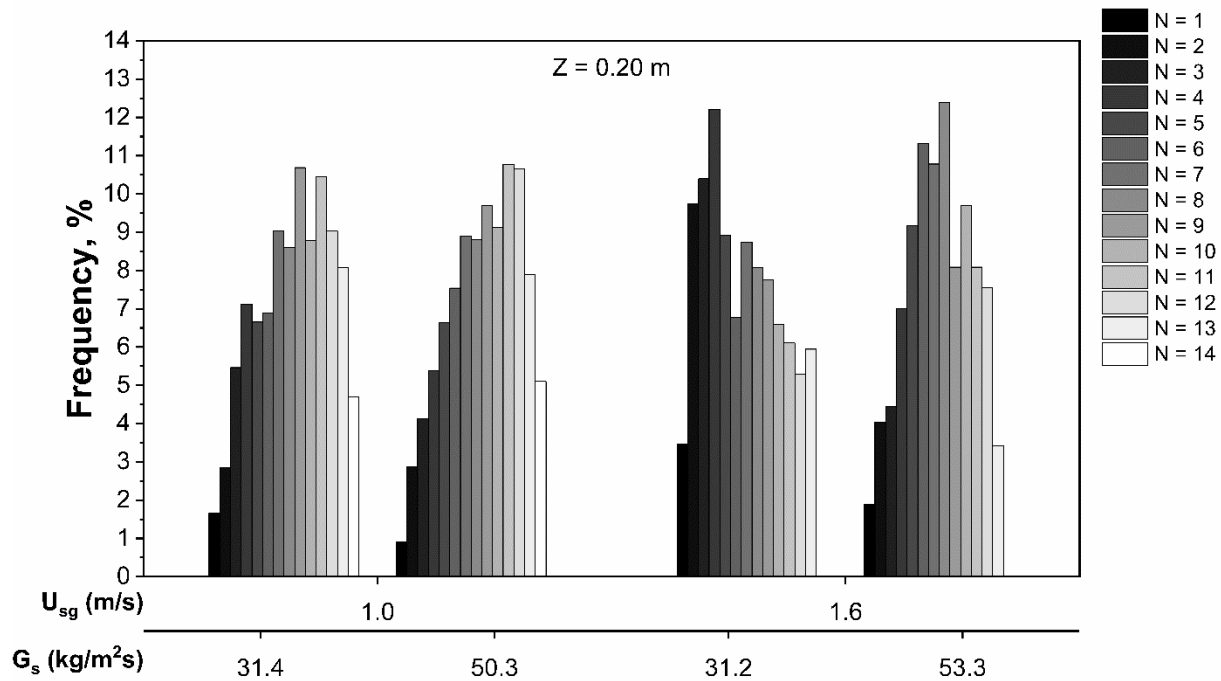
Figure 5.3. Radial Averaged Cluster Size Distribution at Z = 0.20 m at Different Operating Conditions.
Note: Reported frequencies display a typical 5-6% standard deviation.

One can observe in Figure 5.3, that the increasing solids mass fluxes using a 1.0 m/s superficial gas velocity leads to wide cluster size distributions with an important influence of the larger clusters in the distribution. On the other hand, at a 1.6 m/s superficial gas velocity, increasing the solids mass fluxes yields a similar cluster size distribution with, however, a greater contribution of the smaller clusters. This suggests an evolution towards the asymmetrical cluster distribution characteristic of the fully developed flow section. These results are considered sound given the extra kinetic energy provided by the gas flow injected by the air feeder, which contributes to particle cluster disaggregation.

Figure 5.4 describes the particle cluster distributions at the Z = 0.40 m axial position for two particle mass fluxes at the 1.0 m/s and 1.6 m/s superficial gas velocities.
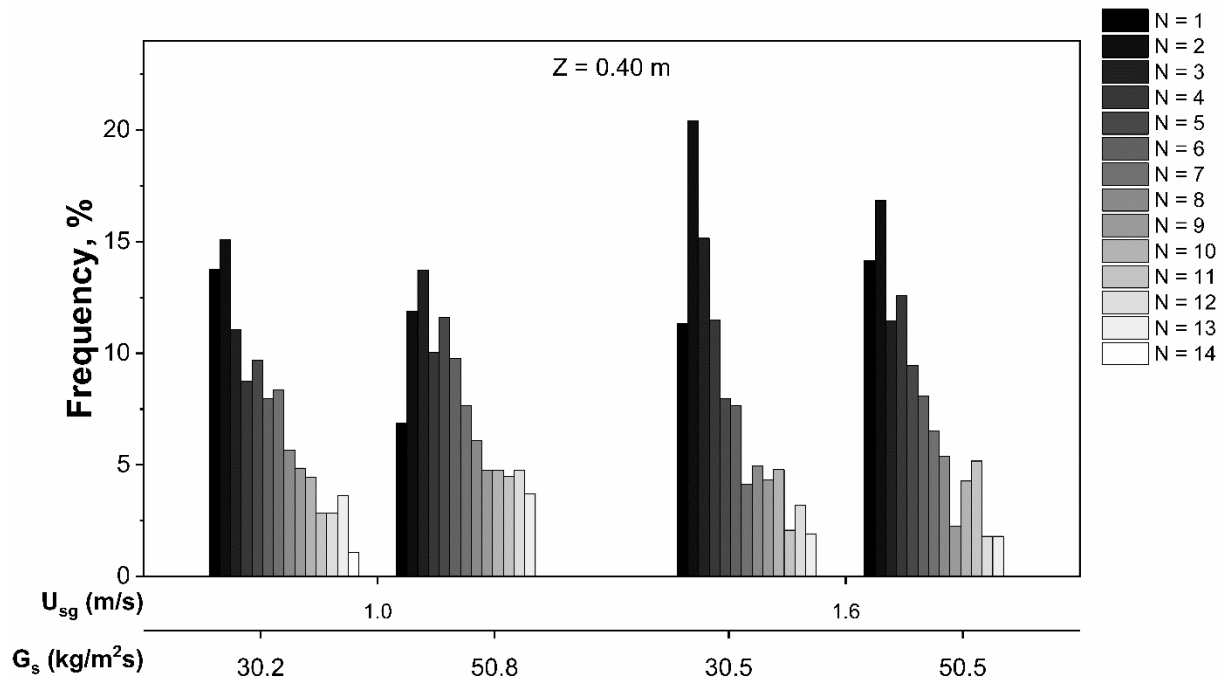
Figure 5.4. Radial Averaged Cluster Size Distribution at Z = 0.40 m with Different Operating Conditions. Note: Reported frequencies display a 4-5% standard deviation.

One can notice that in Figure 5.4 and for all cases considered at Z = 0.4m, the asymmetrical particle cluster size distribution is clearly noticeable. This is the case for all combinations of particle fluxes and superficial gas velocities. It is now apparent that shorter 1-5 particle clusters dominate the overall flow. In particular, this is the case for the 1.6 m/s velocity which resembles the one of a fully developed flow.

Figure 5.5 reports the effect of the various operating conditions on the cluster size distribution at Z = 1.80 m. One can thus observe, in this case, the consistent asymmetric distributions of particle clusters in the downer studied. Clusters composed of 1-2 particles yield the higher distribution frequencies and clusters of 3-4 particles are the average in the distributions as reported in Table 5.3.
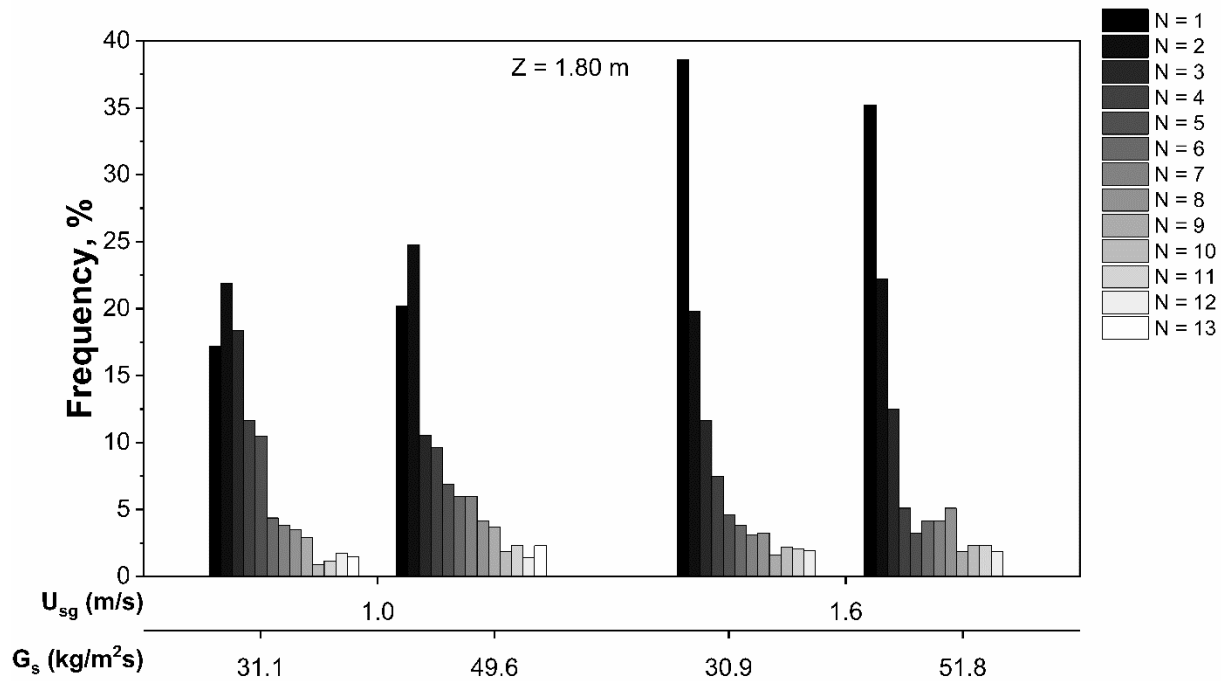
Figure 5.5. Radial Averaged Cluster Size Distribution at Z = 1.80 m with Different Operating Conditions. Note: Reported frequencies display a 2-3% standard deviation.

Table 5.3 provides a summary of the average cluster sizes obtained when using the various experimental conditions of the present study.

Table 5.3 Summary of Average Cluster Sizes.

Condition	U_{sg} (m/s)	G_s (kg/m^{2}s)	Average size (N)
Z = 0.2 m from air distributor			
1	1.0	31.4	8.3
2	1.0	50.3	8.7
3	1.6	31.2	6.8
4	1.6	53.3	7.1
Z = 0.4 m from air distributor			
5	1.0	30.2	5.3
6	1.0	50.8	5.7
7	1.6	30.5	4.6
8	1.6	50.5	4.8
Z = 1.8 m from air distributor			
9	1.0	31.1	3.9
10	1.0	49.6	4.1
11	1.6	31.0	3.1
12	1.6	52.0	3.4

68

It is on this basis that one can conclude the three axial positions selected for data acquisition in the present study, were suitable given that: a) Z = 0.20 m provides valuable fluid dynamic information in the close to feeder section, b) Z=0.40 m gives important data describing gas-particle flow in the intermediate section, with particle clusters evolving towards stabilization, c) Z = 1.80 m provides valuable fluid dynamic data for particle clusters evolving under stabilized flow conditions. Furthermore, it is also valuable to observe the cluster behavior with changes in superficial gas velocity and solids mass fluxes. Here, one can notice the significant influence of the kinetic energy of the feeder air jets impacting and disaggregating the descending particle flow.

5.3 Slip Velocity and Particle Volume Fraction Radial Profiles

In order to fully characterize the cluster particle flow in downers, we must establish cluster slip velocity, which is the difference between cluster velocity and fluid velocity. One must also determine the particle volume fraction or the equivalent solid volumetric concentration in the suspension (Lanza and de Lasa 2017).

To accomplish this, radial measurements with the CREC-GS-Optiprobes were effected as follows: a) two measurements at 0.005 m from the wall on each downer side, and b) 19 measurements spaced every 0.002 m of the remaining distance. Figure 5.6 reports these results for U_{sg} = 1.0 m/s, G_s = 31.0 kg/m²s.
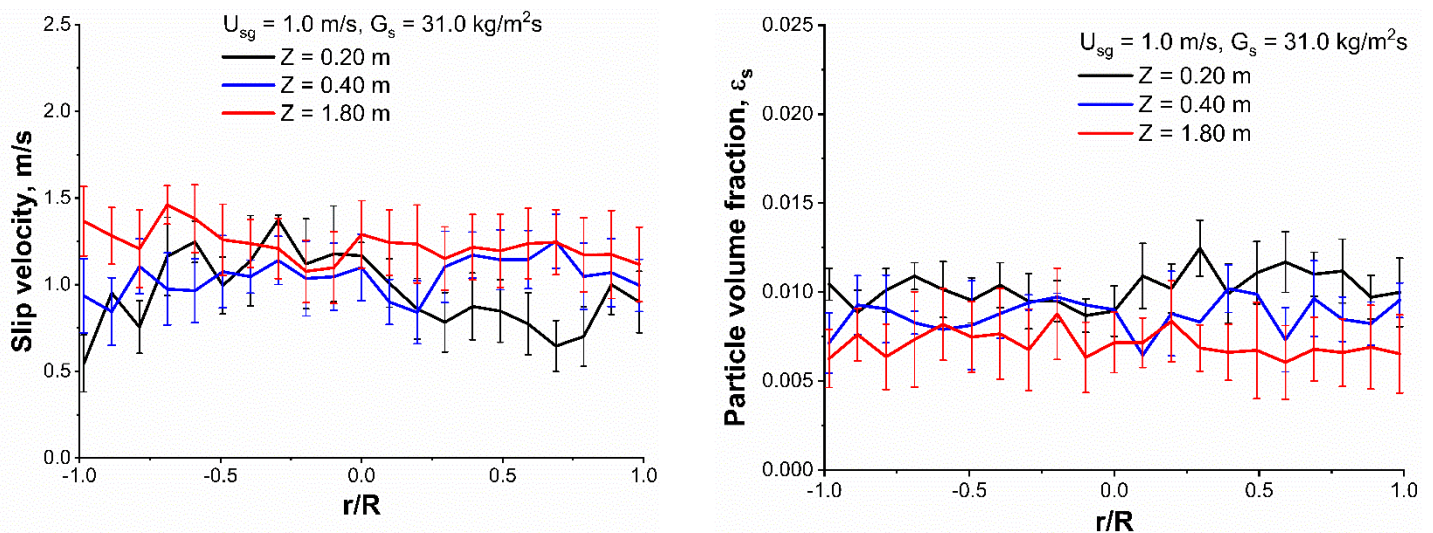
Figure 5.6. Radial Profiles of Cluster Slip Velocity and Particle Volume Fraction at Three Axial Positions with U_{sg} = 1.0 m/s, G_s = 31.0 kg/m²s.

Figure 5.6 shows that the slip velocity tends to progressively increase while clusters are evolving in the downer and moving from Z = 0.20 m to Z = 1.80 m. The slip velocity at Z = 0.40 m shows intermediate values. On the other hand, the particle volume fraction shows the opposite trend; it decreases along the downer length. Furthermore, the radial profiles of both properties become more uniform at Z values greater than 0.40 m.

Figure 5.7 reports similar run results as Figure 5.6; with, however, a higher 50.2 kg/m^{2}s solid mass flux being obtained instead of 31.0 kg/m^{2}s.
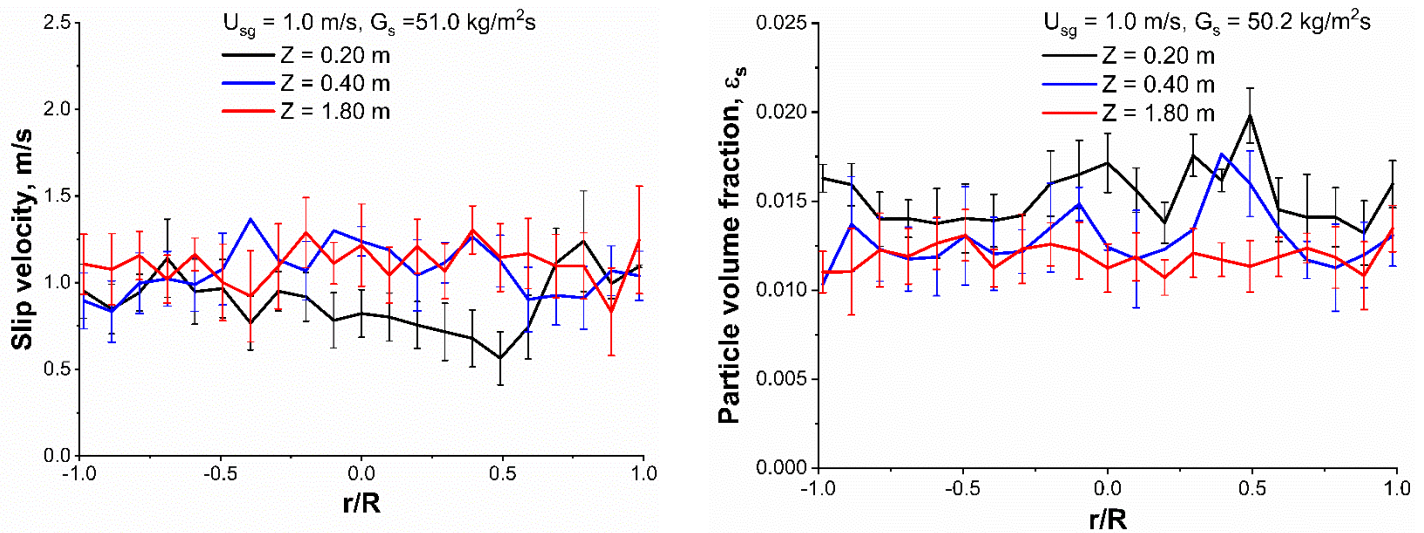
Figure 5.7. Radial Profiles of Cluster Slip Velocity and Particle Volume Fraction at Three Axial Positions with U_{sg} = 1.0 m/s, G_s = 50.2 kg/m2s.

One can observe that at the higher mass fluxes of Figure 5.7, the cluster slip velocity radial distribution remains unaffected except for the one at the Z=0.20 m position. This uneven slip velocity radial distribution at Z = 0.20 m can be assigned to the lower kinetic gas energy per unit weight imparted to the particle cluster flow at 1.0 m/s superficial gas velocities and 50.2 kg/m^{2}s solids mass fluxes. As well, one can also observe in Figure 5.7, while comparing it with Figure 5.6, the significantly augmented particle volume fraction, an understandable result considering the close slip velocities.

Furthermore, Figures 5.8 and 5.9 describe the slip velocity and particle volume fraction radial changes for a 1.6 m/s superficial gas velocity and two solid mass fluxes at 30.9 kg/m^{2}s and 50 kg/m^{2}s.
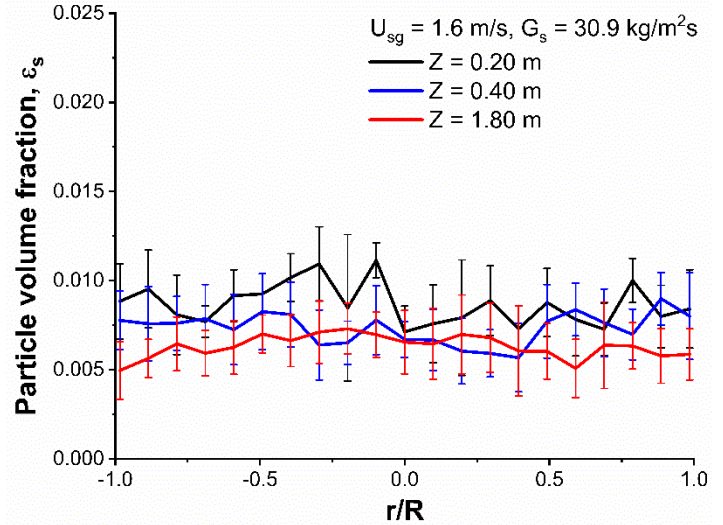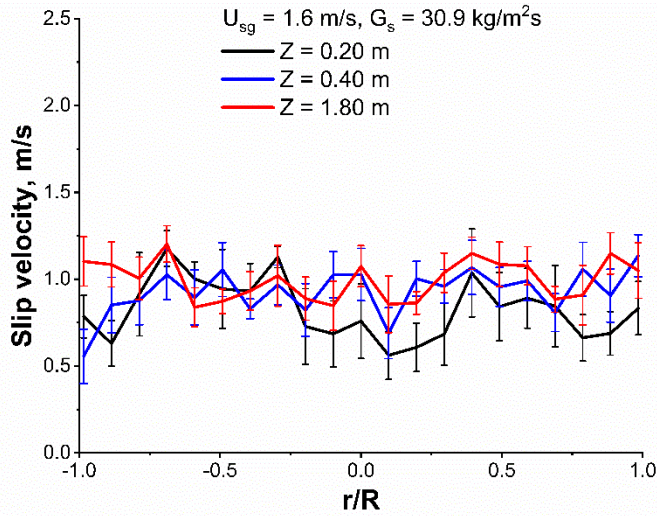
Figure 5.8. Radial Profiles of Cluster Slip Velocity and Particle Volume Fraction at Three Axial Positions with $U_{sg} = 1.6$ m/s, $G_s = 30.9$ kg/m^{2}s.
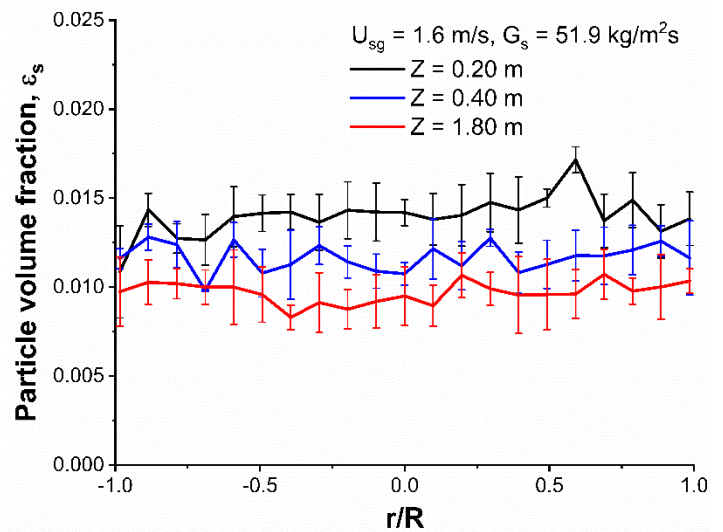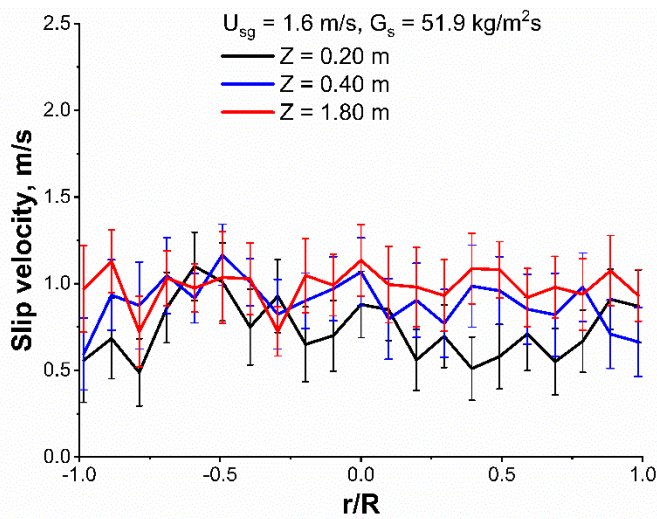
Figure 5.9. Radial Profiles of Cluster Slip Velocity and Particle Volume Fraction at Three Axial Positions with $U_{sg} = 1.6$ m/s, $G_s = 51.9$ kg/m^{2}s.

In Figures 5.8 and 5.9, one can observe that both the cluster slip velocity and particle volume fractions show more uniform radial distributions for both solids fluxes. As well, one can notice at the 1.6 m/s superficial gas velocity, similar results as the ones recorded for the 1.0 m/s superficial gas velocity with the following being observed: a) cluster slip velocities remaining close to the values obtained both at 30.9 kg/m^{2}s and 51.9 kg/m^{2}s solids mass fluxes, b) particle volume fractions increasing at the higher solids fluxes.

71

5.4   Cluster Stabilization Process

Figure 5.10a) reports the measured cluster slip velocity as a function of the cluster size in the acceleration/feeding section. Figure 5.10a) also reports numerically calculated slip velocities as a function of the number of particles in a cluster, calculated with Equation 13. Particles in this simulation are assumed to have a strand shape with the Hölzer-Sommerfeld correlation providing the drag coefficient. One can notice the significant deviation between experimental data and the theoretical "cluster strand" slip velocity predictions at $Z = 0.20$ m. In this case, deviations are assigned to the fact that clusters in the acceleration/feeding section are in fact, better represented by a quasi-spherical shape instead.

Figure 5.10b) on the other hand, compares the experimentally observed cluster slip velocities as a function of the cluster size at $Z = 1.80$ m in the stabilized region, with calculated slip velocities obtained using Equation 13. The strand shape considered is the one formed via the random particle selection described in Section 3.3. One can certainly see that in this case at $Z = 1.80$ m, both experimentally measured and theoretically predicted cluster velocity and particle cluster size are in agreement.

a)

b)
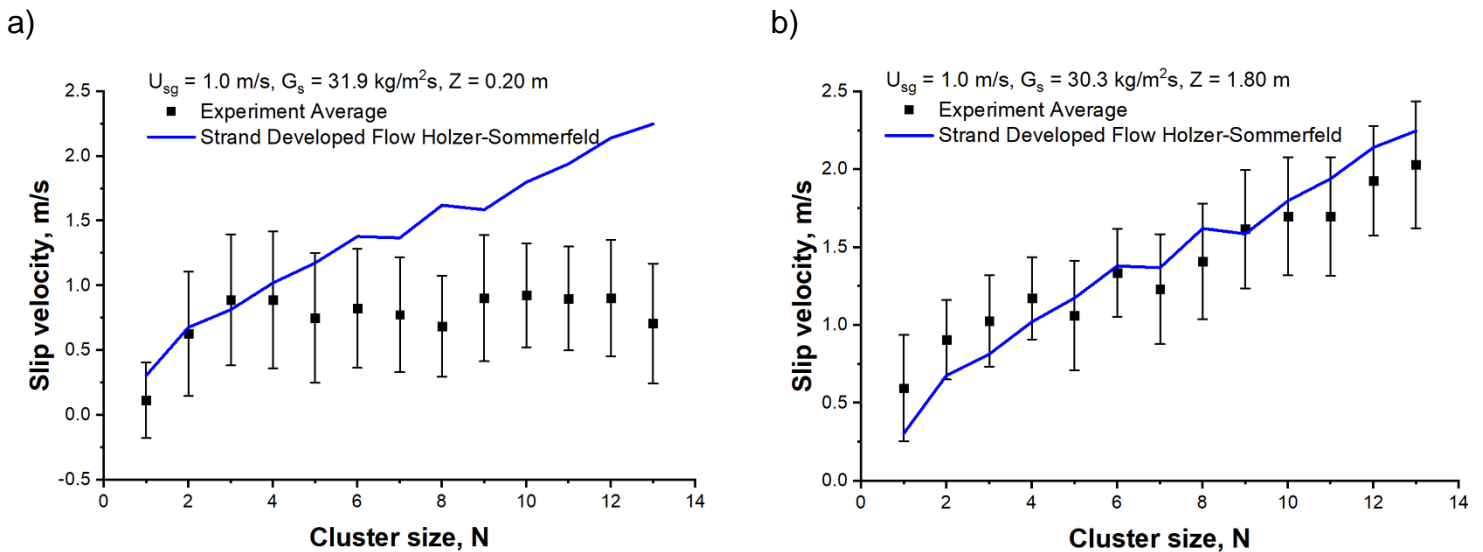
Figure 5.10. Cluster Slip Velocity versus Size at a) Z = 0.20 m, and b) Z = 1.80 m.

However, and to address the observed model and experimental discrepancies between the dependence of cluster slip velocity and cluster size at $Z = 0.20$ m, a particle aggregate resembling a sphere is proposed. The diameter of this particle aggregate is equal to the

distance detected by the probes, $N \cdot d_p$, and filled with particles at minimum fluidization voidage. The characteristics of this "spherical particle cluster" configuration can thus, be described by Equations 5-1 and 5-2, as follows:

$$V_{c,sph} = \varepsilon_{s,mf} \frac{1}{6} \pi (Nd_p)^3 \tag{5-1}$$

$$A_{c,sph} = \frac{\pi}{4} (Nd_p)^2 \tag{5-2}$$

Regarding the particle cluster, Equation 4-14 can be applied to the stabilized downer zone only. However, to simulate the feeding section of the downer, Equations 5-3a and 5-3b with a non-zero unsteady state term must be considered instead, as follows:

$$\frac{du_{slip}}{dt} = \frac{(\rho_p - \rho_f)}{\rho_p} g + \frac{\rho_f A_{c,sph} C_D u_{slip}^2}{2\rho_p V_{c,sph}} \quad for \ u_p < u_f \tag{5-3a}$$

$$\frac{du_{slip}}{dt} = \frac{(\rho_p - \rho_f)}{\rho_p} g - \frac{\rho_f A_{c,sph} C_D u_{slip}^2}{2\rho_p V_{c,sph}} \quad for \ u_p > u_f \tag{5-3b}$$

Thus, these equations were solved numerically and as a result, a "spherical cluster" slip velocity was calculated at every downer axial length in the downer feeding/acceleration section.

Figure 5.11 shows the predictions of the "spherical cluster" slip velocity model in terms of its frequency distribution for various cluster sizes.
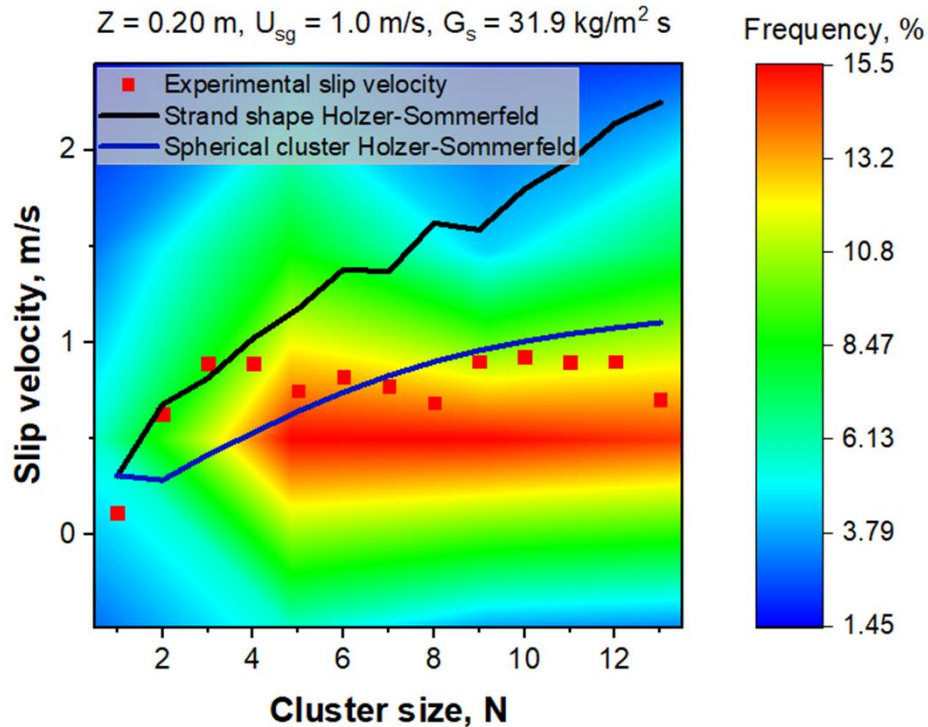
Figure 5.11. Cluster Slip Velocity versus Size for Two Different Cluster Shapes at Z = 0.20 m. Different Colours Refer to Slip Velocity Frequencies for Various Cluster Sizes.

One can thus see in Figure 5.11, that the spherical clusters are more adequate to describe the cluster slip velocity in the feeding section at $Z = 0.20$ m, than non-spherical clusters with particles evolving as a strand of particles.

Figure 5.12 provides a schematic description of these geometrical cluster changes when clusters evolve in a downer unit. On this basis, particle clusters in downers can be viewed as follows: a) At the downer entry section, particle agglomerates move in a "quasi-spherical" shape configuration, b) Following this, particles change progressively from a "quasi-spherical" shape to a "strand shape". This "strand shape" is achieved in the fully developed flow section.
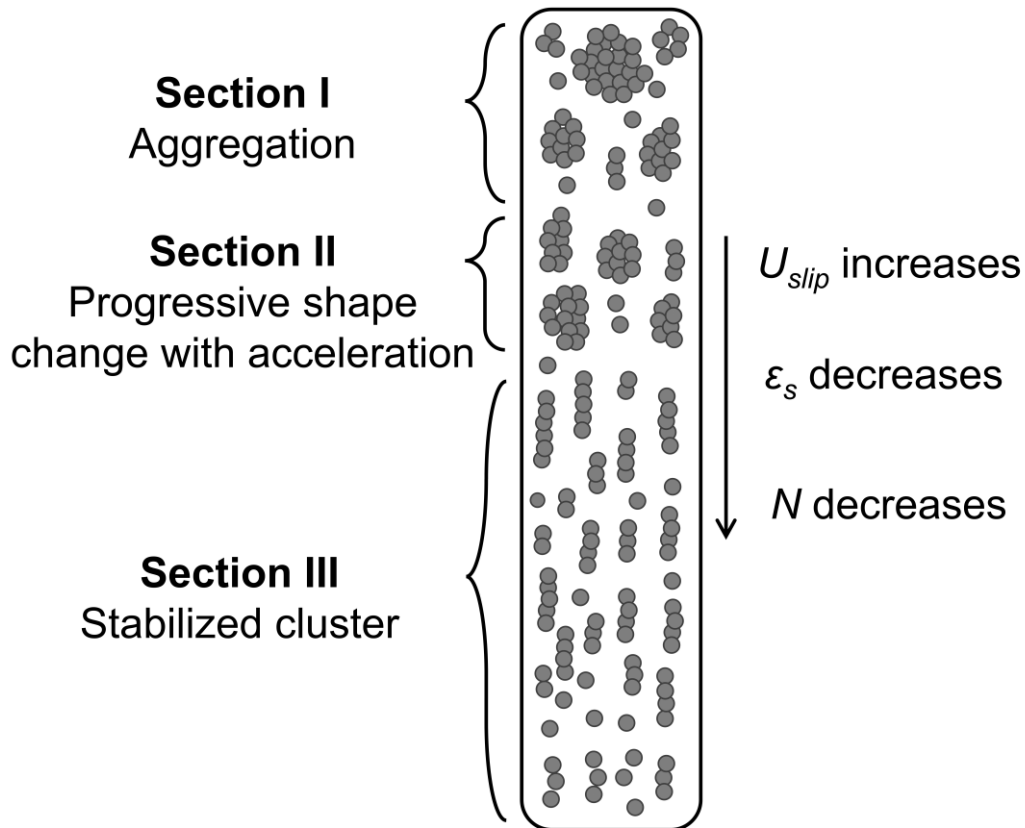
Figure 5.12. Acceleration and Stabilization of Clusters Inside the Downer.

In summary, studying flow patterns in downers involves the consideration of both cluster size distributions and cluster slip velocities. These particle clusters flow in the near feeding section as "quasi-spherical" with symmetrical particle cluster distributions. However, these particle clusters are subject to dynamic changes as particles move in the downer. They evolve from "quasi-spherical" to "strand" cluster shaped aggregates, reaching the fully developed flow zone, having asymmetrical cluster size distributions and 1 to 5 equivalent particle cluster sizes. These changes both in particle cluster size and shape can be attributed to the cluster motion in a turbulent gas-solid suspension, shear stresses exerted on the agglomerate and particle agglomerate interactions.

5.5   Conclusions

c) Studies developed confirmed that the selected downer feeder design provides good gas-solid mixing with the selected air distributor.

d) Particle cluster dynamics were studied in the downer unit for a wide range of operating conditions, changing superficial gas velocity and solid mass fluxes, at three different axial positions along the downer.

e) Particle clusters in the near downer feeding section appear to be larger, with between 1-15 particles and having a "quasi-spherical" shape.

f) Particle cluster distributions change in the downer from a wide and close to symmetrical distribution in the feeding section to a skewed distribution in the stabilized section. In the stabilized section, 1-5 particle clusters are the most frequently observed.

g) Increasing the superficial gas velocity leads consistently to smaller clusters. On the other hand, higher solid mass fluxes have the opposite effect, although it is not as significant.

6 Numerical modeling and Hybrid Cluster numerical model

6.1 Fluid Phase Equations-Continuous Phase

The fluid mass and momentum equations for dense particle flow, using MP-PIC are given by Equations 6-1 and 6-2:

$$\frac{\partial \varepsilon_f \rho_f}{\partial t} + \nabla \cdot (\varepsilon_f \rho_f u_f) = 0 \tag{6-1}$$

$$\frac{\partial (\varepsilon_f \rho_f u_f)}{\partial t} + \nabla \cdot (\varepsilon_f \rho_f u_f u_f) = -\nabla p - F + \varepsilon_f \rho_f g + \nabla \cdot (\varepsilon_f \tau_f) \tag{6-2}$$

where u_f is the fluid velocity; ε_f is the fluid volume fraction; ρ_f is the fluid density; τ_f is the fluid stress tensor; F is the interphase momentum transfer.

6.2 Solid Phase Equations-Discontinuous Phase

For the particle field, a particle distribution function, f, is considered. f is a function of particle spatial location, x, particle mass m_p, particle velocity u_p, and time t: $f(x, u_p, m_p, t)$. The transport equation for f is given by Equations 6-3 and 6-4:

$$\frac{\partial f}{\partial t} + \frac{\partial (f u_p)}{\partial x} + \frac{\partial (f \dot{u}_p)}{\partial u_p} = \left(\frac{\partial f}{\partial t}\right)^D_{coll} \tag{6-3}$$

$$\dot{u}_p = \frac{d u_p}{dt} = D_s(u_f - u_p) - \frac{1}{\rho_s} \frac{\partial p}{\partial x} - \frac{1}{\varepsilon_s \rho_s} \frac{\partial \tau_c}{\partial x} + g \tag{6-4}$$

Where $\dot{u}_p$ is the particle acceleration; u_f is the fluid velocity; ε_s is the particle volume fraction; ρ_s is the solid material density; p is the fluid pressure; g is the gravity acceleration; τ_c is the particle contact stress. D_s is the drag function which is defined by Equation 6-5 as follows:

$$D_s = \frac{3}{8} C_D \frac{\rho_f |u_f - u_p|}{\rho_s r_p} \tag{6-5}$$

The right-hand side of Equation 3 relates to the collision damping term defined by Equation 6-6 as follows:

$$\left(\frac{\partial f}{\partial t}\right)_{coll}^{D} = \frac{f_D - f}{\tau_D} \tag{6-6}$$

where τ_D is the collision damping time; and f_D is the probability distribution function obtained by collapsing the velocity dependence of f to a delta function centered at the local mass-averaged particle velocity, $\overline{u_p}$ given by Equation 6-7:

$$f_D = \left[\int f du_p\right]\delta(u_p - \overline{u_p}) \tag{6-7}$$

Additional information about the collision damping term and the particle and fluid transport equations can be found in O'Rourke and Snider (O'Rourke and Snider 2010) and Snider (Snider 2001).

Furthermore, and considering the f particle distribution function, the gas phase volumetric fraction is calculated as per Equation 6-8:

$$\varepsilon_f = 1 - \frac{1}{V_{cell}} \iint f \frac{m_p}{\rho_p} dm_p du_p \tag{6-8}$$

As well, the interphase momentum transfer function introduced in Equation 2 is defined with f by Equation 6-9 as follows:

$$F = \int\int f m_p [D_s(u_f - u_p) - \frac{1}{\rho_s}\nabla p] dm_p du_p \tag{6-9}$$

6.3   Hybrid Experimental Numerical Cluster Model

Particles evolve in a downer unit by going through a process of acceleration and stabilization. At the entrance of the downer, it is hypothesized that particles aggregate, forming clusters of a quasi-spherical shape, packed with a particle voidage close to the one of minimum fluidization, designated as ε_{mf}. Equations 6-10 – 6-12 describe such a cluster as follows:

$$V_{c,sphere} = \varepsilon_{mf}\frac{1}{6}\pi(L)^3 \tag{6-10}$$

$$A_{c,sphere} = \frac{\pi}{4}(L)^2 \tag{6-11}$$

$$L = N * d_p \qquad\qquad (6-12)$$

Where L is the axial length of a cluster; and N is the number of particles with an average diameter, d_p, in the axial direction.

On the other hand, when clusters stabilize inside the downer, they display a strand or a "train of particles" shape. Thus, the cluster volume can be calculated with Equation 6-13 as follows:

$$V_{c,strand} = \frac{1}{6}\pi d_p^3 N \qquad\qquad (6-13)$$

As well, the strand shaped cluster cross-sectional area normal to the flow can be defined with Equation 6-14 as follows:

$$A_{c,strand} = \frac{\pi}{4}d_p^2 \qquad\qquad (6-14)$$

One can notice that particle configurations in either the acceleration or the stabilized region, may display the same axial length as shown in Figure 6.1, having, however, significantly different cluster volumes.
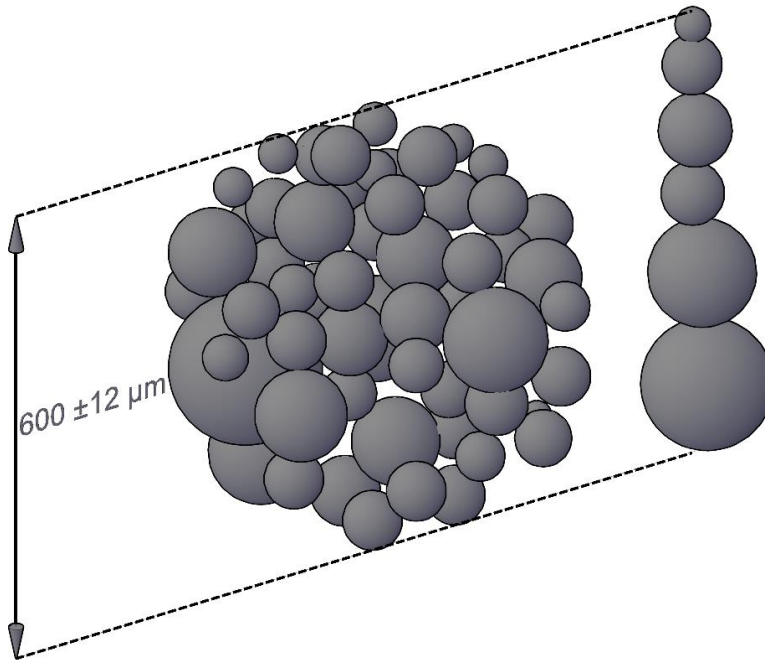
Figure 6.1. Particles Forming a Particle Cluster in Two Different Configurations: Spherical and Strand Shape

As discussed in a recent article, (Medina-Pedraza and de Lasa 2020) experimental measurements at various axial positions, were obtained with the CREC-GS-Optiprobes (Ashraful Islam, Krol, and de Lasa 2011). These measurements allow recording both individual cluster velocities and particle volume fractions. An example of the axial cluster size distribution obtained experimentally at both the entry and stabilized downer regions is shown in Figure 6.2.

a)

b)
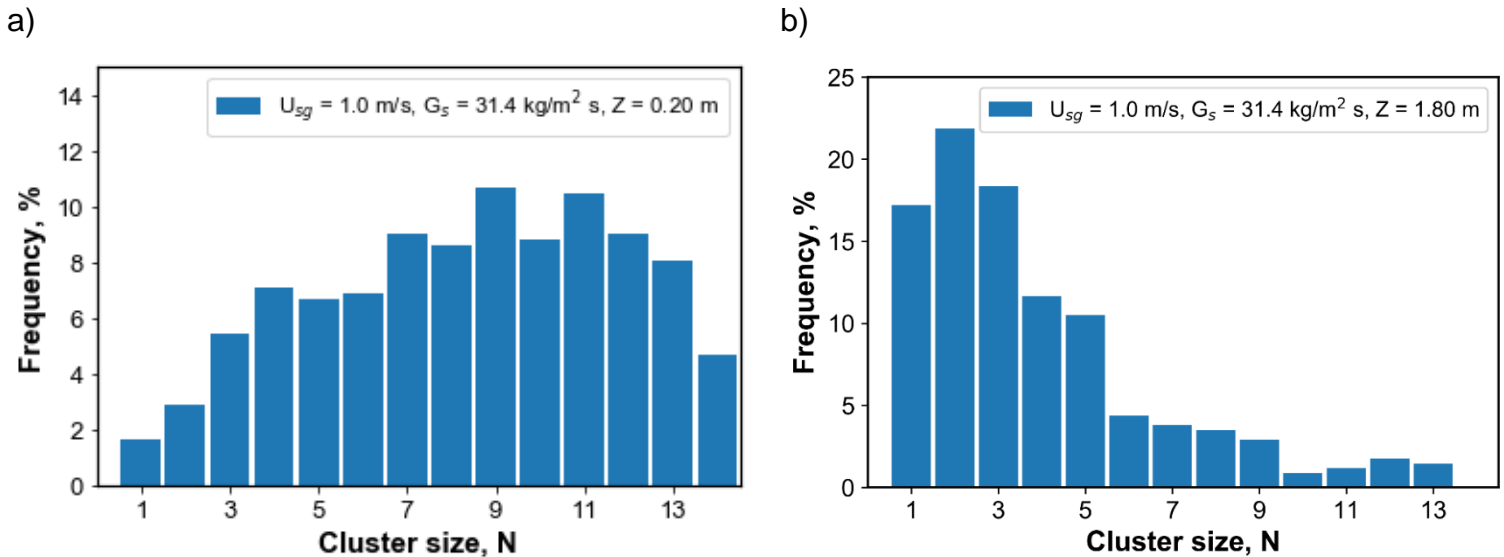
Figure 6.2. Cluster Size Distribution at U_{sg} = 1.0 m/s, G_s ≈ 31 kg/m2s for (a) Z = 0.20 m, (b) Z = 1.80 m

As claimed by Lanza et al.(Lanza, Islam, and Lasa 2016a), these data, such as axial particle cluster size distributions are valuable, given that they can be considered into hybrid CPFD Barracuda VR numerical simulations.

6.4 Drag Coefficient Correlations

The particle cluster drag coefficient is a critical parameter in downer simulations. In this respect, Chhabra et al. (Chhabra, Agarwal, and Sinha 1999) used an extensive experimental dataset and compared different methods for assessing particle cluster drag coefficients. In these studies, the Ganser correlation for non-spherical particles yielded the lowest percentual error for the expected cluster configurations in the gas-solid system under study.

Based on these findings, Lanza (Lanza and de Lasa 2017) selected the Ganser Drag Model for the calculations reported in their work. The Ganser drag coefficient is calculated with equations 6-15 and 6-16 as follows:

$$C_D = \frac{24}{Re_p K_1 K_2}\left(1 + 0.1118\left(Re_p K_1 K_2\right)^{0.6567}\right) + \frac{0.4305}{1 + \dfrac{3305}{Re_p K_1 K_2}} \tag{6 − 15}$$

$$K_1 = \frac{3}{1 + 2\phi^{-0.5}} \ ; \ K_2 = 10^{1.8148(-log\phi)^{0.5743}} \tag{6 − 16}$$

More recently, it was reported by Bagheri (Bagheri and Bonadonna 2016) that when using the Hölzer-Sommerfeld Model (Hölzer and Sommerfeld 2008), a lower error was obtained in the calculation of the motion of non-spherical particles, as compared to when the Ganser Correlation was used. The Hölzer-Sommerfeld Correlation uses three shape parameters: (a) crosswise sphericity, $\phi_\perp$; (b) standard sphericity, ϕ; and (c) length-wise sphericity, $\phi_\parallel$. Consistent with this, the drag coefficient in the present work, is calculated according to Equation 6-17.

$$C_D = \frac{8}{Re_p\sqrt{\phi_\parallel}} + \frac{16}{Re_p\sqrt{\phi}} + \frac{3}{\sqrt{Re_p}\phi^{0.75}} + 0.42 * 10^{0.4(-log\phi)^{0.2}}\left(\frac{1}{\phi_\perp}\right) \tag{6 − 17}$$

The sphericity shape factors are described by the ratios presented in Equations 6-18 – 6-20.

$$\phi_\parallel = \frac{cross-sectional\ area\ of\ the\ volume\ equivalent\ sphere}{\frac{1}{2}cluster\ surface\ area - cluster\ projected\ area,\ parallel\ to\ flow} \tag{6 − 18}$$

$$\phi = \frac{surface\ area\ of\ volume\ equivalent\ sphere}{cluster\ surface\ area} \tag{6 − 19}$$

$$\phi_\perp = \frac{cross-sectional\ area\ of\ the\ volume\ equivalent\ sphere}{cluster\ projected\ area,\ normal\ to\ flow} \tag{6 − 20}$$

As a result, and considering the potential shape change of particle clusters while evolving in downer units, the model given by Equations 6-17- 6-20 is considered in the simulations.

6.5   Conclusions

a) A Hybrid Experimental-Numerical Cluster CPFD model can be considered for developing CPFD fluid dynamic simulations in a downer reactor unit, including both the feeding section and the stabilized flow section,

b) The postulated Hybrid CPFD model requires the experimentally observed cluster particle size distribution in order to be able to develop the downer simulations.

c) The proposed Hybrid CPFD model has to include a suitable drag coefficient correlation, adaptable to the different observed cluster geometries, close to spherical and strand type, observed in the different downer sections.

7 Cold flow model validation simulation conditions, results and discussion

7.1 Catalyst

The solid particles selected in the present study, are Fluid Catalytic Cracking (FCC) catalyst particles with an apparent particle density of 1722 kg/m^3. The particles have a mean diameter of 84.4 μm and a standard deviation of 33.6 μm.

7.2 Downer Geometry

The chosen downer geometry is a replica of an available experimental system, consisting of a cyclone, an air distributor, and a column of 0.051 m ID and 2 m in height. Details of the selected downer unit are provided in Figure 7.1.
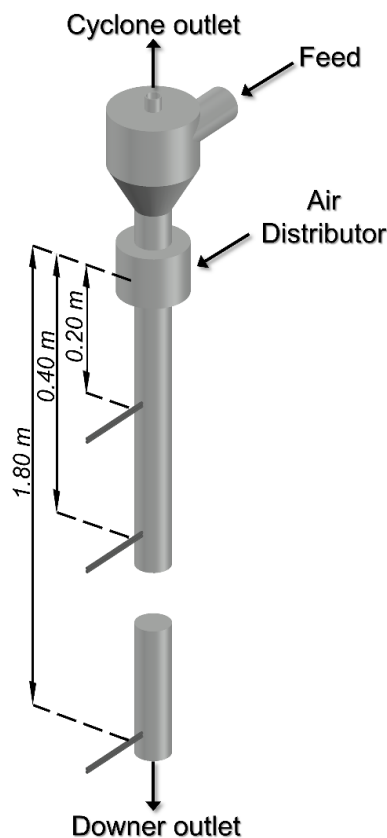
Figure 7.1. Dimensions of the Experimental Downer Unit Selected for the CPFD Simulations

7.3 Simulation Conditions

Regarding numerical simulation and fluid dynamic modeling, the Hybrid Experimental-Numerical Cluster Model was applied to both the acceleration and the fully developed flow sections of the downer. This Hybrid Experimental-Numerical Model uses the cluster axial size distribution determined experimentally as the particle size distribution in the simulations. As well, the considered model accounts for possible cluster shape, in order to establish the best particle cluster geometry to best fit the experimental data. Table 7.1 reports the various input parameters for the CPFD Barracuda VR simulations.

Table 7.1. Input Parameters and Initial Conditions for Barracuda Simulation

	Parameter	Value
Heat transfer	Isothermal flow	T = 300 K
Gravity	Z component of gravity	-9.81 m/s^2
Fluid properties	Density	1.17285 kg/m^3
	Molecular weight	28.9652
	Viscosity	1.8495x10-5 Pa s
Solid properties	Density	1722 kg/m^3
	Molecular weight	101.961
Particle-to-particle interaction	Close-pack volume fraction	0.55
	Maximum redirection from collision	60%
Particle-fluid interaction	Drag model	Hölzer-Sommerfeld / Ganser
	Sphericity	Table 7.3
Particle normal stress model	Harris-Crighton model	
	P_s constant	1
	B constant	3
	Eps constant	1e-8
	Factor of average velocity	0.8
Particle-to-wall interaction	Normal-to-wall momentum retention	0.99
	Tangent-to-wall momentum retention	0.99

	Diffuse bounce	0
Initial conditions	Gas velocity	0
	Gas pressure	113100 Pa

The numerical model also requires the definition of boundary condition at the inlet and outlet of the cyclone and the downer outlet at the bottom. The values for these conditions are reported in Table 7.2

Table 7.2. Boundary Conditions

Cyclone inlet pressure	113100 Pa
Cyclone outlet pressure	113100 Pa
Downer outlet pressure	113100 Pa
Cyclone inlet air flow	Table 7.3
Particle feed	Table 7.3
Particle feed per average volume, n_p	6000
Fluid velocity for both cyclone and downer at the wall	0 m/s

Additionally, the numerical solver parameters and time settings are specified in Table 7.3.

Table 7.3. Solver settings and time controls

Solver settings	Maximum volume iteration	10
	Volume residual	1e-7
	Maximum pressure iteration	2000
	Pressure residual	1e-6
	Maximum velocity iteration	50
	Velocity residual	1e-7
	Maximum energy iteration	100
	Energy residual	1e-6
	Friction coefficient	0.1
Time controls	Time step	0.001 s
	End time	20 s

One should note, the values for the particle-wall interaction were chosen according to previous studies with similar systems (Lanza and de Lasa 2017; F. Li et al. 2012; Kadyrov, Li, and Wang 2019; Ariyaratne, Ratnayake, and Melaaen 2017).

As mentioned above, the MP-PIC Method used in CPFD Barracuda VR employs an Eulerian grid to solve the fluid phase equations and to account for the solid particle phase. Furthermore, it is important to note that the n_p value reported in Table 7.1 refers to the particle feed per average volume, set at the boundary condition. This value is estimated using Equation 7-1 as follows:

$$n_p = \frac{N_p}{N_{cells}\varepsilon_P} \qquad\qquad (7-1)$$

where N_p is the total number of computational particles in the system, N_{cells} is the number of Eulerian cells which will be filled with particles at a volume fraction of ε_P.

In our view, a n_p value larger than 6000 would mean longer and unjustified computational times. One can deduce this, given that Lanza et al (Lanza and de Lasa 2016) demonstrated that for a downer unit operated under similar conditions, a value of 3000 was high enough to ensure result accuracy.

7.4   Grid Independence Test

CPFD Barracuda VR uses a structured grid for the simulations. The accuracy of the numerical solutions of the differential equations depends on several factors. The two most important factors are the number of cells that constitute the mesh geometry, and the time step used to solve the various differential equations. As well, the Courant Flow Number (CFL) is another key parameter to consider in the numerical calculations. The CFL measures the flow of fluid and the number of particles moving through each cell, with a value below 1 being desirable (Courant, Friedrichs, and Lewy 1967).

The computational time, which is the real time that is needed to complete a simulation, is proportional to the number of cells in the system and inversely proportional to the time step length. A strategy to obtain the most accurate results without consuming an excessive amount of computer time is to perform simulations calculating deviations at three different degrees of grid refinement: (a) coarse, (b) medium, and (c) fine. Thus, simulations are developed for each grid and errors are calculated. If this value is below 1%, the grid is sufficiently accurate. In the case of the present study, the average fluid

velocity at an axial position of 0.1 m from the downer outlet, is selected for the grid independence test.

$$\% \, Error \, 1 = \frac{Fluid \, Velocity \, (Medium) - Fluid \, Velocity(Coarse)}{Fluid \, Velocity \, (Medium)} 100$$

$$\% \, Error \, 2 = \frac{Fluid \, Velocity \, (Fine) - Fluid \, Velocity(Medium)}{Fluid \, Velocity \, (Fine)} 100$$

The dimensions of the grid used for the independence test as well as the corresponding errors at three axial positions are reported in Table 7.3.

Table 7.4. Grid Size and Grid Independence Test Results

		Coarse	Medium	Fine	Error 1	Error 2
	Grid size (mm)	10.24x10.24x20.76	7.31x7.31x14.76	5.68x5.68x10.93		
	Cells	4739	9355	17155		
Fluid velocity (m/s)	Z = 0.20	-1.112	-1.061	-1.063	-4.72	0.12
	Z = 0.40	-1.123	-1.062	-1.059	-5.76	-0.27
	Z = 1.80	-1.106	-1.057	-1.064	-4.63	0.65

According to the percentual errors reported in Table 7.2, the medium grid was considered accurate enough and, as a result, it was used in all ensuing reported simulations. The resulting feeding and downer column sections of the grid are described in Figure 7.2.
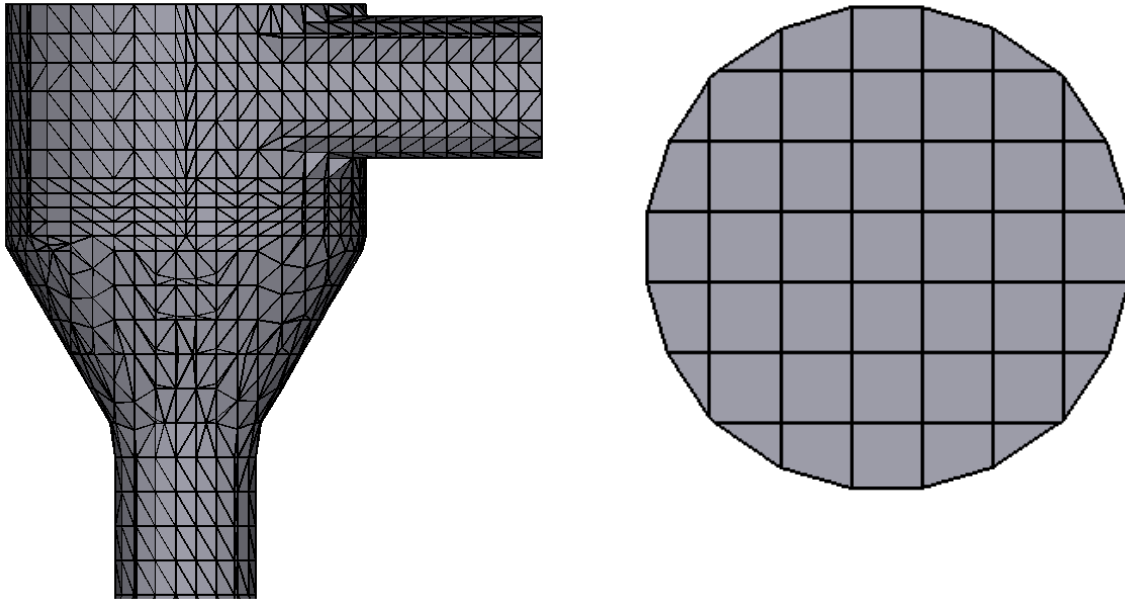
Figure 7.2. Medium Grid Selected for CPFD Simulations

7.5 Boundary Conditions

Four boundary conditions were specified in each simulation: (a) two mass flows, one for the cyclone inlet and one for the cyclone exit; (b) a pressure boundary condition for the downer outlet; and (c) the size and mass flow rate for each of the eight injection nozzles. These boundary conditions are depicted in Figure 7.3 and the corresponding values are reported in Table 7.3.

Regarding the cyclone outlet and the injection mass flows, they were chosen to be in agreement with the conditions selected for the experiments, as reported in Medina-Pedraza and de Lasa (Medina-Pedraza and de Lasa 2020). As well, the inlet solid mass flow was calculated by developing a mass balance which considers the determined outlet mass flow from the experiments, as proposed by Lanza et al. (Lanza, Islam, and de Lasa 2012).
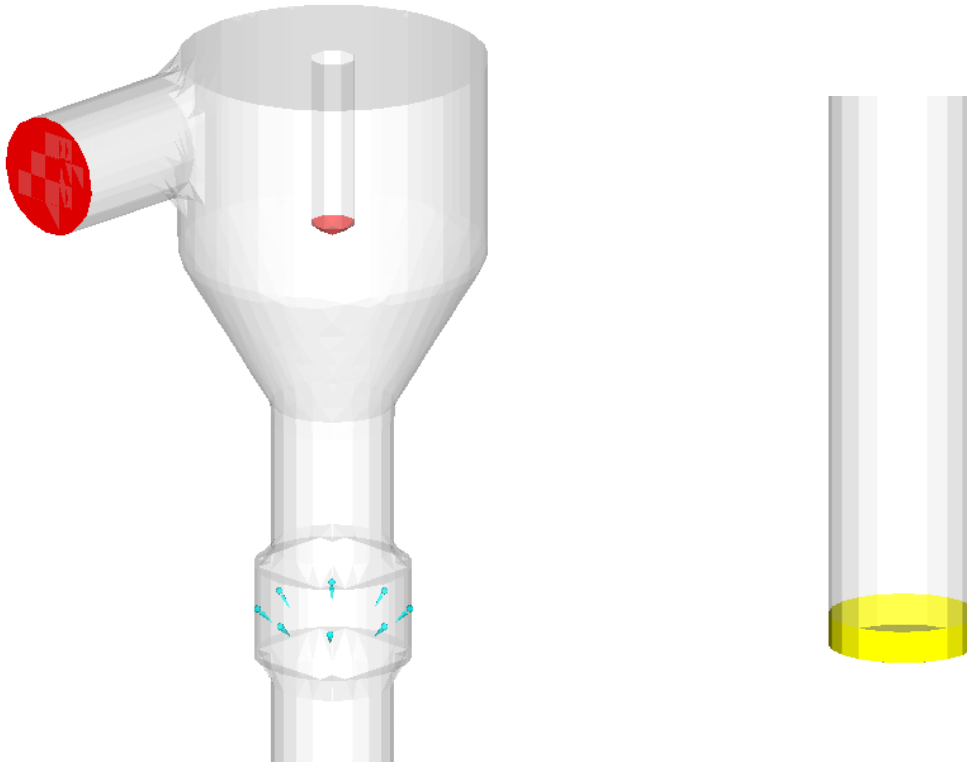
Figure 7.3. Boundary Conditions

7.6 Strategy for the Hybrid Model Evaluation

Given that an important objective of this research is to evaluate the ability of the hybrid model to describe the downer operation in the acceleration (feeding) section, several methodological steps were considered: (a) the CREC-Optiprobes data from experiments were used to calculate cluster size distribution data; (b) the determined cluster size distributions were incorporated into the numerical downer model, to test its ability to predict particle cluster velocities and particle volumetric fractions.

7.6.1 Cluster Configuration and Drag Correlation Evaluation

In order to progress with the Hybrid Barracuda simulations, two different drag models originally proposed by Ganser(Ganser 1993) and Hölzer-Sommerfeld(Hölzer and Sommerfeld 2008) were considered first, using the average cluster size distribution as reported in Table 7.4.

As well, the drag correlation parameters were calculated for three different cluster shapes: (a) the cluster strand, constituted by a train of particles; (b) a prolate spheroid, with the

minor semi-axis equal to half the length of the major semi-axis; c) a sphere, with the diameter equal to the cluster axial length recorded by the CREC-GS-Optiprobes.

The spheroid cluster mentioned above can be described with Equations 7-2 to 7-5, as follows:

$$V_{c,spheroid} = \varepsilon_{mf} \frac{4}{3}\pi a b^2 \qquad (7-2)$$

$$A_{c,spheroid} = \pi b^2 \qquad (7-3)$$

$$a = 0.5 * N * d_p \qquad (7-4)$$

$$b = 0.5 * a \qquad (7-5)$$

The evaluation of these two drag models with the three shapes is reported in Figure 7.4, for three axial positions: Z = 0.20 m, Z = 0.40m, and Z = 1.80 m. Each simulation was run for 20 seconds and the results were obtained from the time-averaging of the last five seconds.

a)
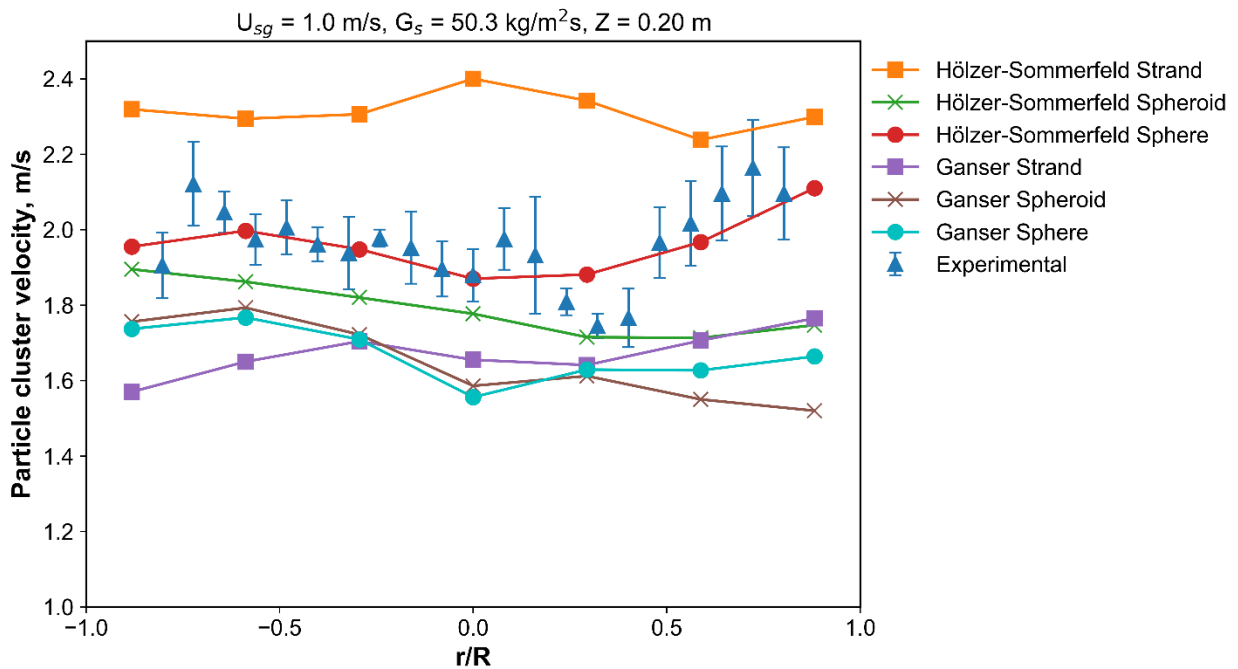
b)
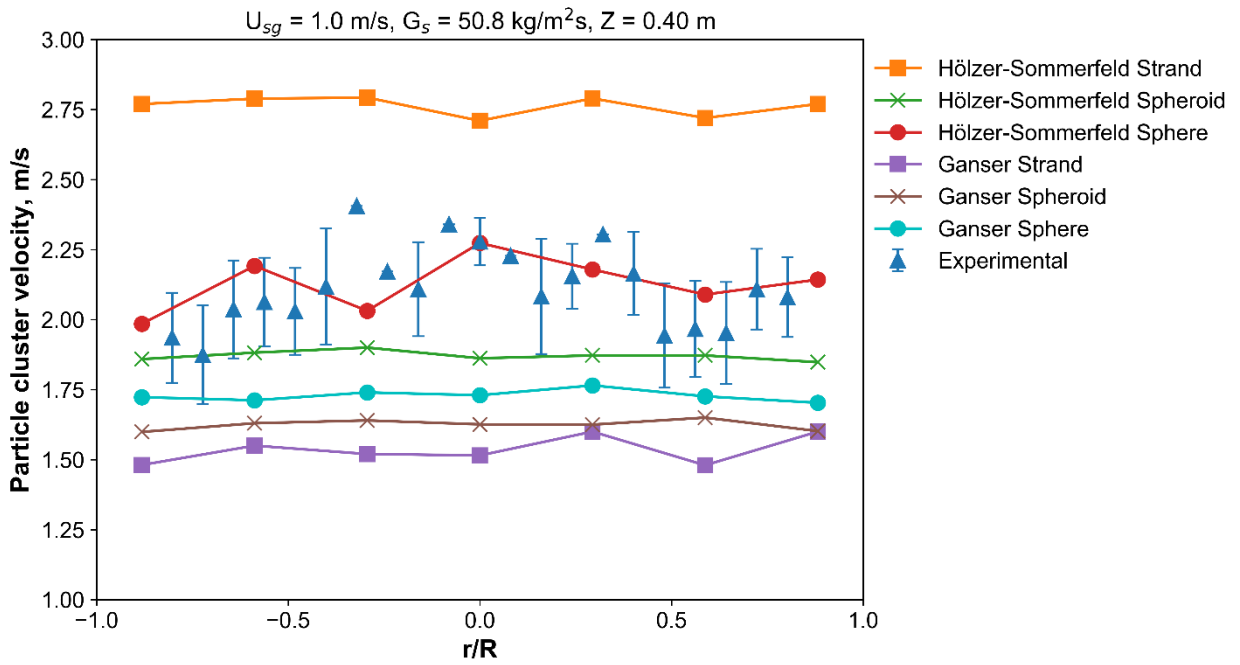
c)
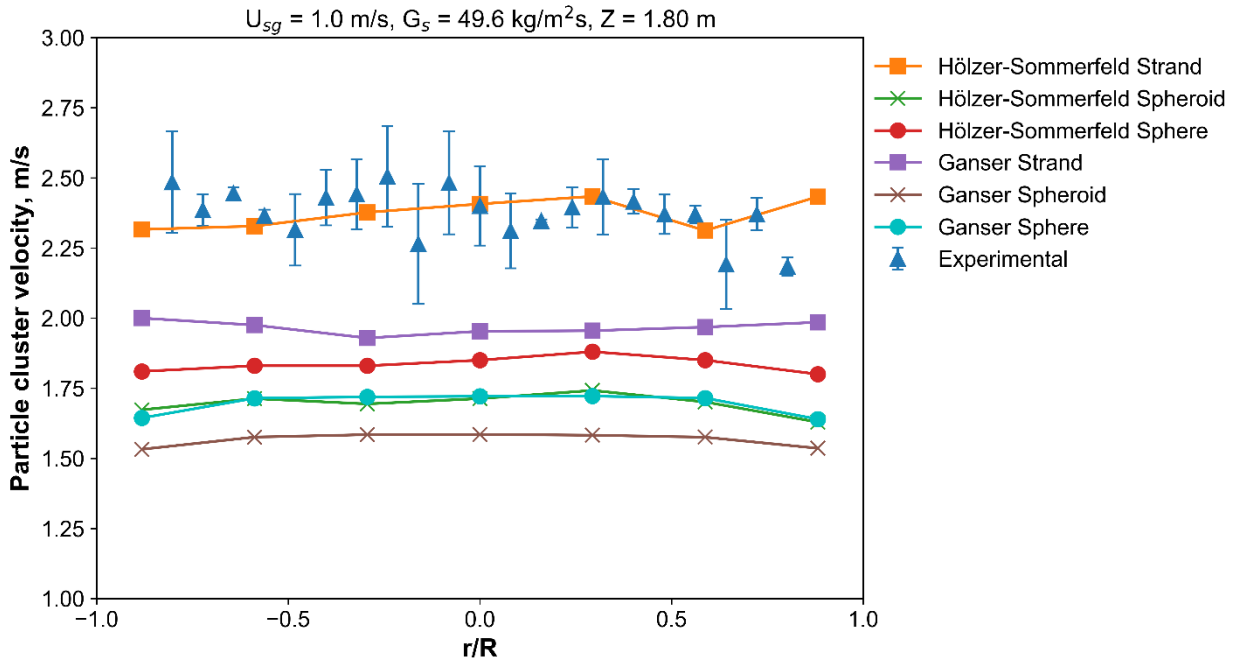
Figure 7.4. Radial Profiles of Particle Cluster Velocities using Hölzer-Sommerfeld and Ganser Drag Configurations at (a) Z = 0.20 m, (b) Z = 0.40 m, and (c) Z = 1.80 m

On this basis, and from the particle cluster velocity radial profiles reported in Figure 7.4, it can be concluded that the Hölzer-Sommerfeld drag correlation provides the best approximation to the experimental results: (a) at the 0.20 m and 0.40 m axial positions when the spherical geometry is selected; and (b) at the 1.80 m axial position when the particle strand is chosen. Therefore, the Hölzer-Sommerfeld drag model is selected for subsequent simulations in the present study, using the spherical or strand geometries given that these particle cluster geometries are relevant for describing the gas-solid flow for the axial positions under consideration.

Table 7.3 reports the operating conditions in terms of U_{sg} and G_s as well as the average axial cluster length and the sphericity parameters as required for the drag model. The spherical shape is assigned to clusters at $Z = 0.20$ m and $Z = 0.40$ m axial positions, while the strand shape is considered for clusters at $Z = 1.80$ m.

Table 7.5. Operating Conditions and Average Cluster Characteristics for all Simulations

Condition	U_{sg} (m/s)	G_s (kg/m² s)	N	$\phi_\parallel$	ϕ	$\phi_\perp$
		Z = 0.2 m from air distributor				
1	1.0	31.4	8.3	0.096	0.163	0.544
2	1.0	50.3	8.7	0.091	0.156	0.544
3	1.6	31.2	6.8	0.122	0.200	0.544
4	1.6	53.7	7.1	0.113	0.187	0.544
		Z = 0.4 m from air distributor				
5	1.0	30.2	5.3	0.139	0.230	0.672
6	1.0	50.8	5.7	0.127	0.214	0.672
7	1.6	30.5	4.6	0.165	0.265	0.673
8	1.6	50.6	4.8	0.156	0.254	0.673
		Z = 1.8 m from air distributor				
9	1.0	31.1	3.9	0.636	0.636	2.487
10	1.0	49.6	4.1	0.627	0.627	2.558
11	1.6	31.0	3.2	0.684	0.684	2.153
12	1.6	52.0	3.3	0.672	0.672	2.230

7.7   Particle Cluster Velocity and Particle Volume Fraction Radial Profiles

The next step in the study was the systematic evaluation of the Hybrid Experimental-Numerical Cluster Model in the acceleration and stabilized sections. To accomplish this, experimental results obtained previously in a cold-model downflow unit and reported in a previous article(Medina-Pedraza and de Lasa 2020) were used. In these experiments, the individual cluster size, the cluster velocity, and the particle volume fraction were

measured with the CREC-GS-Optiprobes. For all cases, the simulation was run for 20 seconds and the results were obtained from the time-averaging of the last five seconds.

The validation of the Hybrid Barracuda Model is achieved as shown in Figures 7.5, 7.6, and 7.7 by comparing the simulation results with the experimental data. With this end in mind, radial particle cluster profiles for both cluster particle velocity and particle volume fraction are reported in the following manuscript sections.

a)
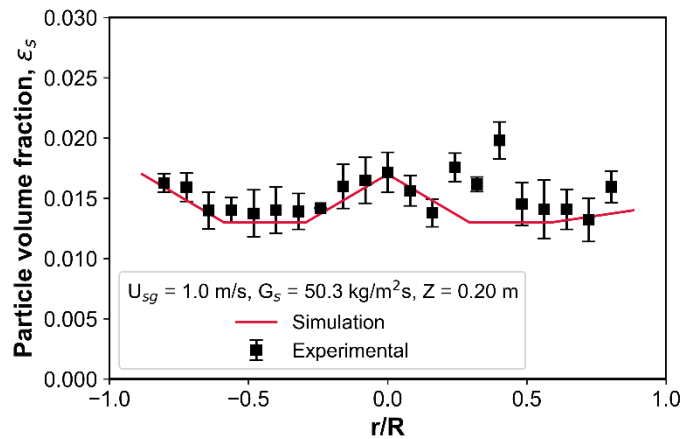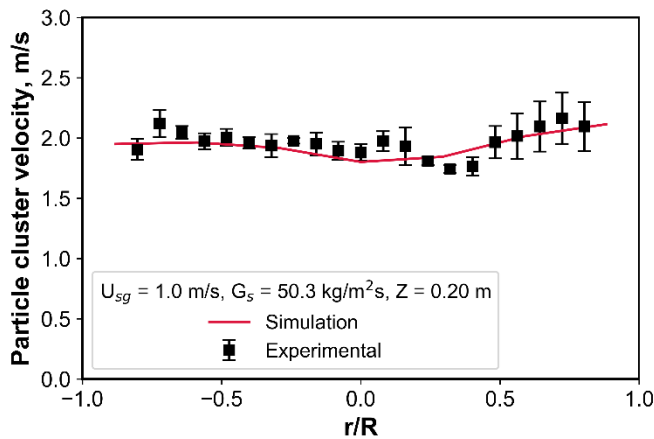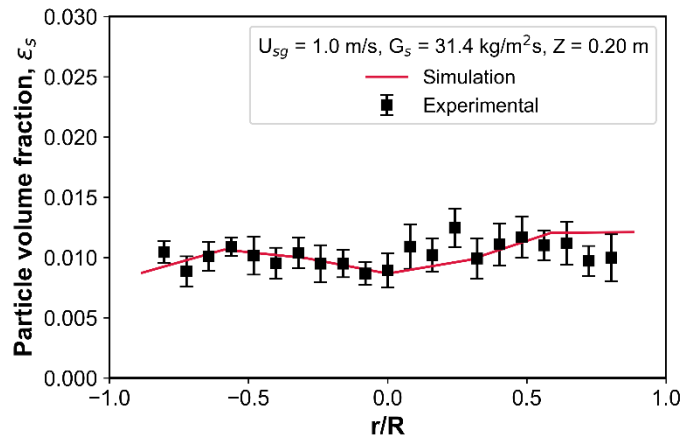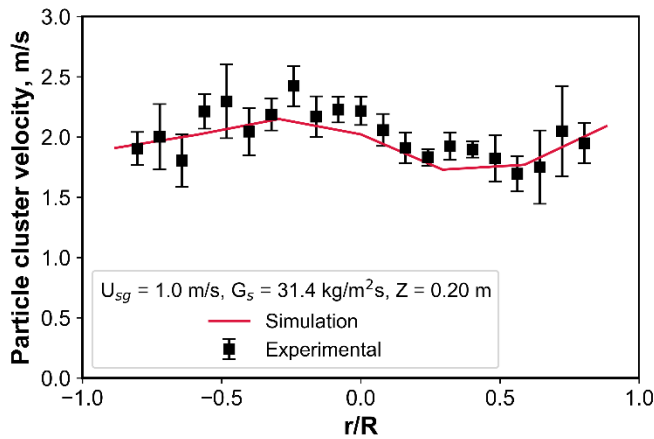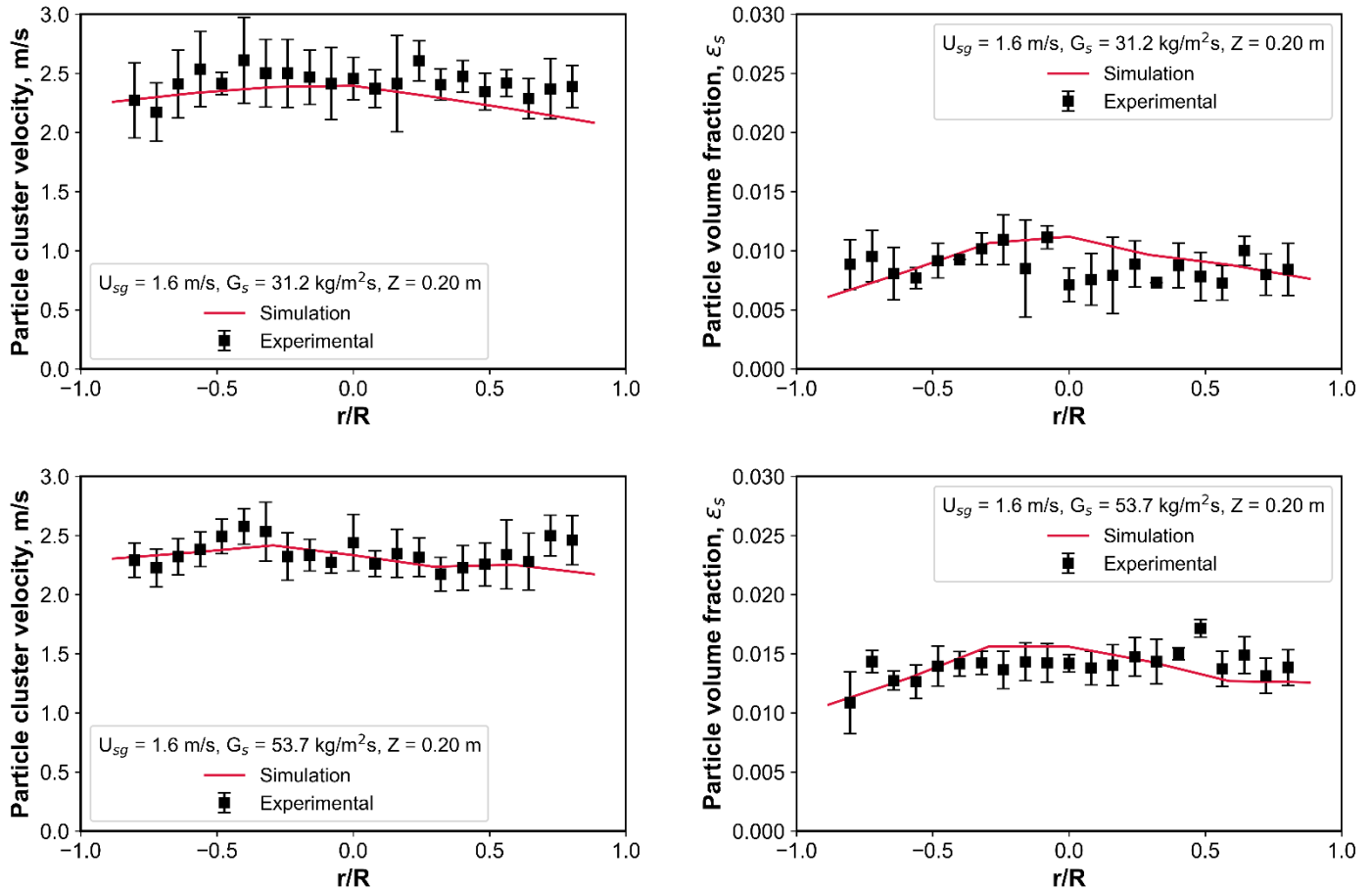
Figure 7.5. Radial Profiles of Cluster Velocities and Particle Volume Fractions at Z = 0.20 m. Particle Cluster Geometry: Spherical Shape.

Figure 7.5 reports cluster particle velocities and particle volumetric fractions for the proposed Hybrid Barracuda simulation using a Hölzer-Sommerfeld Drag Correlation and a spherical cluster geometry. One can see that the particle volume fractions and the cluster particle velocities both display close values in the Hybrid Barracuda simulations as well as in the experimental CREC-Optiprobe data. In addition, an interesting and consistent result which was found as well, was the lack of changes of these particle cluster velocities and particle volumetric fractions with the radial position, remaining at close values, in all cases considered.

Figure 7.6 reports the further validation of the Hybrid Barracuda Model with experimental data at the Z = 0.40 m axial position and several radial downer positions.
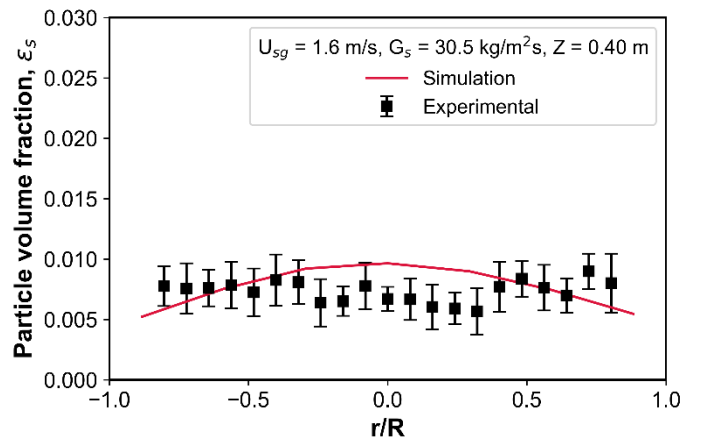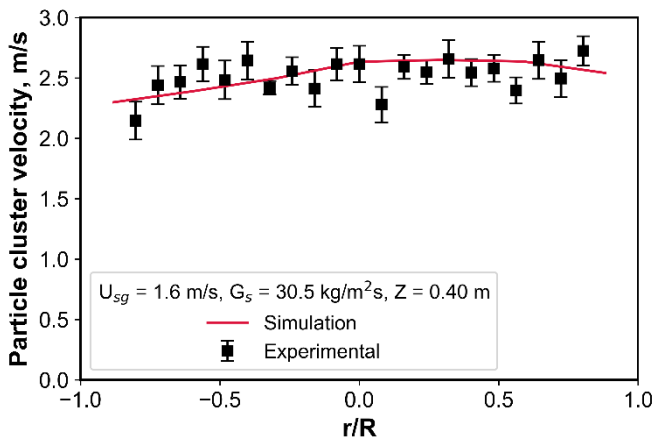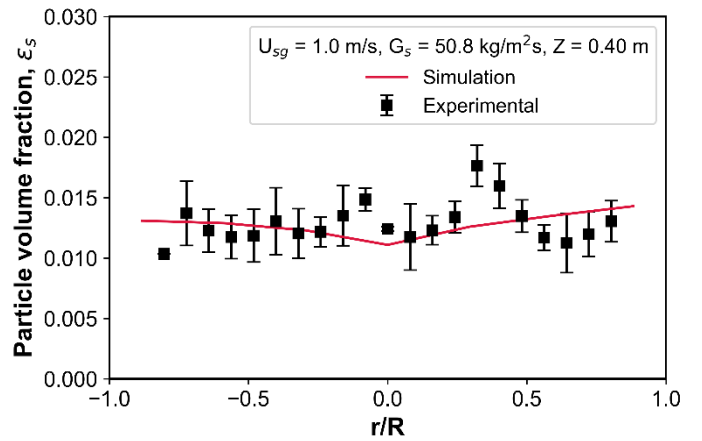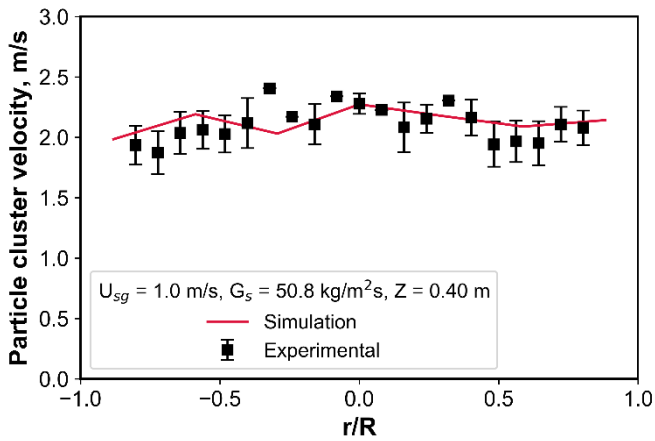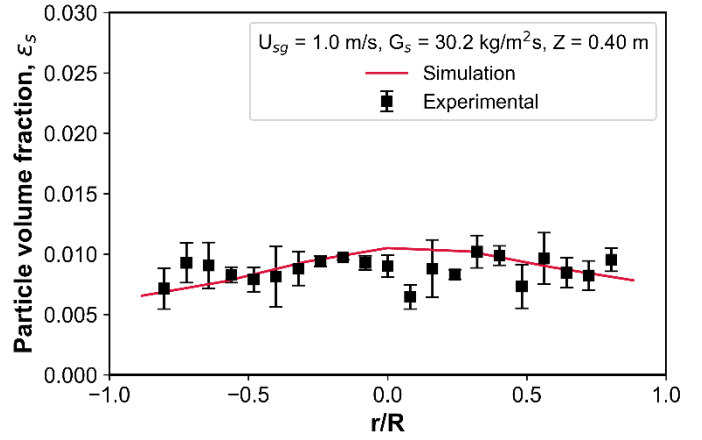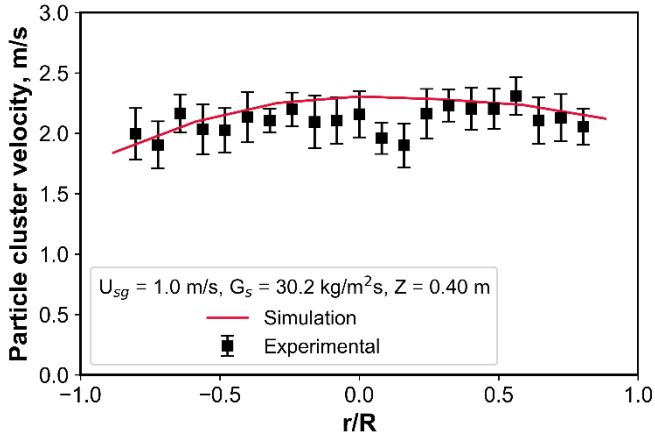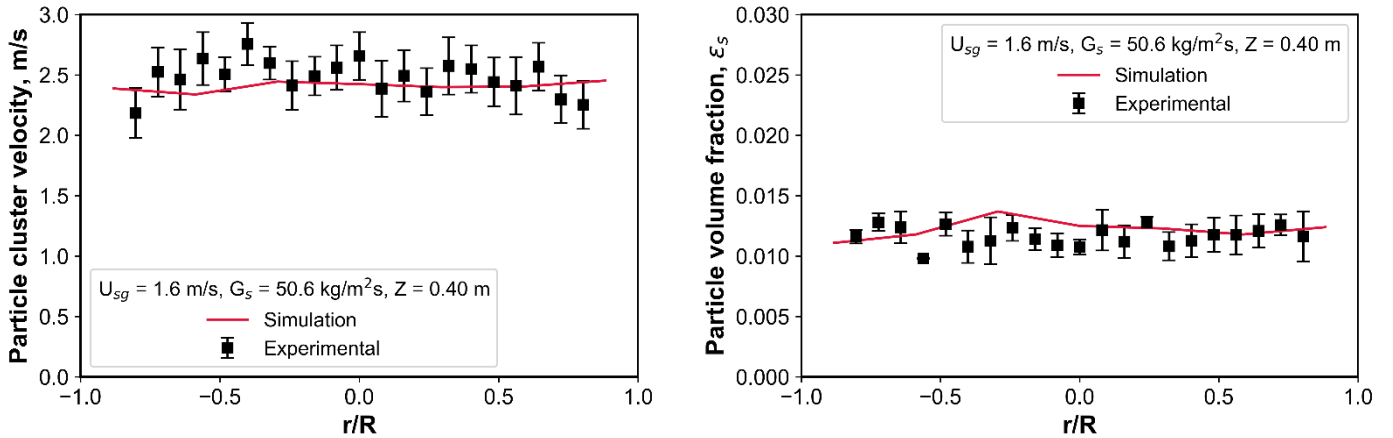
Figure 7.6. Radial Profiles of Cluster Velocities and Particle Volume Fractions at Z = 0.40 m. Particle Cluster Geometry: Spherical Shape.

Figure 7.6 shows as well, the similarity between the Hybrid Barracuda Model simulations and the experimental values at various radial positions, if both the spherical geometry and the Hölzer-Sommerfeld Drag Correlation are selected for fluid dynamic downer studies.

Furthermore, Figure 7.7 revaluates the Hybrid Barracuda Model in the fully developed flow section, at the Z = 1.80 m axial position.
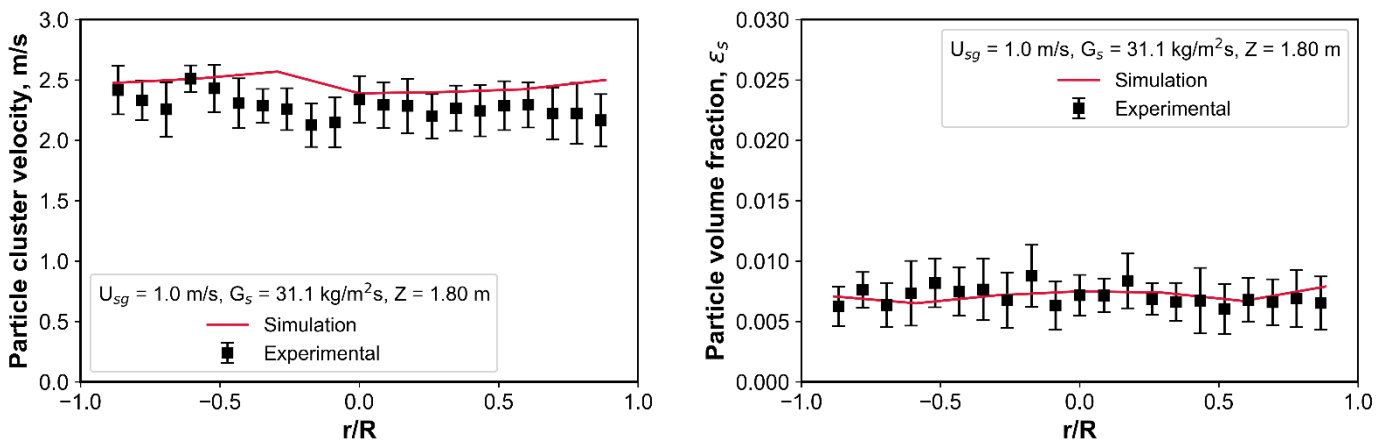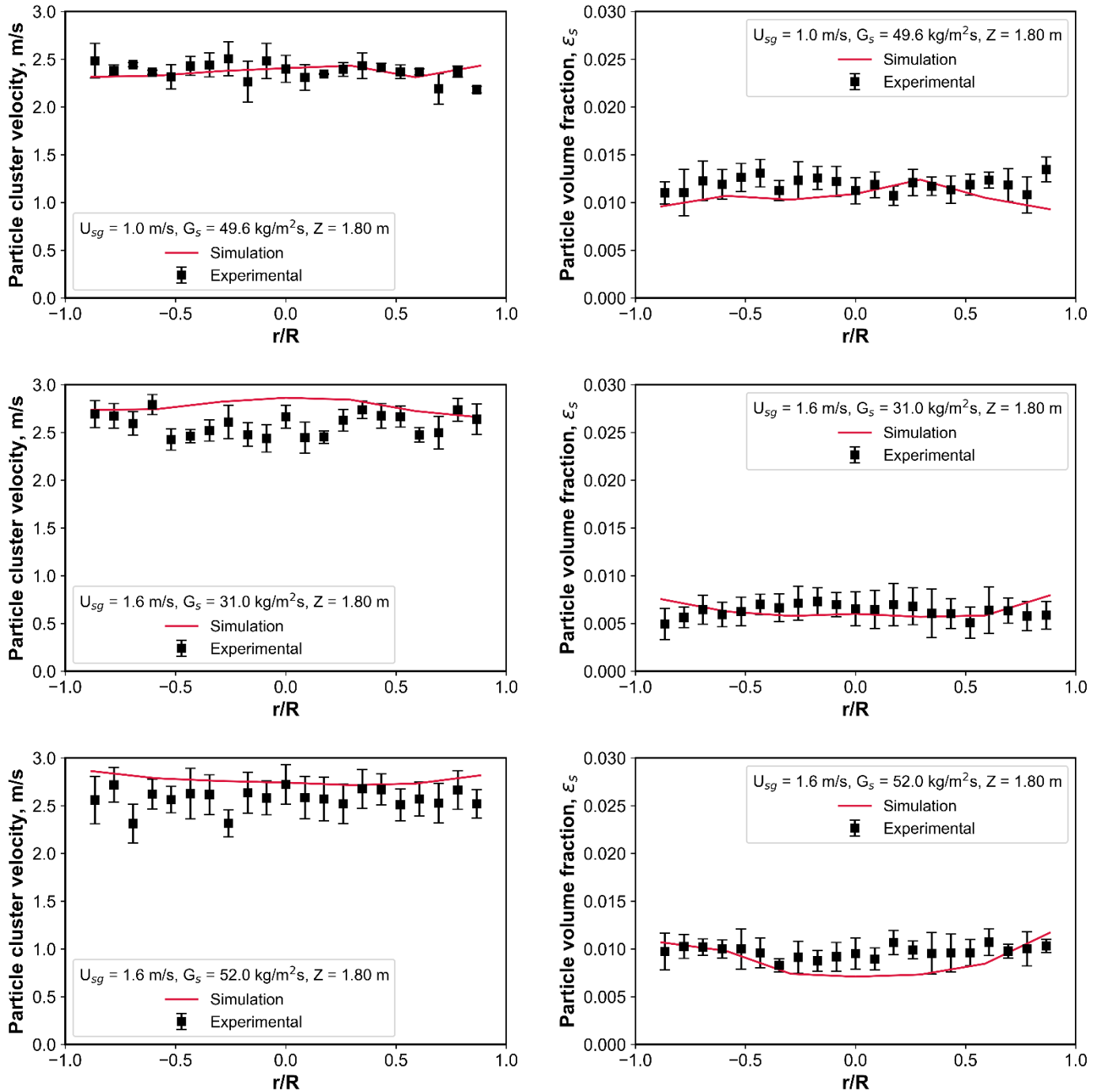
Figure 7.7. Radial Profiles of Cluster Velocities and Particle Volume Fractions at Z = 1.80 m. Particle Cluster Geometry: Strand Shape.

One can thus again observe in Figure 7.7, that the Hybrid Barracuda Model is still quite adequate to represent the relatively uniform radial particle flow (cluster particle velocity and particle volumetric concentration) and this, once the Hölzer-Sommerfeld drag correlation and the strand cluster geometry is selected.

Furthermore, Table 7.4 provides a comprehensive description of the Hybrid Barracuda Model's ability to assess the relatively uniform radial profiles of both particle cluster velocity and particle volumetric concentration.

Table 7.6. Summary of the Radial Averaged Particle Cluster Velocity and Particle Volume Fraction for all Conditions at Three Axial Positions Studied.

Condition	U_{sg} (m/s)	G_s (kg/m² s)	$\bar{u}_{p,exp}$	$\bar{u}_{p,sim}$	$\bar{\varepsilon}_{s,exp}$	$\bar{\varepsilon}_{s,sim}$
			Z = 0.2 m from air distributor			
1	1.0	31.4	2.019	1.956	0.0102	0.0103
2	1.0	50.3	1.963	1.944	0.0153	0.0143
3	1.6	31.2	2.421	2.280	0.0087	0.0089
4	1.6	53.7	2.351	2.297	0.014	0.0135
			Z = 0.4 m from air distributor			
5	1.0	30.2	2.104	2.162	0.0087	0.0087
6	1.0	50.8	2.112	2.128	0.0129	0.0128
7	1.6	30.5	2.519	2.522	0.0073	0.0077
8	1.6	50.6	2.483	2.408	0.0117	0.0122
			Z = 1.8 m from air distributor			
9	1.0	31.1	2.281	2.467	0.0071	0.0072
10	1.0	49.6	2.376	2.372	0.0119	0.0105
11	1.6	31.0	2.586	2.771	0.0063	0.0064
12	1.6	52.0	2.576	2.774	0.0097	0.0089

Table 7.4 shows the consistent closeness of the $\bar{u}_{p,exp}$ and $\bar{u}_{p,sim}$, and the $\bar{\varepsilon}_{s,exp}$ and $\bar{\varepsilon}_{s,sim}$ with limited standard deviations, with this being true for all conditions considered. Thus, one can conclude that in a downer unit simulation the main challenge is to select the proper particle cluster geometry (either spherical or strand) and an appropriate particle drag correlation. This allows one to implement a valuable and applicable hybrid model, such as the one implemented with the Barracuda software in the present study. This can be done successfully in conjunction with the availability of particle cluster size distribution data, obtained with the CREC-Optiprobes.

7.8 Conclusions

a) A hybrid CPFD model which include particle cluster size distributions and particle cluster geometries is validated with experimentally determined cluster particle velocity and particle volume fraction at various radial positions in the downer,

b) An Hölzer-Sommerfeld drag correlation suitable for a wide range of particle cluster configurations either close to spherical in the downer feeding section and of a

strand type in the downer stabilized section, is shown to be adequate while used in conjunction with the hybrid CPFD Model.

8 CPFD Simulation of Fluid Catalytic Cracking of Vacuum Gas Oil in a Downflow Reactor

8.1 Introduction

Fluid catalytic cracking (FCC) is an important part of the modern refinery as it converts heavy gas oil from the atmospheric and vacuum distillation units into higher value products such as gasoline and important precursors for the petrochemical industry. The need to process heavier feedstock while meeting stricter environmental regulations requires innovations in the FCC process. (Jiménez-García, Aguilar-López, and Maya-Yescas 2011)

The downer reactor was initially proposed as an alternative to the riser reactor, as it is designed to improve the gas-solid contact in the FCC process. Hydrodynamic studies have shown uniform radial profiles with a narrow residence time distribution, a behaviour that is close to ideal plug-flow. Several evaluations, ranging from laboratory to demonstration scale, have shown the possible applicability of the downer reactor in the FCC process, given that it increases the gas oil conversion and improves selectivity towards gasoline and light olefins (Parthasarathi and Alabduljabbar 2014). Catalyst particles in the downer tend to aggregate by forming several particle clusters, which affect particle velocity and residence time. Thus, a comprehensive study of the downer unit and its application to the FCC process is needed for its successful implementation.

The FCC process uses catalysts with a typical particle diameter of 60 μm. These particles contain 25-30 wt% of H-USY zeolite crystallites supported by an amorphous matrix. Catalyst activity and selectivity can be improved by modifying the zeolite crystallite size, given that this reduces the intracrystalline diffusional transport rate limitation constraints inside the FCC catalyst (Al-Sabawi, Atias, and de Lasa 2006).

Catalytic cracking reactions of gas oil molecules take place in several steps, which strongly depend on the zeolite crystallite size. After hydrocarbon diffusion through the outer matrix mesopores, reactant molecules are transported further through the zeolite pore structure to reach the active sites in the crystallites, where they adsorb first and crack

later. Smaller crystallite zeolites provide easier access to the active sites, promoting a higher gas oil conversion (Al-Sabawi, Atias, and de Lasa 2006).

A kinetic model for the catalytic cracking of gas oil is required for the description of FCC reactions in the downer unit. Since the VGO (vacuum gas oil) feedstock and the products in FCC are composed of many different compounds and given that a significant number of reactions happen simultaneously during catalytic cracking, an effective strategy for the kinetics of the FCC process is the 'lumping' approach. This kinetic model uses several constituent groups designated as "lumps", with the chemical species included in every pseudo-species group, sharing similar properties, such as boiling points (Ancheyta-Juárez et al. 1997).

The process of scaling-up a fluidized bed reactor, such as the riser or the downer unit, is not trivial, since the behaviour of the two phases at different scales is difficult to predict, and the associated diffusional processes are scale-dependant.

A typical development process of new technology involves the testing at the pilot scale before moving to the demonstration scale. CFD modelling is an efficient way of describing the behaviour of a gas-solid reacting system and is an important tool in the planning of the scale-up of a reactor without building a new unit for each scenario, saving costs and time.

Gas-solid flows can be modelled in CFD in two main ways, as a continuous or discrete phase, with this depending on how the solid phase is treated. Two-Fluid Models (TFM), which treat both phases as a continuum, are capable of solving a system with many particles in a time-effective manner. However, TFM lacks the accuracy of methods that track particles with more detail.

A typical FCC unit has many billions or even trillions of particles circulating. Thus, an accurate model that calculates the trajectory of each particle would lead to prohibitive computational times. The Multiphase-Particle in Cell Method (MP-PIC), which uses groups of particles or clouds for the calculations, allows for the Lagrangian tracking of the solid phase while saving computational resources (Snider 2001).

While there are several CFD studies of catalytic cracking in riser reactors that use TFM and MP-PIC as reported in the literature (Berrouk et al. 2017), very few deal with downer reactors. This study is the first attempt, to the extent of the authors' knowledge, where a catalytic cracking reaction is simulated with an MP-PIC Model in a downer reactor unit, using an experimentally obtained cluster size distribution as a key parameter for the simulation.

8.2   Kinetic Model

The FCC simulation of the downer unit of the present study uses a five-lump kinetic Model involving gasoil (VGO), light cycle oil, gasoline, light gases, and coke as pseudo-components. The reaction scheme is presented in Figure 8.1.
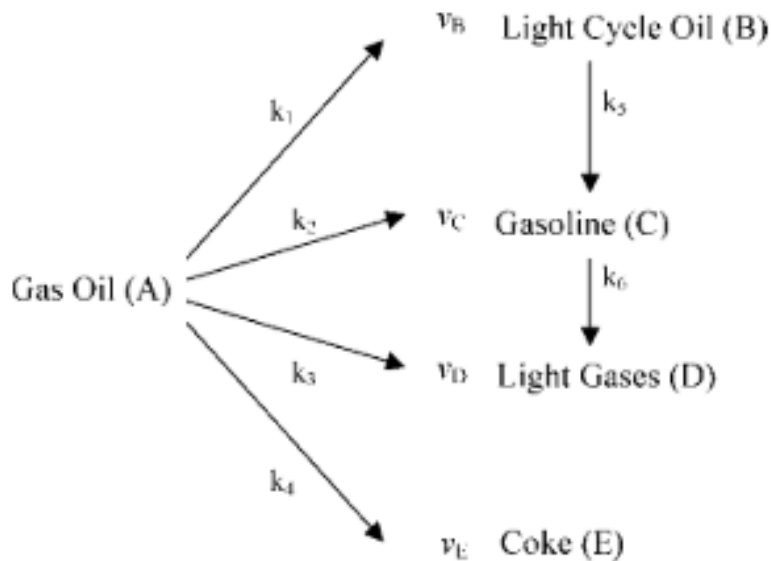
Figure 8.1 Five-Lump Reaction Scheme (Al-Sabawi, Atias, and de Lasa 2006)

Where k_1, k_2, k_3, k_4, k_5 and k_6 are the kinetic constants and v_B, v_C, v_D and v_E represent the stoichiometric coefficients of the products.

Species balances for the selected five pseudo-species lumps can be represented by the following equations:

$$VGO\ (A) \qquad -\frac{V}{W_{cr}}\frac{dC_A}{dt} = n_{ss}\varphi_{int}(k_1 + k_2 + k_3 + k_4)C_A^2 \qquad\qquad (8-1)$$

$$Light\ Cycle\ Oil\ (B) \qquad \frac{V}{W_{cr}}\frac{dC_B}{dt} = \varphi_{int}(v_B n_{ss} k_1 C_A^2 - k_5 C_B) \qquad (8-2)$$

$$Gasoline\ (C) \qquad \frac{V}{W_{cr}}\frac{dC_C}{dt} = \varphi_{int}\left(v_C n_{ss} k_2 C_A^2 + \frac{v_C}{v_B}k_5 C_B - k_6 C_C\right) \qquad (8-3)$$

$$Light\ Gases\ (D) \qquad \frac{V}{W_{cr}}\frac{dC_D}{dt} = \varphi_{int}\left(v_D n_{ss} k_3 C_A^2 + \frac{v_D}{v_C}k_6 C_C\right) \qquad (8-4)$$

$$Coke\ (E\ ) \qquad \frac{dX_E}{dt} = \varphi_{int}(v_E n_{ss} MW_E C_A^2) \qquad (8-5)$$

Where C_A, C_B, C_C, C_D, are the concentrations of gas oil, light cycle oil, gasoline, and light gases, respectively; X_E is the mass fraction of coke per mass of catalyst; V is the reactor volume, $5.5 \times 10^{-5}\ m^3$; W_{cr} is the catalyst mass in kg; t is the reaction time.

As the reaction progresses, the coke deposits on the catalyst surface, decreasing its activity by covering the active sites. The catalyst activity decay function, φ_{int}, can be used to relate catalyst activity to the coke concentration on the catalyst. It is calculated with the expression below:

$$\varphi_{int} = \exp(-\lambda X_E') \qquad (8-6)$$

where λ is the deactivation parameter for gas oil cracking and X_E' is the mass of coke produced per mass of gas oil injected. The values for the various constants used in this study were obtained in the CREC Riser Simulator, which is a laboratory-scale fluidized batch reactor. Additional details about the kinetic model and the experiments can be found in Al-Sabawi and de Lasa. (Al-Sabawi, Atias, and de Lasa 2006; Al-Sabawi, Atias, and De Lasa 2008)

One should note as well that Eqs. 8-1 to 8-5 include a n_{ss}, which is an effectiveness factor parameter, which can be approximated to the value of one, for 0.4 μm size zeolites dispersed in the 60-μm FCC catalyst of the present study (Al-Sabawi, Atias, and de Lasa 2006; Al-Sabawi, Atias, and De Lasa 2008). Thus, the kinetic parameters for a catalyst with crystallites of a 0.4 μm diameter, as reported in Table 8.1, can be used.

Table 8.1. Intrinsic Kinetic Parameters for Gas Oil Catalytic Conversion

Parameter	Value
n_{ss}	1
$k_{10} \left(\dfrac{m^6}{kg_{crystallite}\ mol_{gasoil}\ s} \right)$	1.158E-02
$E_{10} \left(\dfrac{kJ}{mol} \right)$	97.01
$k_{20} \left(\dfrac{m^6}{kg_{crystallite}\ mol_{gasoil}\ s} \right)$	5.036E-03
$E_{20} \left(\dfrac{kJ}{mol} \right)$	120.61
$k_{30} \left(\dfrac{m^6}{kg_{crystallite}\ mol_{gasoil}\ s} \right)$	4.058E-03
$E_{30} \left(\dfrac{kJ}{mol} \right)$	136.17
$k_{40} \left(\dfrac{m^6}{kg_{crystallite}\ mol_{gasoil}\ s} \right)$	1.49E-03
$E_{40} \left(\dfrac{kJ}{mol} \right)$	139.65
$k_{50} \left(\dfrac{m^3}{kg_{crystallite}\ mol_{gasoil}\ s} \right)$	7.602E-02
$E_{50} \left(\dfrac{kJ}{mol} \right)$	90.43
$k_{60} \left(\dfrac{m^3}{kg_{crystallite}\ mol_{gasoil}\ s} \right)$	4.705E-02
$E_{60} \left(\dfrac{kJ}{mol} \right)$	82.86
λ	26.10

8.3 CPFD Simulation Parameters

The downer reactor geometry used for the simulations in the present study is composed of (a) a cyclone feeder which feeds the reactor with the catalyst coming from the catalyst regenerator, (b) an entry Venturi feeder section, and (c) a downer column section where the reaction takes place quite rapidly. The downer column has a diameter of 0.15 m and a height of 15 m. The downer reactor is shown in Figure 8.2.
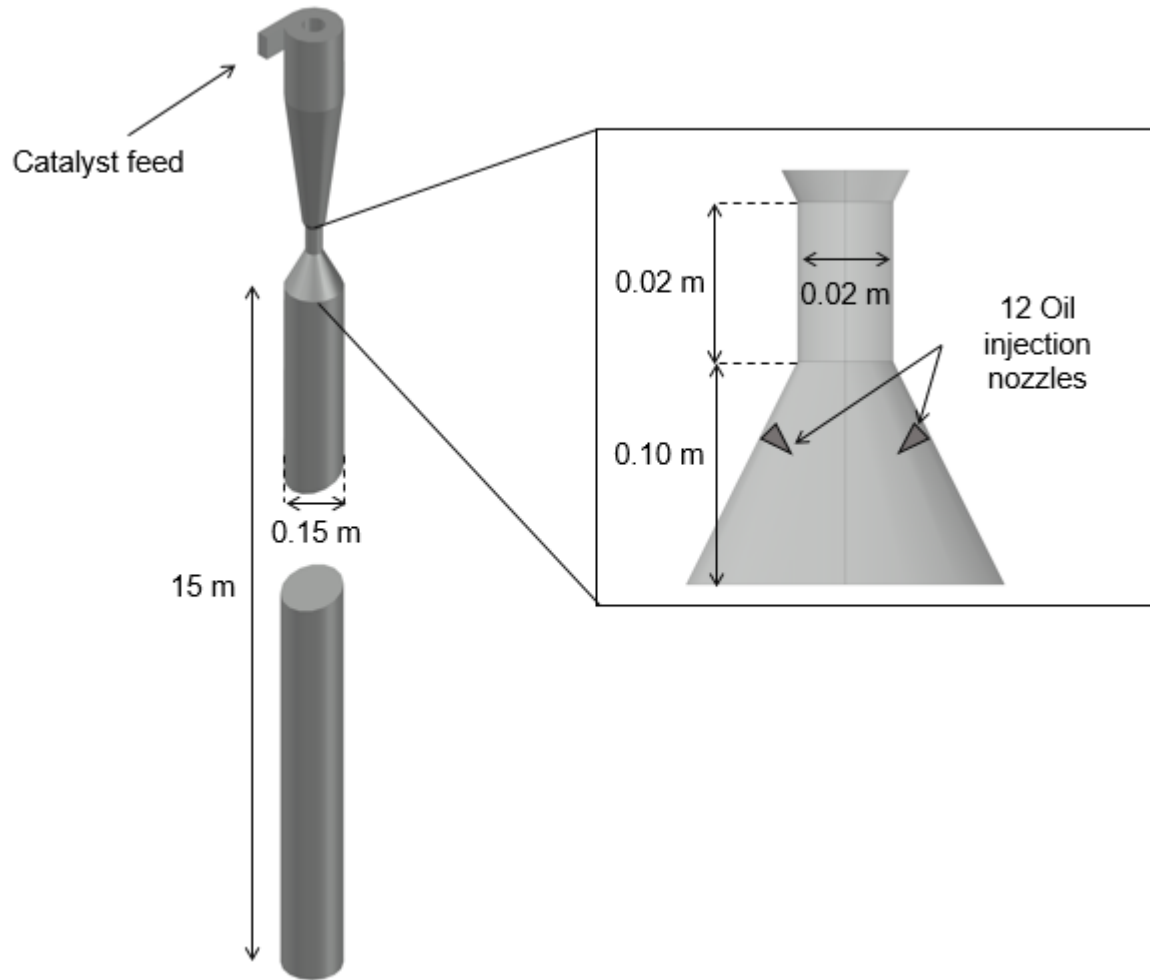
Figure 8.2. Downer Reactor Used in the Simulations

The VGO is injected into the downer unit through 12 nozzles with a diameter of 2 mm each, equally spaced around the perimeter below the Venturi feeder.

To proceed with the CPFD simulations, an Eulerian grid was used. It was composed of 57,000 cells, with their dimensions being reported in Table 2.

Table 8.2. Cell Dimensions for CPFD Simulations

Direction	Length (m)
Δx	0.0136
Δy	0.0160
Δz	0.0230

Furthermore, the specific operating conditions (steam flow rate, catalyst flow rate selected) in the FCC unit simulation are reported in Table 8.3.

Table 8.3. Simulation Conditions

Parameter	Value
Stream From Cyclone	
Steam Flow Rate (kg/s)	0.001
Catalyst Flow Rate (kg/s)	0.275 given a C/O = 5
	0.33 given a C/O = 6
	0.385 given a C/O = 7
	(initial 0.1 % of coke)
Temperature (°C)	690
Pressure (Pa)	150000
Stream From Injection Ports	
VGO Flow Rate (kg/s)	0.055
Steam Flow Rate (kg/s)	0.003
Temperature (°C)	230

Regarding the agglomerate particle sizes for the simulations, one should mention that cluster sizes display a skewed distribution as reported in Section 5.1. For the simulations, and based on the operating condition, the cluster size distribution is the one considered in Figure 8.3.
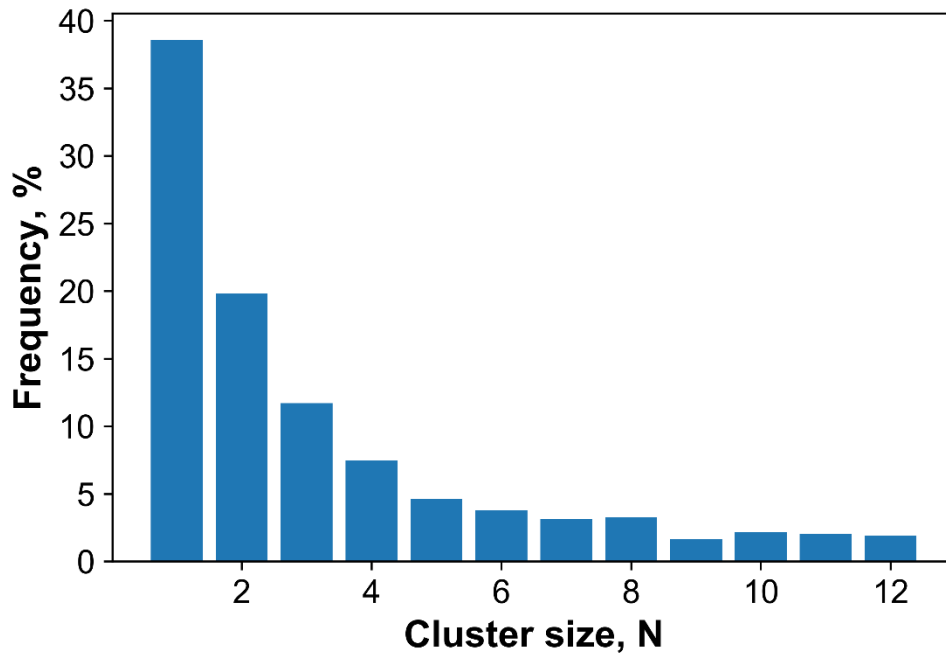
Figure 8.3. Cluster Size Distribution Used in FCC Simulations as Reported in Section 5.1 for Gs=30 Kg/m2 s and Ug= 1.6 m/s

8.4 Results and Discussion

On this basis, and to develop various simulations, the catalyst-to-oil ratio (C/O) was set at 5, 6, and 7. This was done to evaluate the influence of this key C/O parameter on gas oil conversion, product selectivity, and gas-solid mixing in the downer feeder.

Figures 8.4 (a) and (b) report the CPFD simulation results for the Catalyst/Oil (C/O) ratio of 5. Figure 8.4a shows the downer gas-solid fluid dynamics using axial and radial downer cluster velocity and particle volume fraction profiles. In particular, Figure 8.4a shows particle cluster velocity radial profiles at six axial positions, downwards from the injection ports: 0.5 m, 1 m, 5 m, 9 m, 13 m, and 14.8 m. It can be observed that both radial and axial particle velocity profiles are quite uniform, with a consistent increase of cluster velocity in the near to wall region. This finding is consistent with a progressive increase of the particle cluster velocity, given the steady increase of the total molar flows and the total volumetric gas flows, with the catalytic cracking extent of reaction.

a)   b)
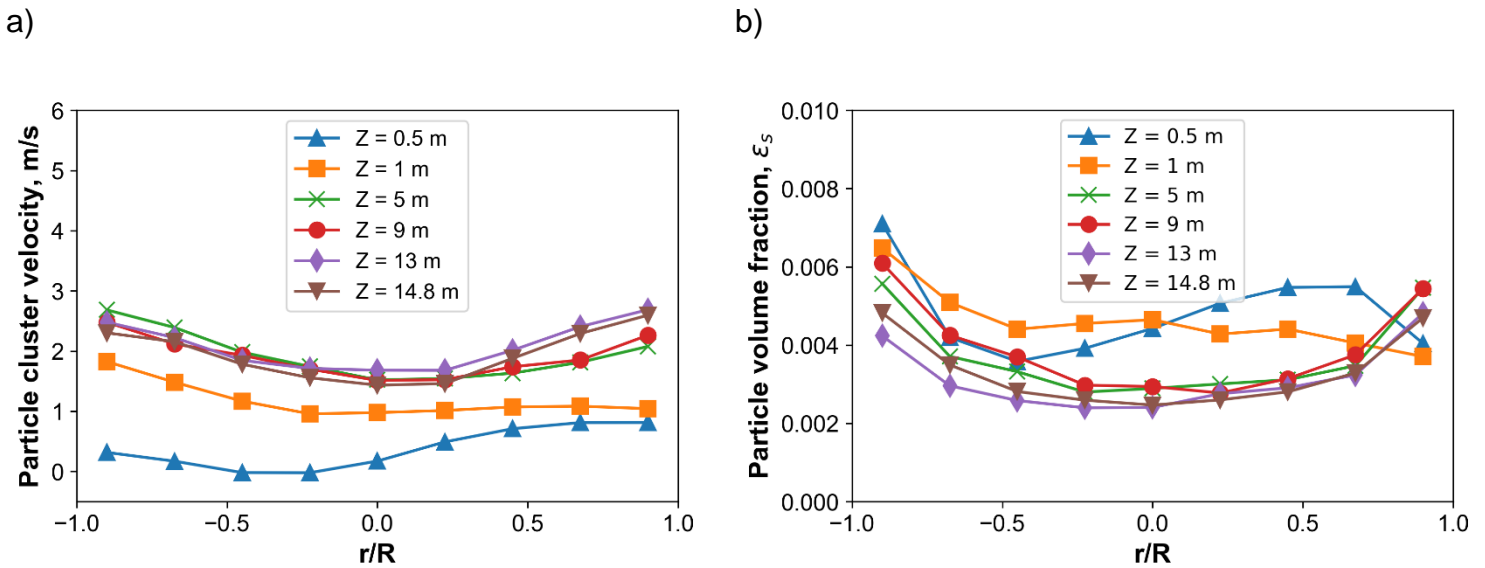
Figure 8.4 Results for C/O = 5, a) particle cluster velocity, b) particle volume fraction

Furthermore, Figure 8.4b reports the particle volume fraction radial profiles at the same 0.5m, 1m, 5m, 9m, 13m, and 14.8m axial positions, showing a particle volume fraction consistently augmenting near the wall. This behaviour is similar to those of previous

107

studies with downers of a diameter greater than 0.1 m, as reported by Zhu et al. (J. X. Zhu et al. 1995).

Turning our attention to the mass fractions of the various chemical species (lumps), Figure 8.5 depicts the mass fractions for various hydrocarbon gaseous components along the downer axis. As expected, the gas oil mass fraction decreases along the axial downer length, with the light cycle oil mass fraction always being higher than those of gasoline and light gases. One can thus see that in a downer with a 6.47 s average particle residence time, a 42.5 wt% overall VGO oil conversion is achieved.
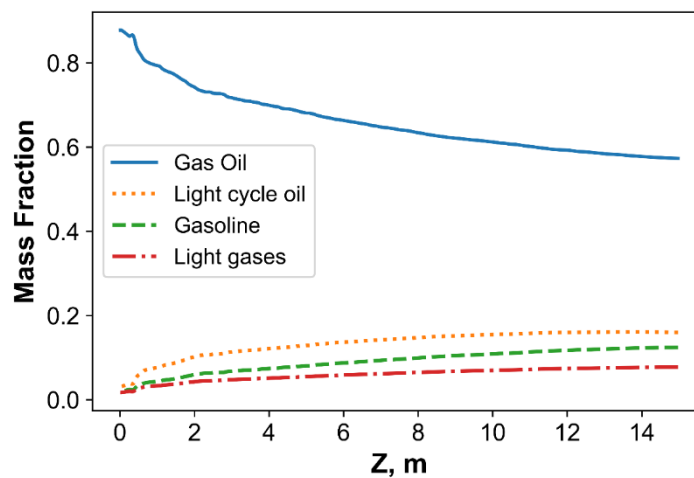
Figure 8.5 Results for C/O = 5. Mass fraction of gaseous reaction components along the downer

Figure 8.6a further describes the axial and radial fluid and particle temperature profiles at three radial positions. This was done for the entire 15m downer length. As well, Figure 8.6b reports an expanded view of the first meter downwards from the VGO injection feeding level. On the basis of these data, one can conclude that thermal equilibrium between the flowing phases is reached within 0.4-m from the downer injection port, with mixed phases reaching the 520 °C thermal level at 1m from the downer injection port. Following this, and once thermal equilibrium was achieved, one could observe a justifiable progressive temperature decrease for both gas and solid phases. This was the case, given the endothermic nature of the cracking reaction.

a)
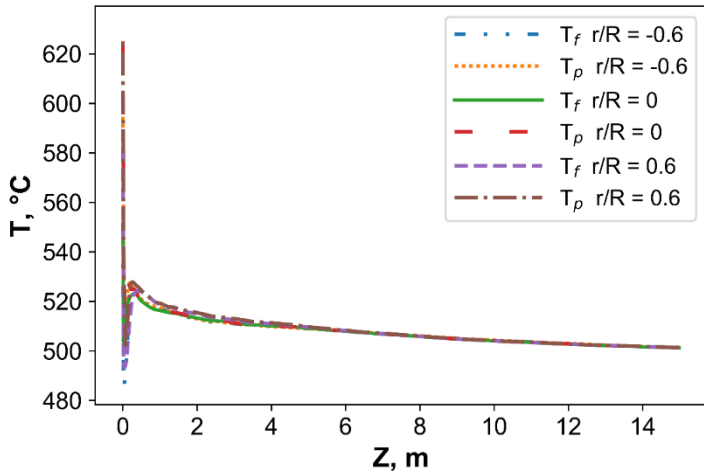
b)
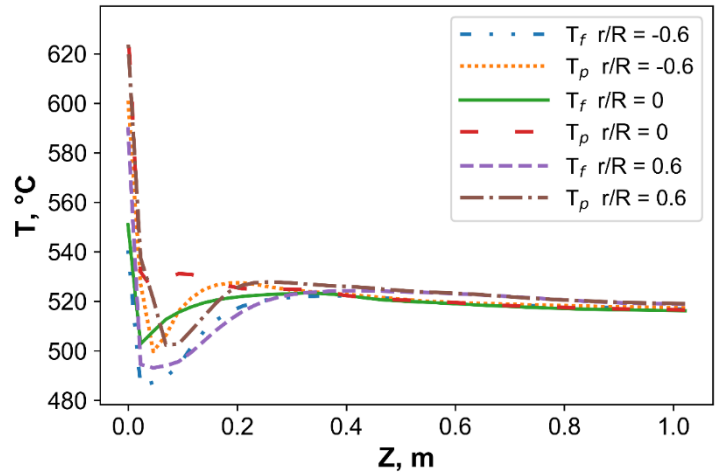
Figure 8.6. Results for C/O = 5. Axial Temperature profiles for: a) full length of downer, b) one meter from the feeding point

Figure 8.7 (a) and (b) further report the results of the catalyst particle fluid dynamic behaviour at a C/O of 6. Figure 8.7a shows the radial profiles of the cluster velocity, at six axial positions, from the VGO injection ports level with these being 0.5m, 1m, 5m, 9m, 13m, and 14.8m.

a)
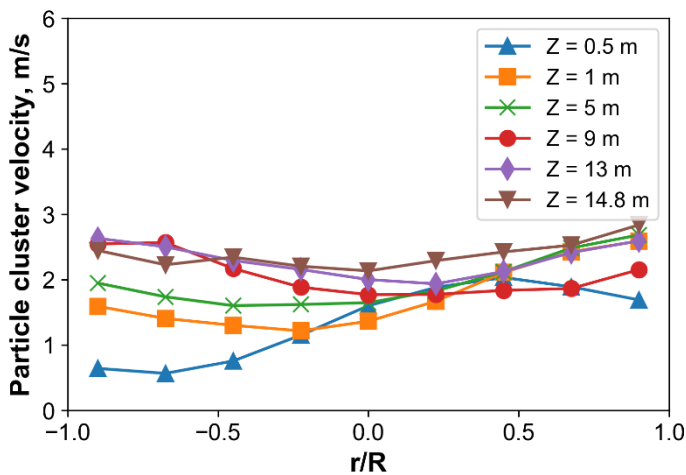
b)
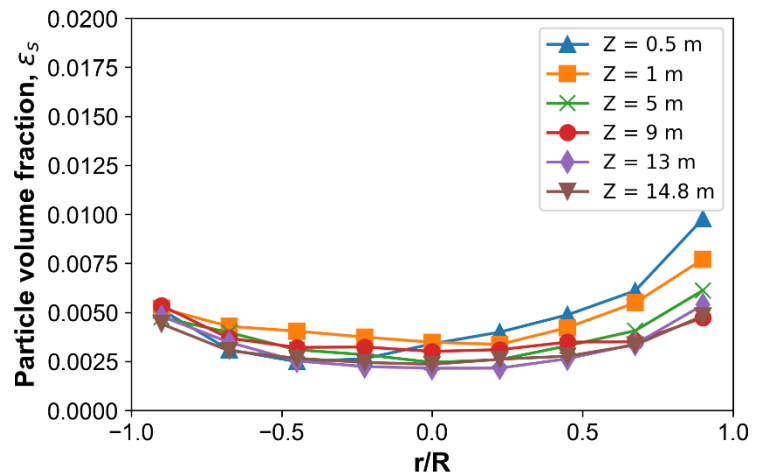
Figure 8.7. Results for a C/O = 6: a) particle cluster velocity, and b) particle volume fraction.

109

It can be observed that at 1 m downwards from the VGO injection port, the radial particle velocity profiles are fully developed already. In fact, at 1 m, particle velocity profiles already displayed steady radial distributions, essentially unchanged at lower heights in the downer. Once again, and consistent with all the calculated particle velocities, for a C/O of 5 and after 5 m, these particle velocities were consistently higher near the wall region.

Figure 8.7b describes the cluster particle volume fractions at 0.5 m, 1 m, 5 m, 9 m, 13 m, and 14.8m and various radial positions for the C/O of 6. In particular, the data for the 0.5 m level shows a somewhat less uniform radial profile, with the particle volume fraction consistently increasing near the wall.

Figure 8.8 shows the mass fractions of the various species lumps, along axial positions in the downer. Results obtained for the C/O of 6 displayed a justifiable steeper decrease of the gas oil mass fractions. This was the case while compared to the C/O ratio of 5. This was a sound result, given the dependence of the changes of A species (VGO) concentrations with reaction time, and with increased catalyst density per unit reactor volume, as anticipated by Eq. (1). Consistent with this, the gas oil conversion increased from 42.5% for a C/O of 5 to 49.8 % for a C/O of 6. On the other hand, the selectivity to gasoline now also augmented, with gasoline and light cycle oil mass fractions being comparable to each other. Thus, one can conclude that increasing the C/O from 5 to 6, leads to higher VGO conversions and better selectivities towards the gasoline desired lump product.
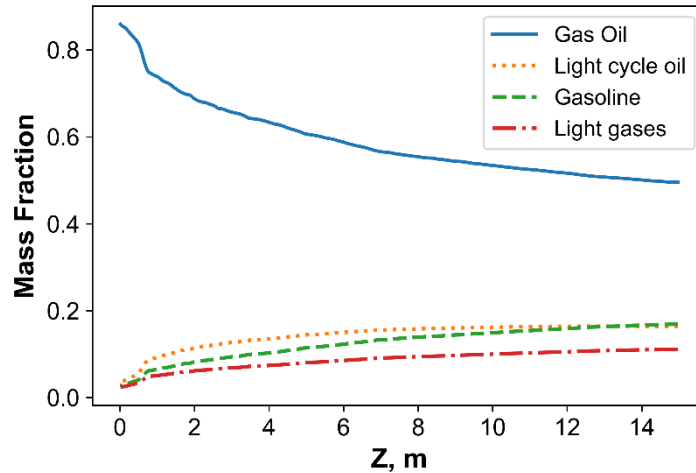
Figure 8.8. Results for C/O = 6. Mass fractions of gaseous reaction components.

Figure 8.9a reports the axial and radial fluid and particle temperature profiles for the full downer length, for the C/O of 6 at three radial positions. Figure 8.9b shows an expanded view of the first meter of the downer from the VGO injection port level. One can observe that the simulated temperature profiles show that thermal equilibrium is reached after a 0.8m downer length, with this distance being longer than the one for the C/O of 5. This is most likely caused by the higher amount of hot catalyst flow being mixed with a steady steam-gas oil stream.

a)
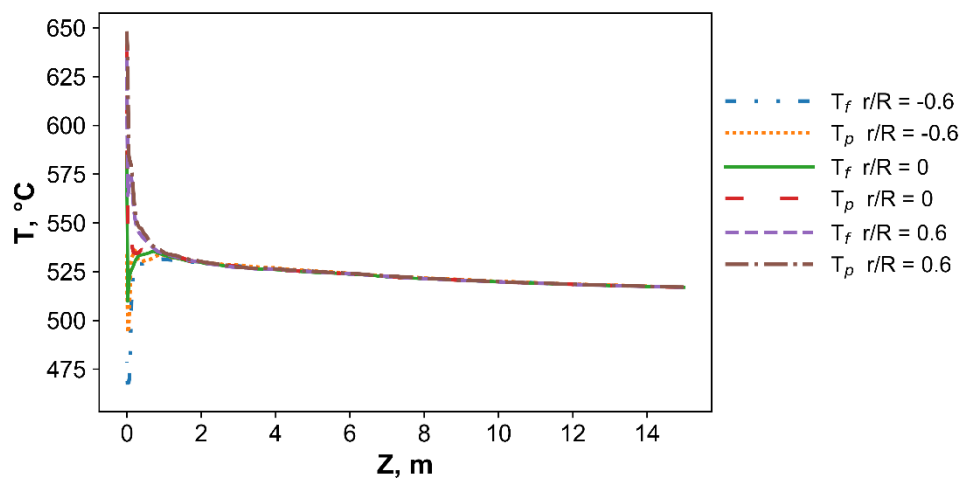
b)
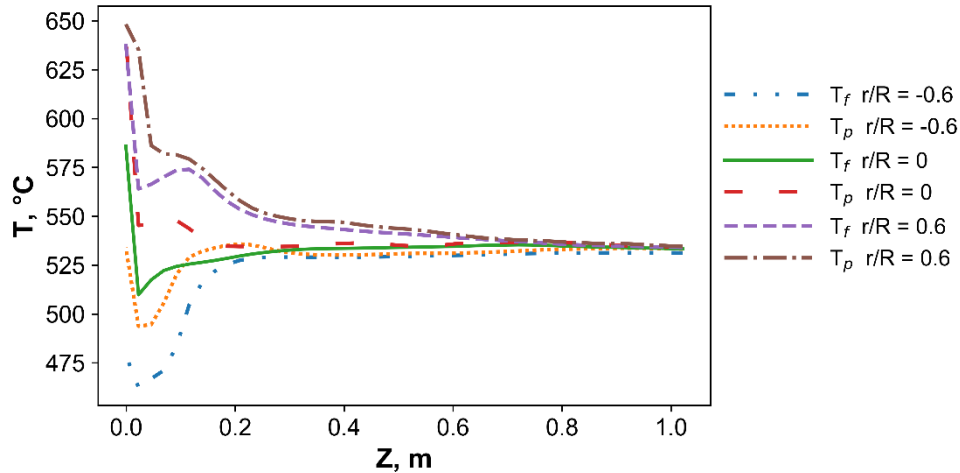
Figure 8.9. Results for C/O = 6 Axial Temperature Profiles for a) full length of downer, b) one meter below the injection

On this basis, it can thus be shown, that it takes at least a one-meter downer length, for the temperatures of the lumped chemical species and those of the catalyst to become similar, reaching approximately a 530 °C mixing temperature. Furthermore, and as in the case of the C/O of 5, once the 1m downer length is attained, both gas and solid temperatures, being always very similar, decrease further along the downer axial positions, with this being consistent with the endothermic nature of the cracking reaction.

Furthermore, Figures 8.10 (a) and (b) show the particle fluid dynamics CPFD simulation results for the C/O of 7. Figure 8.10a reports the particle cluster velocity radial profiles at 0.5 m, 1 m, 5 m, 9 m, 13 m, and 14.8 m axial positions. One can see that at the 0.5 m, the particle clusters have not reached the cluster terminal velocity yet, with this flow stabilization attained after the 5m length.

Figure 8.10b displays the particle volume fractions radial profiles for C/O of 7. Once again, the particle volume fractions at 0.5 m are higher at the near wall region than it is when compared to the other axial positions, indicating that the flow is not fully developed yet.
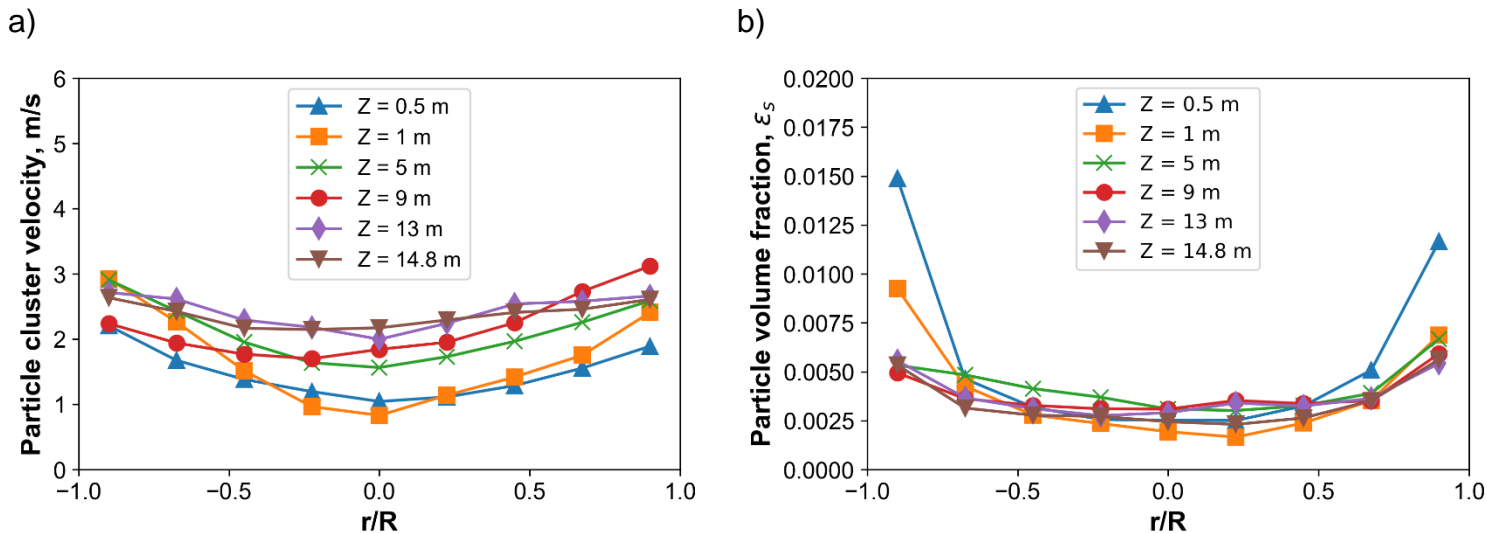
Figure 8.10. Results for C/O = 7; a) particle cluster velocity, b) particle volume fraction.

Figure 8.11 shows the axial mass fractions of various gas chemical species lumps for a C/O of 7. In this case, the overall gas oil conversion reached 56.17 % at the 15 m downer outlet with this being higher than the 42.5% and the 49.8% obtained for the C/Os of 5 and 6, respectively. As well, the gasoline lump mass fractions at the outlet, became higher than those for the lower C/Os of 5 and 6, showing a higher gasoline selectivity.
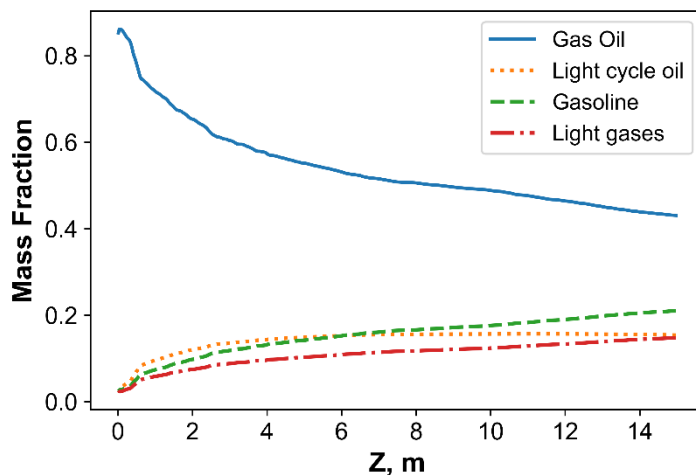
Figure 8.11. Results for a C/O = 7, Mass Fraction of Gaseous Reaction Components

Finally, Figures 8.12 (a) and (b) describe the axial and radial variations of gas and solid temperatures for the C/O of 7, showing the axial temperature stabilization, at a 2m downer axial position.

a)
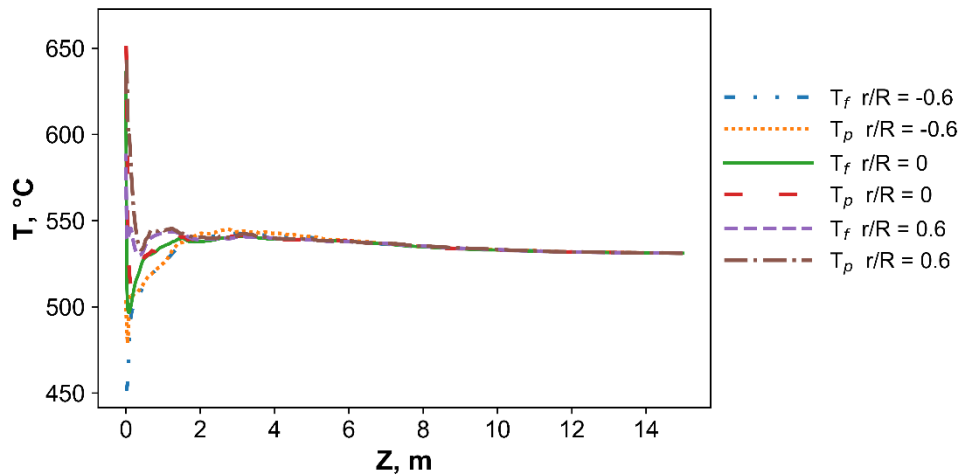
b)
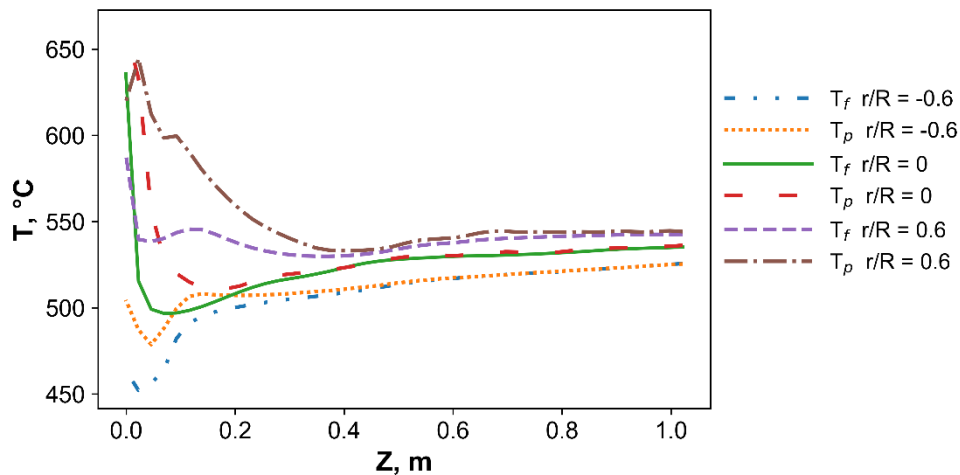
Figure 8.12. Results for a C/O = 7, Axial Temperature Profiles for a) the full length of downer, b) one meter below the injection port

Regarding the coke-on-catalyst or "E" lump in Figure 8.1, one should mention that coke deposits progressively on the catalyst surface as the reaction progresses, reducing

114

catalyst activity. Figure 8.13 displays the average percentage of coke on a weight fraction basis, or weight of coke per unit catalyst weight. This information is provided at five axial positions in the downer and for three C/O ratios: C/O=5, C/O=6, and C/O=7.
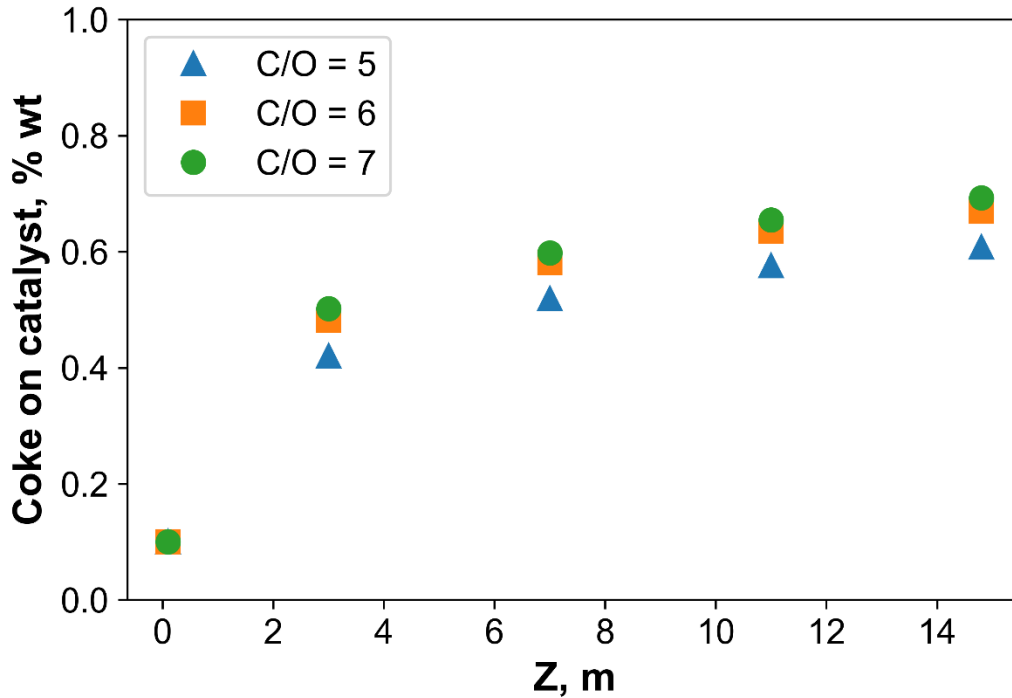
Figure 8.13. Percent of Coke Deposited on the Catalyst along the Downer.

Concerning Figure 8.13, it can be noticed that there is a consistent rapid increase of coke deposition within the first 3 m of the downer unit, with the C/O of 7 yielding the highest coke-on-catalyst fraction. One can notice that the coke level observed represents typical coke yields in FCC units (Arandes et al. 2000). This is required in order to achieve an adequate heat balance in the refinery, with the heat released in the catalyst regenerator being comparable to the heat needed in the cracking unit.

The CPFD simulations can be validated by comparing the simulation temperature at the outlet of the downer with the solution from the energy balance. This is defined by the following equations:

$$\Delta H_1 = F_{VGO} C_{p_{VGO}} (25\,°C - T_{mix}) + F_{cat} C_{p_{cat}} (25°C - T_{mix}) \qquad (8-7)$$

$$\Delta H_2 = \Delta H_{crack} F_{VGO} X_{VGO} \qquad (8-8)$$

$$\Delta H_3 = F_{VGO,out} C_{p_{VGO}}(T_2 - 25°C) + F_{LCO,out} C_{p_{LCO}}(T_2 - 25°C) + F_{Gasoline,out} C_{p_{Gasoline}}(T_2 - 25°C)$$
$$+F_{Light\ Gases,out} C_{p_{Light\ Gases}}(T_2 - 25°C) + F_{Coke,out} C_{p_{Coke}}(T_2 - 25°C) + F_{cat} C_{p_{cat}}(T_2 - 25°C) \quad (8-9)$$

$$\Delta H_1 + \Delta H_2 + \Delta H_3 = 0 \qquad\qquad (8-10)$$

The parameters for the energy balance are reported in Table 8.4.

Table 8.4. Parameters for Energy Balance

Parameter	Value
VGO Specific heat (J/kg K)	2670
LCO Specific heat (J/kg K)	3300
Gasoline Specific heat (J/kg K)	3300
Light Gases Specific heat (J/kg K)	2800
Coke Specific Heat (J/kg K)	1650
ΔH_{crack} (kJ/kg K)	416
Catalyst Specific Heat (J/kg K)	1046

The calculation of the outlet temperature for the C/O of 5 is done with conditions reported in Table 8.5.

Table 8.5. Operating Conditions For C/O = 5

Parameter	Value
VGO mass flowrate (kg/s)	0.055
VGO Inlet T (°C)	220
Catalyst flowrate (kg/s)	0.275
Catalyst Inlet T (°C)	690
Mixing point T (°C)	526.9
Conversion (%)	42.5

Solving Equations 8-7 to 8-10 results in a final temperature of 497.17 °C, while the simulation results show an outlet temperature of 501.3 °C. Thus, the error is 0.83%.

For C/O = 7, the conditions are shown in Table 8.6.

Table 8.6. Operating Conditions For C/O = 7

Parameter	Value
VGO mass flowrate (kg/s)	0.055
VGO Inlet T (°C)	220
Catalyst flowrate (kg/s)	0.385
Catalyst Inlet T (°C)	690
Mixing point T (°C)	560.7
Conversion (%)	56

The final temperature for this case is 534.9 °C. The simulation reports an outlet temperature of 530.71 °C. The error between the calculation and the simulation is 0.78%.

Thus, the present study demonstrates that the proposed CPFD simulation, which uses a trustable kinetics for VGO catalytic cracking from the CREC Riser Simulator, shows that an FCC downer reactor operated with a C/O of 5-7, displays the following significant features:

- o Good mixing of the hot solids and the VGO-steam streams using the proposed downer feeding unit.
- o Close control of cluster particle velocities and particle volume fractions along the downer length, after the 1-2m of the downer feeding section.
- o Quick heating and vaporization of the VGO, by the stream of hot particle clusters, with both phases reaching close thermal levels in less than 2-meters of the downer unit,
- o Good overall VGO conversion, which is achieved in a 15 m downer unit, with gasoline selectivities being higher than the light cycle oil selectivities.
- o Coke-on-catalyst at the 15 m downer outlet, which is consistent with that of an FCC unit operated as a desirable autothermal process: the heat released from the coke combustion in the regenerator is close to the heat of enthalpy required by the endothermic catalytic cracking reactions in the downer.

8.5 Conclusions

a) A catalytic cracking FCC unit can be simulated using a trustable five-lump kinetic model obtained in a CREC Riser Simulator laboratory scale unit and a MP-PIC model using CPFD Barracuda VR software.

b) The *MP-PIC Model with a 5-lump kinetics* is able to successfully incorporate a cluster particle size distribution into the simulation, allowing the evaluation of the catalyst-to-oil ratio influence on the FCC unit operation.

c) The *MP-PIC Model with a 5 lump kinetics* shows good gas-solid mixing, with uniform radial profiles for both particle cluster velocities and particle volume fractions. Results show that a 0.5 m- 2 m minimum axial downer length is needed to achieve a fully developed particle cluster velocity and particle volume fraction radial profiles, with this minimum mixing-stabilization downer length being a function of the C/O ratio.

d) *The MP-PIC Model with a 5 lump kinetics* shows 56.1% VGO conversion, with this being a function of the catalyst density or the equivalent, the C/O ratio. Additionally, this simulation allows one to show that desirable conditions of gasoline selectivities, surpassing light cycle oil selectivities, can be achieved at the highest C/O ratio of 7.

e) *The MP-PIC Model with a 5 lump kinetics* demonstrates that thermal equilibrium between gas and solid flowing phases can be consistently obtained in a 0.5-2m axial downer mixing length, with this mixing length being the largest for the highest C/O ratios.

f) *The MP-PIC Model with a 5 lump kinetics* shows that the highest C/O ratio of 7 leads to the highest coke yields, with the coke, formed occurring mostly in the first three meters of the downer reactor unit.

9   Conclusions and Recommendations

The present PhD dissertation reports the outcomes of a research study on downflow reactors, with a special focus on the feeding/entrance section of the downflow reactor.

From the experimental results, one can provide the following concluding remarks:

a) The downflow, or downer reactor, shows very uniform radial particle cluster velocities and radial particle volume fractions.

b) These experimentally based results, obtained with CREC-Optiprobes, show very effective gas-solid mixing at the downer entry section, using the selected gas-solid feeding system, which includes a solid particle feeding cyclone and feeding ring, which uses strategically positioned and directed steam and VGO jets.

c) The selected gas-solid feeder (gas and solids) and the downer geometry chosen, provide close particle residence times. Thus, the overall downer reactor fluid dynamics approximate the ideal plug-flow.

d) The experimental results from the present PhD Dissertation, obtained at different axial positions in a 0.051 m OD diameter and 2m length downer unit, allow establishing an acceleration and stabilization zones and this on the basis of cluster velocity, cluster shape, and size.

e) The experimentally measured particle cluster velocities display in the 0.051 m OD diameter and 2m length laboratory-scale unit entry section, 0.7 – 0.8 m/s particle velocities. This provides evidence that at the entry downer level, particle velocities do not reach the cluster terminal velocity.

f) The experimental cluster size distributions at the laboratory scale entry section, are of the wide and close to normal distribution type, with an average cluster size of 8-9 particles. On the other hand, the observed cluster size distribution in the fully developed flow downer section shows particle cluster velocities in the 1.1-1.4 m/s range, with a particle cluster size displaying a skewed distribution, with 3-4 particle clusters being the most frequent.

g) The experimental results obtained point towards different particle cluster arrangements in the various downer sections. Clusters near the feeding zone display a close packed 'quasi-spherical' shape. However, once particle clusters

reach the fully developed flow section, their shapes evolve towards a "train of particles", with the cluster adopting a more stable strand fluid dynamic configuration.

Regarding the CPFD simulation results, the following can be concluded:

a) A Hybrid Numerical Cluster Model was successfully developed with the MP-PIC method. The Hybrid Numerical Cluster Model used the cluster size distributions determined experimentally with the help of the CREC-Optiprobes.

b) The Hybrid Numerical Cluster Model was able to describe the gas-solid behaviour in a 0.051 m OD diameter and 2 m height downer unit at different axial positions, and for a wide range of operating conditions.

c) The Hölzer-Sommerfeld drag correlation provided the best approximation for the MP-PIC simulations. To support this, clusters were assigned a close packed 'quasi-spherical' geometry in the downer entry section, and a strand shape in the lower and fully developed flow section.

Once the MP-PIC Model was validated with the experimental data from the 0.051 m OD diameter and a 2 m height cold-flow unit, a 0.15 m diameter and 15 m, high temperature demonstration-scale FCC downer unit was successfully simulated using a five-lump kinetic model. The effect of the catalyst-to-oil ratio in this unit operation was evaluated and the following was concluded:

a) The Hybrid Numerical Cluster Model with a MP-PIC method and a five-lump kinetics successfully describes both the hydrodynamics and the extent of the catalytic cracking reactions in the 0.15 m-diameter and 15 m length demonstration-scale downer reactor. This includes both the downer entry section and the downer flow stabilized section.

b) The 15 m FCC downer reactor of the present study was operated with 0.4-micron Y-zeolites dispersed on 60-micron catalyst particles. This allows minimizing intracrystalline diffusional transport limitations, reaching yields of 56.1% VGO conversion with a C/O of 7. At this catalyst-to-oil ratio, the best gasoline selectivities, surpassing both those of light cycle oil and light gases yields, were

obtained. This highest C/O of 7, also led to 0.68 wt% coke yields which are compatible with the needed to secure the autothermal balance of the FCC process.

c) The radial and axial profiles of particle cluster velocity, particle volume fraction, and temperatures in the 0.15 m-diameter and 15 m length downer showed that an axial length in the entry section is required to achieve a fully developed flow in the FCC downer.

d) This entry length in the downer was found to be a function of the catalyst-to-oil ratio, with the highest C/O of 7 yielding the conditions requiring the longest downer entry length, and this for achieving adequate gas-solid mixing and flow development.

Recommendations

Based on the outcomes from the present research study, the following recommendations can be suggested:

a) To develop an extended MP-PIC simulation including both a vacuum gas oil downer catalytic cracking unit and a catalyst regenerator unit. This will allow one to establish a First Principle Model for the entire FCC process loop. This simulation could provide the information required to secure the thermal balance and the controllability of the complete FCC reactor unit.

a) The downer vacuum gas oil FCC catalytic cracking unit should incorporate more advanced kinetic models developed in the CREC Riser Simulator, as they become available, where C/O ratios are incorporated in a more rigorous manner, as recently postulated by Alkhlel and de Lasa (de Lasa and Alkhlel 2019).

Bibliography

Abbasi, Alireza. 2013. "CPFD Flow Pattern Simulation in Downer Reactor." *AIChE Journal*. https://doi.org/10.1002/aic.

Abul-Hamayel, M. A. 2004. "Comparison of Downer and Riser Based Fluid Catalytic Cracking Process at High Severity Condition: A Pilot Plant Study." *Petroleum Science and Technology* 22 (5–6): 475–90. https://doi.org/10.1081/LFT-120034183.

Ahmed, Imtiaz, and Hugo de Lasa. 2020. "CO2 Capture Using Chemical Looping Combustion from a Biomass-Derived Syngas Feedstock: Simulation of a Riser-Downer Scaled-Up Unit." *Industrial and Engineering Chemistry Research* 59 (15): 6900–6913. https://doi.org/10.1021/acs.iecr.9b05753.

Al-Sabawi, Mustafa, Jesús A. Atias, and Hugo de Lasa. 2006. "Kinetic Modeling of Catalytic Cracking of Gas Oil Feedstocks: Reaction and Diffusion Phenomena." *Industrial and Engineering Chemistry Research* 45 (5): 1583–93. https://doi.org/10.1021/ie050683x.

Al-Sabawi, Mustafa, Jesús A. Atias, and Hugo De Lasa. 2008. "Heterogeneous Approach to the Catalytic Cracking of Vacuum Gas Oil." *Industrial and Engineering Chemistry Research* 47 (20): 7631–41. https://doi.org/10.1021/ie701745k.

Ancheyta-Juárez, Jorge, Felipe López-Isunza, Enrique Aguilar-Rodríguez, and Juan C. Moreno-Mayorga. 1997. "A Strategy for Kinetic Parameter Estimation in the Fluid Catalytic Cracking Process." *Industrial and Engineering Chemistry Research* 36 (12): 5170–74. https://doi.org/10.1021/ie970271r.

Andrews, M. J., O'Rourke, P. J. 1996. "The Multiphase Particle-in-Cell (MP-PIC) Method for Dense Particle Flow."

Arandes, José M., Miren J. Azkoiti, José Bilbao, and Hugo I. De Lasa. 2000. "Modelling FCC Units under Steady and Unsteady State Conditions." *Canadian Journal of Chemical Engineering* 78 (1): 111–23. https://doi.org/10.1002/cjce.5450780116.

Ariyaratne, W. K.Hiromi, Chandana Ratnayake, and Morten C. Melaaen. 2017. "Application of the MP-PIC Method for Predicting Pneumatic Conveying

Characteristics of Dilute Phase Flows." *Powder Technology* 310: 318–28. https://doi.org/10.1016/j.powtec.2017.01.048.

Armor, John N. 2011. "A History of Industrial Catalysis." *Catalysis Today* 163 (1): 3–9. https://doi.org/10.1016/j.cattod.2009.11.019.

Ashraful Islam, Mohammad, Stefan Krol, and Hugo I. de Lasa. 2011. "The CREC-GS-Optiprobes and Its Focal Region. Gas-Solid Flow Measurements in down Flow Reactors." *Chemical Engineering Science* 66 (8): 1671–84. https://doi.org/10.1016/j.ces.2011.01.004.

Babich, I. V., and J. A. Moulijn. 2003. "Science and Technology of Novel Processes for Deep Desulfurization of Oil Refinery Streams: A Review." *Fuel* 82 (6): 607–31. https://doi.org/10.1016/S0016-2361(02)00324-1.

Bagheri, Gholamhossein, and Costanza Bonadonna. 2016. "On the Drag of Freely Falling Non-Spherical Particles." *Powder Technology* 301: 526–44. https://doi.org/10.1016/j.powtec.2016.06.015.

Ball, J. S., and J. X. Zhu. 2001. "A Preliminary Study into the Local Solids Fluxes in a Downer Reactor." *Powder Technology* 114 (1–3): 96–101. https://doi.org/10.1016/S0032-5910(00)00274-6.

Bang, Jjn Hwan, Yong Jeon Kim, Won Namkung, and Sang Done Kimt. 1999. "Radial Gas Mixing Characteristics in a Downer Reactor." *Korean J. Chem. Eng.*. 16 (5): 624–29. https://doi.org/10.1007/BF02708142.

Bartholomew, R. N., and R. M. Casagrande. 1957. "Measuring Solids Concentration in Fluidized Systems by Gamma-Ray Absorption." *Industrial and Engineering Chemistry* 49 (3): 428–31. https://doi.org/10.1021/ie51392a041.

Bassi, A B, C L Briens, and M A Bergougnou. 1994. "Short Contact Time Fluidized Reactors (SCTFRs)." In *Circulating Fluidized Bed Technology IV*, 15–19. AIChE, New York.

Beetstra, R., M. A. van der Hoef, and J. A M Kuipers. 2007. "Numerical Study of Segregation Using a New Drag Force Correlation for Polydisperse Systems Derived

from Lattice-Boltzmann Simulations." *Chemical Engineering Science* 62 (1–2): 246–55. https://doi.org/10.1016/j.ces.2006.08.054.

Berg, D. A., C. L. Briens, and M. A. Bergougnou. 1989. "Reactor Development for the Ultrapyrolysis Process." *Canadian Journal of Chemical Engineering* 67 (1): 96–101.

Berrouk, Abdallah S., C. Pornsilph, S. S. Bale, Y. Du, and K. Nandakumar. 2017. "Simulation of a Large-Scale FCC Riser Using a Combination of MP-PIC and Four-Lump Oil-Cracking Kinetic Models." *Energy and Fuels* 31 (5): 4758–70. https://doi.org/10.1021/acs.energyfuels.6b03380.

Bhusarapu, Satish, Muthanna H. Al-Dahhan, and Milorad P. Duduković. 2006. "Solids Flow Mapping in a Gas-Solid Riser: Mean Holdup and Velocity Fields." *Powder Technology* 163 (1–2): 98–123. https://doi.org/10.1016/j.powtec.2006.01.013.

Breck, Donald W. 1964. Crystalline Zeolite Y. U. S. 3,130,007, issued 1964.

Bridgwater, A. V., and G. V.C. Peacocke. 2000. "Fast Pyrolysis Processes for Biomass." *Renewable and Sustainable Energy Reviews* 4 (1): 1–73. https://doi.org/10.1016/S1364-0321(99)00007-6.

Cao, C., and H. Weinstein. 2000. "Gas Dispersion in Downflowing High Velocity Fluidized Beds." *AIChE Journal* 46 (3): 523–28. https://doi.org/10.1002/aic.690460311.

Cao, C, Y Jin, Z Yu, and Z Wang. 1995. "Gas-Solids Velocity Profiles and Slip Phenomenon in a Cocurrent Downflow Circulating Fluidized Bed." *JOURNAL OF CHEMICAL INDUSTRY AND ENGINEERING-CHINA-* 46: 180.

Capart, H., D. L. Young, and Y. Zech. 2002. "Voronoï Imaging Methods for the Measurement of Granular Flows." *Experiments in Fluids* 32 (1): 121–35. https://doi.org/10.1007/s003480200013.

Cate, A. ten, C. H. Nieuwstad, J. J. Derksen, and H. E A Van den Akker. 2002. "Particle Imaging Velocimetry Experiments and Lattice-Botlzmann Simulations on a Single Sphere Settling under Gravity." *Physics of Fluids* 14 (11): 4012–25. https://doi.org/10.1063/1.1512918.

Chalermsinsuwan, Benjapon, Titinan Chanchuey, Waraporn Buakhao, Dimitri Gidaspow, and Pornpote Piumsomboon. 2012. "Computational Fluid Dynamics of Circulating Fluidized Bed Downer: Study of Modeling Parameters and System Hydrodynamic Characteristics." *Chemical Engineering Journal* 189–190: 314–35. https://doi.org/10.1016/j.cej.2012.02.020.

Cheng, W.-C., G. Kim, a. W. Peters, X. Zhao, K. Rajagopalan, M. S. Ziebarth, and C. J. Pereira. 1998. *Environmental Fluid Catalytic Cracking Technology. Catalysis Reviews.* Vol. 40. https://doi.org/10.1080/01614949808007105.

Cheng, Y., J. Q. Chen, Y. L. Ding, X. Y. Xiong, and Y. Jin. 2008. "Inlet Effect on the Coal Pyrolysis to Acetylene in a Hydrogen Plasma Downer Reactor." *Canadian Journal of Chemical Engineering* 86 (3): 413–20. https://doi.org/10.1002/cjce.20049.

Cheng, Yi, Yincheng Guo, Fei Wei, Yong Jin, and Wenyi Lin. 1999. "Modeling the Hydrodynamics of Downer Reactors Based on Kinetic Theory." *Chemical Engineering Science* 54 (13–14): 2019–27. https://doi.org/10.1016/S0009-2509(98)00293-0.

Cheng, Yi, Changning Wu, Jingxu Zhu, Fei Wei, and Yong Jin. 2008. "Downer Reactor: From Fundamental Study to Industrial Application." *Powder Technology* 183 (3): 364–84. https://doi.org/10.1016/j.powtec.2008.01.022.

Chhabra, R. P., L. Agarwal, and N. K. Sinha. 1999. "Drag on Non-Spherical Particles: An Evaluation of Available Methods." *Powder Technology* 101 (3): 288–95. https://doi.org/10.1016/S0032-5910(98)00178-8.

Cocco, Ray, William D. Fullmer, and Peiyuan Liu. 2017. "CFD-DEM - Modeling the Small to Understand the Large." *Chemical Engineering Progress* 113 (9): 38–45.

Cocco, Ray, S. B Reddy Karri, and Ted Knowlton. 2014. "Introduction to Fluidization." *Chemical Engineering Progress* 110 (11): 21–29.

Courant, R, K Friedrichs, and H Lewy. 1967. "On the Partial Difference Equations of Mathematical Physics." *IBM Journal of Research and Development* 11 (2): 215–34. https://doi.org/10.1147/rd.112.0215.

Dewitz, Thomas. 1989. Downflow fluidized catalytic cracking system, issued 1989.

Ganser, Gary H. 1993. "A Rational Approach to Drag Prediction of Spherical and Nonspherical Particles." *Powder Technology* 77 (2): 143–52. https://doi.org/10.1016/0032-5910(93)80051-B.

Gartside, Robert J. 1989. "QC—a New Reaction System." *Fluidization VI*, 25–32.

Geldart, D. 1973. "Types of Gas Fluidization." *Powder Technology* 7 (5): 285–92. https://doi.org/10.1016/0032-5910(73)80037-3.

Gidaspow, Dimitri. 1992. "Hydrodynamics of Circulating Fluidized Beds: Kinetic Theory Approach." *Fluidization VII* 1.

Grace, John R, A A Avidan, and T M Knowlton. 1997. "Circulating Fluidized Beds ." New York;London; : Blackie Academic & Professional .

Gross, Benjamin, and Michael Ramage. 1983. FCC Reactor with a downflow reactor riser. US patent 4,385,985, issued 1983.

Hagemeier, Thomas, Christoph Roloff, Andreas Bück, and Evangelos Tsotsas. 2015. "Estimation of Particle Dynamics in 2-D Fluidized Beds Using Particle Tracking Velocimetry." *Particuology* 22: 39–51. https://doi.org/10.1016/j.partic.2014.08.004.

Hahn, Gerald, and Samuel S. Shapiro. 1967. *Statistical Models in Engineering*. Wiley.

Haider, A., and O. Levenspiel. 1989. "Drag Coefficient and Terminal Velocity of Spherical and Nonspherical Particles." *Powder Technology* 58 (1): 63–70. https://doi.org/10.1016/0032-5910(89)80008-7.

Hao, Jian, Tsorng Whay Pan, Roland Glowinski, and Daniel D. Joseph. 2009. "A Fictitious Domain/Distributed Lagrange Multiplier Method for the Particulate Flow of Oldroyd-B Fluids: A Positive Definiteness Preserving Approach." *Journal of Non-Newtonian Fluid Mechanics* 156 (1–2): 95–111. https://doi.org/10.1016/j.jnnfm.2008.07.006.

Herbert, P. M.; Gauthier, T. A.; Briens, C. L. 1998. "Flow Study of a 0.05 m Diameter Downflow Circulating Fluidized Bed." *Powder Technology* 96: 255–61.

Herbert, P. M., T. A. Gauthier, C. L. Briens, and M. A. Bergougnou. 1994. "Application of

Fiber Optic Reflection Probes to the Measurement of Local Particle Velocity and Concentration in Gas-Solid Flow." *Powder Technology* 80 (3): 243–52. https://doi.org/10.1016/0032-5910(94)02859-1.

Hölzer, Andreas, and Martin Sommerfeld. 2008. "New Simple Correlation Formula for the Drag Coefficient of Non-Spherical Particles." *Powder Technology* 184 (3): 361–65. https://doi.org/10.1016/j.powtec.2007.08.021.

Jian, H., and R. Ocone. 2003. "Modelling the Hydrodynamics of Gas-Solid Suspension in Downers." *Powder Technology* 138 (2–3): 73–81. https://doi.org/10.1016/j.powtec.2003.07.001.

Jiménez-García, Gladys, Ricardo Aguilar-López, and Rafael Maya-Yescas. 2011. "The Fluidized-Bed Catalytic Cracking Unit Building Its Future Environment." *Fuel* 90 (12): 3531–41. https://doi.org/10.1016/j.fuel.2011.03.045.

Jin, Y, F Wei, Y Cheng, Z Wang, and J F Wang. 2000. "Gas and Solid Parallel-Flow Folding Type Quick Fluidized-Bed Reactor." *Chinese Patent, ZL00100823* 4.

Jin, Yong, and Wei Chen. 1994. "Dispersion of Lateral and Axial Solids in a Cocurrent Downflow Circulating Fluidized Bed." *Powder Technology* 81: 25–30.

Kadyrov, Tagir, Fei Li, and Wei Wang. 2019. "Impacts of Solid Stress Model on MP-PIC Simulation of a CFB Riser with EMMS Drag." *Powder Technology* 354: 517–28. https://doi.org/10.1016/j.powtec.2019.06.018.

Kim, Y. J., S. H. Lee, and S. D. Kim. 2001. "Coal Gasification Characteristics in a Downer Reactor." *Fuel* 80 (13): 1915–22. https://doi.org/10.1016/S0016-2361(01)00052-7.

Krol, S., A. Pekediz, and H. I. de Lasa. 2000. "Particle Clustering in down Flow Reactors." *Powder Technology* 108 (1): 6–20. https://doi.org/10.1016/S0032-5910(99)00196-5.

Lanza, A., M. A. Islam, and H. de Lasa. 2012. "Particle Clusters and Drag Coefficients in Gas-Solid Downer Units." *Chemical Engineering Journal* 200–202: 439–51. https://doi.org/10.1016/j.cej.2012.06.027.

Lanza, A., M. Islam, and H. de Lasa. 2017. "Particle Cluster Sizing in Downer Units.

Applicable Methodology across Downer Scale Units." *Powder Technology* 316: 198–206. https://doi.org/10.1016/j.powtec.2016.11.035.

Lanza, A., M A Islam, and H De Lasa. 2016a. "CPFD Modeling and Experimental Validation of Gas – Solid Flow in a down Flow Reactor." *Computers and Chemical Engineering* 90: 79–93. https://doi.org/10.1016/j.compchemeng.2016.04.007.

Lanza, A., and H. de Lasa. 2016. "CPFD Modeling and Experimental Validation of Gas-Solid Flow in a down Flow Reactor." *Computers and Chemical Engineering* 90 (May): 79–93.

Lanza, A., and H. de Lasa. 2017. "Scaling-up down Flow Reactors. CPFD Simulations and Model Validation." *Computers & Chemical Engineering* 101: 226–42. https://doi.org/10.1016/j.compchemeng.2017.02.034.

Lanza, A, M Islam, and H De Lasa. 2016b. "Particle Cluster Sizing in Downer Units . Applicable Methodology across Downer Scale Units." *Powder Technology*. https://doi.org/10.1016/j.powtec.2016.11.035.

Lasa, Hugo de, and Abdualkaber Alkhlel. 2019. "Catalyst / Feedstock Ratio Effect on FCC Using Different Catalysts Samples."

Lehner, P, and K.-E Wirth. 1999. "Characterization of the Flow Pattern in a Downer Reactor." *Chemical Engineering Science* 54: 5471–83. https://doi.org/10.1016/S0009-2509(99)00286-9.

Levy, Y., and F. C. Lockwood. 1983. "Laser Doppler Measurements of Flow in Freeboard of a Fluidized Bed." *AIChE Journal* 29 (6): 889–95. https://doi.org/10.1016/0029-5493(83)90143-7.

Li, Fei, Feifei Song, Sofiane Benyahia, Wei Wang, and Jinghai Li. 2012. "MP-PIC Simulation of CFB Riser with EMMS-Based Drag Model." *Chemical Engineering Science* 82: 104–13. https://doi.org/10.1016/j.ces.2012.07.020.

Li, Songgeng, Weigang Lin, and Jianzhong Yao. 2004. "Modeling of the Hydrodynamics of the Fully Developed Region in a Downer Reactor." *Powder Technology* 145 (2): 73–81. https://doi.org/10.1016/j.powtec.2004.04.040.

Liu, G. Q., S. Q. Li, X. L. Zhao, and Q. Yao. 2008. "Experimental Studies of Particle Flow Dynamics in a Two-Dimensional Spouted Bed." *Chemical Engineering Science* 63 (4): 1131–41. https://doi.org/10.1016/j.ces.2007.11.013.

Liu, W., K. B. Luo, J. X. Zhu, and J. M. Beeckmans. 2001. "Characterization of High-Density Gas-Solids Downward Fluidized Flow." *Powder Technology* 115 (1): 27–35. https://doi.org/10.1016/S0032-5910(00)00276-X.

Loth, E. 2008. "Drag of Non-Spherical Solid Particles of Regular and Irregular Shape." *Powder Technology* 182 (3): 342–53. https://doi.org/10.1016/j.powtec.2007.06.001.

Louge, M., and M. Opie. 1990. "Measurements of the Effective Dielectric Permittivity of Suspensions." *Powder Technology* 62 (1): 85–94. https://doi.org/10.1016/0032-5910(90)80026-U.

Lu, Xuesong, Songgeng Li, Lin Du, Jianzhong Yao, Weigang Lin, and Hongzhong Li. 2005. "Flow Structures in the Downer Circulating Fluidized Bed." *Chemical Engineering Journal* 112 (1–3): 23–31. https://doi.org/10.1016/j.cej.2005.06.002.

Ma, Y., and J. X. Zhu. 1999. "Experimental Study of Heat Transfer in a Co-Current Downflow Fluidized Bed (Downer)." *Chemical Engineering Science* 54 (1): 41–50. https://doi.org/10.1016/S0009-2509(98)00233-4.

Medina-Pedraza, Cesar, and Hugo de Lasa. 2020. "Cluster Acceleration and Stabilization in a Downflow Circulating Fluidized Bed Unit." *Industrial & Engineering Chemistry Research.* https://doi.org/10.1021/acs.iecr.0c01397.

Mok, L K, R G Graham, B A Freel, M A Bergougnou, and R P Overend. 1985. "Fast Pyrolysis (Ultrapyrolysis) of Cellulose and Wood Components." *Journal of Analytical and Applied Pyrolysis* 8: 391–400.

Muldowney, Gregory P. 1995. "FCC Process with Upflow and Downflow Reactor." Google Patents.

Munday, John. 1947. Catalytic Conversion of Hydrocarbons. 2,420,558, issued 1947.

Murphree, E. V., C. L. Brown, H. G. M. Fischer, E. J. Gohr, and W. J. Sweeney. 1943.

"Fluid Catalyst Process. Catalytic Cracking of Petroleum." *Industrial & Engineering Chemistry* 35 (7): 768–73. https://doi.org/10.1021/ie50403a006.

Niccum, Phillip, and Dorrance Bunn. 1985. Catalytic Cracking System. 4,514,285, issued 1985.

Nieuwlan, J.J., R. Meijer, J.A.M. Kuipers, and W.P.M Van Swaaij. 1996. "Measurements of Solids Concentration and Axial Solids Velocity in Gas-Solid Two-Phase Flows." *Powder Technology* 87: 127–39.

Nova, Samuel R., Stefan Krol, and Hugo I. de Lasa. 2004. "CREC Fiber-Optic Probes for Particle Velocity and Particle Clustering: Design Principles and Calibration Procedures." *Industrial & Engineering Chemistry Research* 43 (18): 5620–31. https://doi.org/10.1021/ie0306980.

O'Rourke, Peter J., J. U. Brackbill, and Bernard Larrouturou. 1993. "On Particle-Grid Interpolation and Calculating Chemistry in Particle-in-Cell Methods." *Journal of Computational Physics*. https://doi.org/10.1006/jcph.1993.1197.

O'Rourke, Peter J., and Dale M. Snider. 2010. "An Improved Collision Damping Time for MP-PIC Calculations of Dense Particle Flows with Applications to Polydisperse Sedimenting Beds and Colliding Particle Jets." *Chemical Engineering Science* 65 (22): 6014–28. https://doi.org/10.1016/j.ces.2010.08.032.

Parthasarathi, R. S., and Sarah S. Alabduljabbar. 2014. "HS-FCC High-Severity Fluidized Catalytic Cracking: A Newcomer to the FCC Family." *Applied Petrochemical Research* 4 (4): 441–44. https://doi.org/10.1007/s13203-014-0087-5.

Qi, C M, Z Q Yu, Y Jin, D R Bai, and W H Yao. 1990. "Hydrodynamics of Cocurrent Downwards Fast Fluidization (I) and (II)." *J. Chem. Ind. Eng* 41: 273–90.

Qian, Z. 2006. "Experimental Investigation on the Hydrodynamics and Inlet Outlet Structure in a Large Scale Downer." Ph. D. Thesis, Tsinghua University.

Ropelato, Karolline, Henry F. Meier, and Marco A. Cremasco. 2005. "CFD Study of Gas-Solid Behavior in Downer Reactors: An Eulerian-Eulerian Approach." *Powder Technology* 154 (2–3): 179–84. https://doi.org/10.1016/j.powtec.2005.05.005.

Rostom, S., and H. de Lasa. 2019. "Downer Fluidized Bed Reactor Modeling for Catalytic Propane Oxidative Dehydrogenation with High Propylene Selectivity." *Chemical Engineering and Processing - Process Intensification* 137 (January): 87–99. https://doi.org/10.1016/j.cep.2019.02.002.

Sharma, Arun Kumar. 2000. "Transient Studies in Fast-Fluidized Beds." *Lehigh University*. https://doi.org/10.16953/deusbed.74839.

Snider, D M. 2001. "An Incompressible Three-Dimensional Multiphase Particle-in-Cell Model for Dense Particle Flows." *Journal of Computational Physics* 170: 523–49. https://doi.org/10.1006/jcph.2001.6747.

Sobocinski, D. A.; Young, B. J.; de Lasa, H. 1995. "New Fiber-Optic Method for Measuring Velocities of Strands and Solids Hold-up in Gas-Solids Downflow Reactors." Powder Technology.

Syamlal, M. 2007. "Report on Workshop on Multiphase Flow." *Energy*.

Talman, J. A., and L. Reh. 2001. "An Experimental Study of Fluid Catalytic Cracking in a Downer Reactor." *Chemical Engineering Journal* 84 (3): 517–23. https://doi.org/10.1016/S1385-8947(00)00375-2.

Talman, J A, R Geier, and L Reh. 1999. "Development of a Downer Reactor for Fluid Catalytic Cracking." *Chemical Engineering Science* 54: 2123–30. https://doi.org/10.1016/S0009-2509(98)00378-9.

Tang, Yali; Peters, E.; Kuipers, J. 2016. "Direct Numerical Simulations of Dynamic Gas-Solid Suspensions." *AIChE Journal* 62 (6): 1958–69. https://doi.org/10.1002/aic.

Tsuji, Y., T. Kawaguchi, and T. Tanaka. 1993. "Discrete Particle Simulation of Two-Dimensional Fluidized Bed." *Powder Technology* 77 (1): 79–87. https://doi.org/10.1016/0032-5910(93)85010-7.

Tuzla, K. Sharma, A. K. 1998. "Transient Dynamics of Solid Concentration in Downer Fluidized Bed." *Powder Technology* 100: 166–72.

Vogt, E. T. C., and B. M. Weckhuysen. 2015. "Fluid Catalytic Cracking: Recent

Developments on the Grand Old Lady of Zeolite Catalysis." *Chem. Soc. Rev.* 44 (20): 7342–70. https://doi.org/10.1039/C5CS00376H.

Wang, Chengxiu; Li, Chunyi; Barghi, Shahzad; Zhu, Jesse. 2015. "A Comparison of Flow Development in High Density Gas-Solids Circulating Fluidized Bed Downer and Riser Reactors." *AIChE Journal* 61 (4): 1172–83. https://doi.org/10.1002/aic.

Wang, Chengxiu. 2013. "High Density Gas Solids Circulating Fluidized Bed Riser and Downer Reactors."

Wang, Chengxiu, Chunyi Li, and Jesse Zhu. 2015. "Axial Solids Flow Structure in a High Density Gas – Solids Circulating Fluidized Bed Downer." *Powder Technology* 272: 153–64. https://doi.org/10.1016/j.powtec.2014.11.041.

Wang, Jieguang, Xuesong Lu, Jianzhong Yao, Weigang Lin, and Lijie Cui. 2005. "Experimental Study of Coal Topping Process in a Downer Reactor." *Industrial & Engineering Chemistry Research* 44 (3): 463–70.

Wang, Z., D. Bai, and Y. Jin. 1992. "Hydrodynamics of Cocurrent Downflow Circulating Fluidized Bed (CDCFB)." *Powder Technology* 70 (3): 271–75. https://doi.org/10.1016/0032-5910(92)80062-2.

Wei, Fei, Yong Jin, Zhiqing Yu, Wei Chen, and S. Mori. 1995. "Lateral and Axial Mixing of the Dispersed Particles in CFB." *Journal of Chemical Engineering of Japan*. https://doi.org/10.1252/jcej.28.506.

Wei, Fei, Yong Jin, Zhiqing Yu, and Jinzhong Liu. 1995. "Gas Mixing in the Cocurrent Downflow Circulating Fluidised Bed." *Chemical Engineering & Technology* 18 (1): 59–62. https://doi.org/10.1002/ceat.270180111.

Wei, Fei, and Jing Xu Zhu. 1996. "Effect of Flow Direction on Axial Solid Dispersion in Gas-Solids Cocurrent Upflow and Downflow Systems." *The Chemical Engineering Journal* 64: 345–52. https://doi.org/10.1016/S0923-0467(96)85016-0.

Werther, Joachim. 1999. "Measurement Techniques in Fluidized Beds." *Powder Technology* 102 (1): 15–36. https://doi.org/10.1016/S0032-5910(98)00202-2.

Wu, B., J. X. Zhu, L. Briens, and H. Zhang. 2007. "Flow Dynamics in a Four-Inch Downer Using Solids Concentration Measurements." *Powder Technology* 178 (3): 187–93. https://doi.org/10.1016/j.powtec.2007.05.006.

Wylie, Jonathan J., and Donald L. Koch. 2000. "Particle Clustering Due to Hydrodynamic Interactions." *Physics of Fluids* 12 (5): 964–70. https://doi.org/10.1063/1.870351.

Xu, Jing, and J. X. Zhu. 2010. "Experimental Study on Solids Concentration Distribution in a Two-Dimensional Circulating Fluidized Bed." *Chemical Engineering Science* 65 (20): 5447–54. https://doi.org/10.1016/j.ces.2010.07.015.

Yang, Wen-Ching. 2003. *Handbook of Fluidization and Fluid-Particle Systems*.

Yinghui, Zhang, Lan Zingying, and Gao Jinsen. 2012. "Modeling of Gas-Solid Flow in a CFB Riser Based on Computational Particle Fluid Dynamics." *Petroleum Science* 9 (4): 535–43. https://doi.org/10.1007/s12182-012-0240-7.

Young, Brad J, Hugo I. de Lasa, and Stefan Krol. 1998. Fiber Optic for Sensing Particle Movement in a Catalytic Reactor, issued 1998.

Yun, Song, Weizhong Qian, Chaojie Cui, Yuntao Yu, Chao Zheng, Yi Liu, Qiang Zhang, and Fei Wei. 2013. "Highly Selective Synthesis of Single-Walled Carbon Nanotubes from Methane in a Coupled Downer-Turbulent Fluidized-Bed Reactor." *Journal of Energy Chemistry* 22 (4): 567–72. https://doi.org/10.1016/S2095-4956(13)60074-1.

Zhang, H., J-X. Zhu, and M.A. Bergougnou. 1999. "Hydrodynamics in Downflow Fluidized Beds (1): Solids Concentration Profiles and Pressure Gradient Distributions." *Chemical Engineering Science* 54 (22): 5461–70. https://doi.org/10.1016/S0009-2509(99)00284-5.

Zhang, H, W Huang, and J Zhu. 2001. "Gas-Solids Flow Behavior : CFB Riser vs . Downer" 47 (9).

Zhang, H, and J.-X Zhu. 2000. "Hydrodynamics in Downflow Fluidized Beds (2): Particle Velocity and Solids Flux Profiles." *Chemical Engineering Science* 55: 4367–77. https://doi.org/10.1016/S0009-2509(00)00087-7.

Zhang, M. H., K. W. Chu, F. Wei, and A. B. Yu. 2008. "A CFD-DEM Study of the Cluster Behavior in Riser and Downer Reactors." *Powder Technology* 184 (2): 151–65. https://doi.org/10.1016/j.powtec.2007.11.036.

Zhang, Minghui, Zhen Qian, Hao Yu, and Fei Wei. 2003. "The Solid Flow Structure in a Circulating Fluidized Bed Riser/Downer of 0.42-m Diameter." *Powder Technology* 129 (1–3): 46–52. https://doi.org/10.1016/S0032-5910(02)00130-4.

Zhu, Jesse; Manyele, S. 2001. "Radial Nonuniformity Index (RNI) in Fluidized Beds and Other Multiphase Flow Systems." *The Canadian Journal of Chemical Engineering* 79 (April): 203–13.

Zhu, H. P., Z. Y. Zhou, R. Y. Yang, and A. B. Yu. 2007. "Discrete Particle Simulation of Particulate Systems: Theoretical Developments." *Chemical Engineering Science* 62 (13): 3378–96. https://doi.org/10.1016/j.ces.2006.12.089.

Zhu, H P, Z Y Zhou, R Y Yang, and A B Yu. 2008. "Discrete Particle Simulation of Particulate Systems : A Review of Major Applications and Findings" 63: 5728–70. https://doi.org/10.1016/j.ces.2008.08.006.

Zhu, J. X., Zq. Yu, Y. Jin, J. R. Grace, and A Issangya. 1995. "Cocurrent Downflow Circulating Fluidized Bed (Downer) Reactors—a State of the Art Review." *The Canadian Journal of Chemical Engineering* 73: 662–77.

Curriculum Vitae

Cesar Alejandro Medina Pedraza

Post-Secondary Education and Degrees

Ph. D. in Chemical Engineering   2015-2020
University of Western Ontario
London, Ontario, Canada

B. Sc. in Chemical Engineering   2009-2014
Universidad Michoacana de San Nicolás de Hidalgo
Morelia, Michoacán, Mexico

Honours and Awards

Full time scholarship for PhD studies   2015-2020
Sponsored by the Federal Government of Mexico and the Government of the State of
Michoacán through the National Council of Science and Technology (CONACyT) and the
Institute for Science, Technology and Innovation (ICTI)

Award for the Best GPA 94/100 Class 2014   2014
Faculty of Chemical Engineering
Universidad Michoacana de San Nicolás de Hidalgo

Mexican Academy of Science Undergraduate Scholarship awarded for obtaining first
place in the National Chemistry Olympiad contest.   2009-2013

Related Work Experience

Graduate Research Assistant   2015-2020

University of Western Ontario

London, Ontario, Canada

Graduate Teaching Assistant   2015-2020

University of Western Ontario

London, Ontario, Canada

Publications and Conferences

Peer-Reviewed Publications

Cesar Medina-Pedraza, Hugo de Lasa. **Cluster Acceleration and Stabilization in a Downflow Circulating Fluidized Bed Unit**. *Industrial & Engineering Chemistry Research*, 2020, 59, 12360. Impact Factor: 3.573

Cesar Medina-Pedraza, Hugo de Lasa. **Hybrid Particle Cluster CPFD Simulation in the Acceleration and Stabilized Sections of a Downflow Circulating Fluidized Bed**. *Industrial & Engineering Chemistry Research*, 2020, 59, 20325. Impact Factor: 3.573

Podium Presentations

Cesar Medina-Pedraza, Hugo de Lasa. **"Particle Cluster Acceleration and Stabilization in the Feeding Section of a Downer Unit".** AIChE Fluidization XVI Conference. Guilin, China. May 2019.

Cesar Medina-Pedraza, Hugo de Lasa. **"Acceleration and Stabilization of Particle Clusters in a Downflow Catalytic Reactor: Experimental and Modeling Studies."** 70th Canadian Chemical Engineering Conference. Ottawa, Ontario. October 26th – 31st, 2020.